Non-Invasive Venous Thrombus Composition and Therapeutic Response by Multiparametric MRI

by

Olivia Ruth Palmer

A dissertation submitted in partial fulfillment
of the requirements for the degree of
Doctor of Philosophy
(Biomedical Engineering)
in the University of Michigan
2019

Doctoral Committee:

Assistant Research Professor José A. Díaz, Co-Chair
Assistant Professor Joan M. Greve, Co-Chair
Professor Thomas Chenevert
Professor J. Brian Fowlkes

Olivia Ruth Palmer

opalmer@umich.edu

ORCID iD: 0000-0002-6195-8613

Dedication

To my mother, Dione Palmer, who in every way made this dream possible. And to my grandfather, Robert Palmer, who lost his life to complications from deep vein thrombosis just a few months before I began my graduate work.

Acknowledgements

I would like to express my sincerest gratitude to all those who contributed—scientifically and personally—to helping me complete this work. First, I am incredibly grateful to the people who helped me believe I could succeed in this program in the first place. My advisor Joan Greve saw potential in me when I didn't think I could reasonably pursue a PhD. With minimal research experience and completely disparate research interests ranging from optics and environmental engineering to imaging, I was far from an obvious candidate. While I had been told that UM was too much of a "reach" school, Joan went out of her way on the visit weekend to make me feel that I belonged at Michigan. My friend and physics professor Danielle Berg supported and encouraged me through every self-doubt in the decision process. Her pivotal words at that time continue to motivate me: "If you're not scared, then you're not pushing yourself to reach your full potential. People like you and me don't settle for the comfortable path, and that's what separates a good life from an extraordinary life. Do you have the courage to embrace an extraordinary opportunity?"

Joan has supported me in every endeavor, from my research ideas to taking time away for an industry co-op and many extracurricular activities. I am grateful for her unending enthusiasm, genuine care for my wellbeing, and dedication to helping students succeed. I am a better communicator and more confident scientist because of her. This work would also not have been possible if not for Jose Diaz. Beyond teaching me the art of microsurgery, Jose showed me how keep the patient at the heart of basic science research, and perhaps more importantly, how to transform challenges and failure into motivation. And of course, Jose's meticulously polished

PowerPoint presentations inspired my PowerPoint masterpieces that are now visible in several journals. His boundless humility and servant leadership inspires a fierce work ethic in his students, myself included. I am thankful for his tremendous support and guiding example; I would not be the scientist and leader I am today if not for him. I would also like to thank my committee members Tom Chenevert and Brian Fowlkes, for their guidance and support throughout this process. Their expert questions and feedback have been incredibly valuable in the completion of this work.

I have been fortunate to mentor and work with several people on this project. This work would not have been possible if not for the efforts of Calvin Chiu, Grey Braybrooks, Ulrich Scheven, Amos Cao, Paige Castle, Jie Ma, Vijay Vobbilisetty, and Mac Morris. Calvin endured the endless frustration of inserting tail veins for the dobutamine studies in my first paper, along with helping with many hours of imaging and analysis including work on projects that didn't make it into this dissertation. Grey worked largely independently on the collateral project, troubleshooting the meticulous process of building geometric models of small tortuous collateral veins and completing all the imaging for the collaterals paper. Uli and Amos developed highly valuable tools for data analysis. Beyond being a supportive friend, Paige spent her last month in the lab writing the code to apply a Gaussian Mixture Model to my thrombus composition data, adapting work that Jie had done using k-means clustering. I was thrilled when Vijay graciously took over the unhappy task of cleaning mouse poop off running wheels for my exercise study. Vijay also took over most of the imaging in my final exercise studies and spent hours doing tedious thrombus boundary tracing on over 150 data sets. Mac hit the ground running, accepting my challenge to submit an abstract in his first two weeks. I am incredibly grateful for his willingness to help me tackle a very challenging problem and provide valuable scientific contributions to the thrombus classification work.

I am grateful to the members of Jose's lab who taught me all the bench techniques required for this research. Maxim Shaydakov patiently taught me the entire q-RT PCR process (starting with the basics of pipetting). Josh Rainey took time away from his project to help with data collection for Maxim's and my EIM update paper. Melanie Flaherty walked me through the ELISA process, and deeply inspired me with her dedication and passion for basic science research. Mel is one of the greatest scientists I've ever met, and our brief time working together left a lasting impression. Cathy Luke taught me how to do immunohistochemistry and was a tremendous help as I worked through staining over 300 slides.

At the end of my 3rd year, I took a leap into a completely unfamiliar area and became a Technology Transfer Fellow. This 10 hour/week position exposed me to innovations from over 12 different industries. In the 48 invention disclosures I reviewed, I learned how to quickly get up to speed on the technical details in completely new fields, a skill that proved highly valuable for future job prospects. I am grateful to my Tech Transfer supervisor, Anne Juggernauth, for pushing me outside my comfort zone with projects ranging from chemical engineering to autonomous vehicle technology.

The Graduate Society of Women Engineers (GradSWE) has offered a backbone of support and community throughout my graduate work. I served as Activities Co-Chair, then Professional Development Co-Chair, and then Media Officer—roles which connected me to many hardworking and talented people along with other great campus organizations and centers. I simply would not have made it through the hardest periods of my PhD work without this supportive community and many of the friendships that came from it. I am especially grateful to my lab mate and amazing friend Colleen Crouch. Nothing beats a hard day of research like one of our pool breaks, camping trips, or even just a walk around north campus.

I would like to acknowledge my funding sources – the Rackham Merit Fellowship (RMF) and the Graduate Assistance in Areas of National Need fellowship. Through RMF I was able to start research the summer before my first semester, which gave me enough traction to be able to submit a conference abstract in my very first semester. The RMF community has provided a supportive environment and plenty of extremely beneficial write-ins. I also would like to thank the Rackham Graduate School for providing financial assistance with attendance to conferences in Toronto, Tampa, and Berlin. Additionally, the College of Engineering Co-Curricular Grant allowed me to attend a week-long Biotech professional development workshop through the American Society for Cell Biology.

Lastly and most importantly, I would like to thank my extraordinary mother, Dione Palmer. My mom made tremendous sacrifices to carve a loving and stable path for me. She never pushed education; she supported my unusual path through a performing arts high school, and partnered with me in strengthening every essay, project, and presentation. My mom is selfless, compassionate, faithful, and full of astounding strength. She is the source of my tenacity, enthusiasm, communication skills, financial acumen, writing ability, determination, and so much more. This achievement is as much hers as it is my own.

Preface

This dissertation summarizes research that I have conducted over the past five years while working in Dr. Joan Greve's and Dr. José Diaz's laboratories. Sections of this thesis have been previously published and are presented here with some modifications as outlined below.

Chapter 2 is work that has been previously published as follows: Palmer OR, Chiu CB, Cao A, Scheven UM, Diaz JA, Greve JM. In Vivo Characterization of the Murine Venous System Before and During Dobutamine Stimulation: Implications for Preclinical Models of Venous Disease. *Annals of Anatomy*, Sept 1, 2017;214:43-52, PMID 28865773.

Parts of Chapter 3 and Appendix 1 have been adapted from work that has been previously published as follows: Diaz JA, Saha P, Cooley B, Palmer OR, Grover SP, Mackman N, Wakefield TW, Henke PK, Smith A, Lal BK; Choosing a Mouse Model of Venous Thrombosis: A Consensus Assessment of Utility and Application, Dual Publication in *Arteriosclerosis Thrombosis and Vascular Biology* and *Journal of Thrombosis and Haemostasis*, endorsed by the ATVB Council and ISTH. PMID: 30786739.

Chapter 4 is work that has been previously published as follows: Palmer OR, Shaydakov ME, Rainey JP, Lawrence DA, Greve JM, Diaz JA. Update on the Electrolytic IVC Model for Pre-Clinical Studies of Venous Thrombosis. *Research and Practice in Thrombosis and Haemostasis*. 2018; 2: 266-273, PMID 30046728.

Chapter 5 is work that has been submitted for publication as follows: Palmer OR, Braybrooks G, Cao A, Diaz JA, Greve JM. Multiple Overlapping Thin Slap Acquisitions Reveal

Collateral Vein Pathways in Mouse Models of Venous Thrombosis Consistent with Humans. *Journal of Magnetic Resonance Imaging* 2019. (Under Review)

Table of Contents

List of Tables

List of Figures

List of Appendices

List of Abbreviations

In Order of Appearance

Deep Vein Thrombosis	DVT
Magnetic Resonance Imaging	MRI
Pulmonary Embolism	PE
Post Thrombotic Syndrome	PTS
Venous Thromboembolism	VTE
Venous Thrombosis	VT
Interleukin	IL
Low Molecular Weight Heparin	LMWH
Vitamin K Antagonist	VKA
Catheter Directed Thrombolysis	CDT
Percutaneous Mechanical Thrombectomy	PMT
Red Blood Cell	RBC
Von Willebrand Factor	vWF
Neutrophil Extracellular Traps	NETs
Deoxyribose Nucleic Acid	DNA
Computed Tomography	CT
Magnetic Resonance Direct Thrombus Imaging	MR-DTI
Inferior Vena Cava	IVC
Electrocardiogram	ECG

Proportional Integral Derivative	PID
Standard Error of the Mean	SEM
Analysis of Variance	ANOVA
Analysis of Covariance	ANCOVA
Maximum Intensity Projection	MIP
Time of Flight	TOF
Enzyme-Linked Immunosorbent Assay	ELISA
Ferric Chloride	$FeCl_3$
Electrolytic IVC Model	EIM
Thrombus Weight	TW
Interrupted Branches	IB
Open Branches	OB
Plasminogen Activator Inhibitor-1	PAI-1
Voltage to Current Converter	VIC
Direct Current	DC
Polymerase Chain Reaction	PCR
True Controls	TC
Diaminobenzidine	DAB
Tissue Plasminogen Activator	t-PA
Urokinase Plasminogen Activator	u-PA
Not Significant	NS
Pharmacomechanical Catheter Directed Thrombolysis	PCDT
Multiple Overlapping Thin Slab Acquisition	MOTSA

Radiofrequency	RF
Repetition Time	TR
Echo Time	TE
Flip Angle	FA
Contrast to Noise Ratio	CNR
Region of Interest	ROI
Number of Excitations	NEX
Magnetic Resonance Venography	MRV
Apparent Diffusion Coefficient	ADC
Multiparametric MRI	MP-MRI
Martius Scarlet Blue	MSB
Gaussian Mixture Model	GMM
Akaike Information Criterion	AIC
True Control VT Group	CC
Exercise Control Group	EC
Control Heparin Group	CH
Exercise + Heparin Group	EH
Tumor Necrosis Factor α	TNFα
C Reactive Protein	CRP

Abstract

Deep vein thrombosis (DVT), or a blood clot in a deep vein (commonly the legs), is known as the silent killer—there may be few or no symptoms, yet a section of the thrombus could break free and travel to the lungs causing a potentially fatal pulmonary embolism. DVT and its complications affect 900,000 people in the U.S. each year, with one third of cases resulting in fatality. Anticoagulants (the standard treatment) pose serious bleeding risks and rely on the patient's fibrinolytic system to break up the thrombus, which is often incapable of doing so thus leading to post thrombotic syndrome (PTS) in almost 50% of patients. Removing the DVT completely via thrombolytic treatments may improve quality of life by reducing PTS. However, thrombolysis is only effective on acute thrombi. Impaired success with thrombolytic treatment is due to heterogeneity in the thrombus (old clot, which is unable to be broken up, intermixed with fresh clot, which can easily be broken up). This problem is largely overlooked based on an inability to determine thrombus composition.

Currently, the only method for determining disease stage is the patient's recollection of when their symptoms began, which is inherently unreliable and could put the patient at risk. Further, thrombi of the same chronological age may organize at different rates in different people. Magnetic resonance imaging (MRI) has the potential to provide information about thrombus composition (clot age), and thus inform patient-specific treatment planning.

Since there are several limitations to studying DVT in humans, animal models are key tools for understanding the disease. Mouse models are the most commonly used, providing a unique biological environment to study disease progression and treatment. Any model requires

rigorous characterization and standardization to ensure reproducibility between studies. Our first objective was to quantify structural and functional changes in the healthy venous system of young and aged mice of both sexes, at rest and under conditions which simulate exercise. Second, we assessed the endogenous response to two models of DVT mimicking the two possible clinical scenarios: total or partial occlusion.

Following the necessary model characterization, we developed a multiparametric MRI approach to probe thrombus composition without the need for contrast agents. Our results show imaging correlation with known composition by histology. This method provides a novel approach to study thrombus composition, and could eventually be used clinically to provide patient-specific treatment planning for DVT.

Additionally, we investigated the impact of exercise, an emerging therapeutic option, on thrombus composition. Using an in-cage running wheel, our results show that spontaneous exercise – both alone and in combination with standard treatment – reduces initial thrombus size and contributes to thrombus resolution. We found that exercise increases acute fibrin content, attenuates local inflammation, and decreases sub-chronic collagen content in pharmacologically treated mice.

This work provides 1) the first *in vivo* characterization of the murine venous system in health and disease, 2) a foundational methodology to determine thrombus composition by MRI, and 3) insights on the impact of exercise on DVT. This research can help DVT investigators from the animal model perspective, and provides a step forward in characterizing thrombus composition for patient-specific DVT treatment planning.

Chapter 1

Introduction

1.1 Overview of Deep Vein Thrombosis

Deep vein thrombosis (DVT), or a blood clot in a deep vein, is the third most common cardiovascular disease. When considering blood clots, most people think of heart attack and stroke for their imminent and life-threatening outcomes. Conversely, DVT may have few or no symptoms, yet the risk lies in the potential for a portion of the thrombus to break free from its origin—perhaps in the femoral vein of the leg or the ilio-caval veins in the abdomen—travel through the heart and become lodged in the first small vessels it encounters in the lungs. This event is known as a pulmonary embolism (PE), which is fatal in roughly 10% of patients [1]. Thus, DVT is sometimes referred to as the "silent killer." Even in less dire circumstances (absence of PE), chronic DVT leads to the post thrombotic syndrome (PTS), characterized by severe pain and swelling of the affected leg. This condition can be so uncomfortable that patients with PTS have quality of life scores *worse* than patients living with chronic heart, lung, and musculoskeletal conditions [2], [3]. PTS can lead to ulcers and may require amputation.

DVT and PE are collectively referred to as venous thromboembolism (VTE), which affects an estimated 900,000 people in the United States each year [4]. As staggering as this number may be, it is likely an underestimate, as the only prevalence data available is from 2005. Age and obesity are both risk factors for DVT, and with rapid growth in the aging population and an obesity pandemic, the number of people affected by VTE is projected to double by 2050 [4]. Even with standard treatment, one third of patients die of complications from DVT, and nearly half develop PTS [4], [5]. Further, DVT recurrence is a huge problem, affecting 10-30% of DVT patients in 2-5 years [5].

1.2 Treatment History and Standard Practice

Biologically, DVT is a combination of runaway coagulation, sterile inflammation, and a suppressed fibrinolytic system. Most treatments target coagulation to slow or stop the progression of thrombogenesis, known as anticoagulants. Anti-inflammatory approaches are of growing interest but not yet used clinically. Preclinical studies of anti-inflammatory targets have shown promise as a potential DVT therapy without bleeding risk; p-selectin inhibition promoted thrombus resolution and prevented vein wall fibrosis better than anticoagulants in a baboon model [6], and neutralizing interleukin(IL)-6 decreased vein wall intimal thickness and fibrosis in a mouse model [7]. Thrombolytic treatments promote fibrinolysis to get rid of the existing thrombus. Some drugs such as statins have been shown to have pleiotropic effects; statins have been shown to be anti-inflammatory and pro-fibrinolytic. The beneficial role of statins in DVT arose in 2009 from the JUPITER trial, where the rate of DVT was significantly smaller in patients receiving rosuvastatin therapy versus a placebo control [8]. While statins have shown to have prophylactic effects, their potential as a therapeutic remains in question.

Anticoagulant treatment for at least 6 months is the gold standard of treatment in DVT, commonly paired with graduated compression stockings to assist in PTS prevention [9]. Anticoagulation typically includes initial heparin or low molecular weight heparin (LMWH) followed by a vitamin K antagonist (VKAs) such as warfarin. Heparin’s use in humans began in 1935, and with its rapid adoption the mortality from PE among symptomatic DVT patients dropped from 18% to 0.4% [10]. The development of VKAs, however, came from a very different source. In the 1920s, Canadian veterinarians discovered that cattle were bleeding to death after consuming spoiled sweet clover hay, which they termed “sweet clover disease” [11]. Further investigations in 1948 uncovered the anticoagulant agent, which Wisconsin researchers Karl Link and his student Eugen Wilhelm Schoeffel developed into a rat poison that revolutionized the rodenticide field: warfarin. Clinical usefulness had long been suspected, yet physicians were wary to use rat poison on patients until 1951, when a marine inductee was admitted to the hospital for a failed suicide attempt. The marine had consumed 567 mg of warfarin, prompting hemorrhage that was fully treated by Vitamin K administration at the hospital. This event prompted warfarin’s development into Coumadin Sodium, and the standard treatment pairing was established.

Despite limited success, the standard treatment of anticoagulants *has remained unchanged since the 1950s* [10]. By targeting the coagulation cascade, anticoagulants stop the progression of thrombogenesis, but rely on the body’s natural fibrinolytic system (which is often dysfunctional or suppressed in unprovoked DVT) to break up the existing thrombus. Thus, while anticoagulants do prevent pulmonary embolism and thrombus progression during administration, they fail to prevent PTS [12]. More importantly, anticoagulants carry significant risk of major bleeding events, including intracranial hemorrhage. If anticoagulants are contraindicated, vena cava filters may be implanted in an attempt to prevent PE, however this does nothing towards clearing the DVT or mitigating symptoms in the affected leg. In patients with PTS, stents may be placed to promote recanalization in chronically occluded vessels.

Thrombolytic therapies seek to do what anticoagulants cannot: dissolve the existing thrombus. Systemic administration of thrombolytic agents was found to have unacceptably high rates of bleeding complications with only mild thrombus clearance [9], thus localized therapy via catheter directed thrombolysis (CDT) is more commonly used—alone or in combination with percutaneous mechanical thrombectomy (PMT). Anticoagulant therapy is still used before and after thrombolytic treatment. If venous patency remains insufficient (typically <50%) following CDT, a stent is placed to open the vessel.

Although the use of thrombolytic agents for myocardial infarction dates back to the 1950's [13], its use in DVT treatment is complicated. While several small clinical trials have shown significantly improved venous patency and reduced PTS in patients treated with thrombolytics compared to anticoagulation alone [14], the recent multicenter ATTRACT trial concluded that CDT did not reduce PTS or improve quality of life, and worse, increased the risk of major bleeding [15]. A primary factor confounding the use of CDT is its indication for acute DVT. Two weeks is traditionally thought of as the cut-off for the acute phase, yet CDT trials have varied in recruitment cut-off from 10 days to 21 days. This timeline is built from a timeline of symptoms reported by the patient, which is inherently unreliable. *Would the results of the ATTRACT trial proved as dismal if physicians had had a way to verify acute phase by MRI?*

1.3 Thrombus Composition

The effectiveness of thrombolytic treatment and its indication for acute DVT is directly tied to the evolution of thrombus composition. Thrombogenesis is thought to originate in the valve pockets or at a site of endothelial damage [16]. DVT is sometimes referred to as a "red clot" due to the predominance of red blood cells (RBCs) as opposed to the platelet rich "white" arterial clot. RBCs are entrapped by three structures in DVT: fibrin, von Willebrand factor (vWF) strands, and neutrophil extracellular traps (NETs).

Activated endothelial cells release weibel palade bodies containing P-selectin and von Willebrand factor (vWF). vWF strands assemble into 3D web-like structures [17] that entrap RBCs, and this erythrocyte adhesion is further enhanced under stasis conditions—common in the onset of thrombogenesis [18]. At the same time, the adhesion molecule P-selectin facilitates polymorphonuclear neutrophil recruitment. Inflammatory signals then stimulate neutrophil apoptosis, launching the release of neutrophil extracellular traps (NETs) and extracellular DNA. Extracellular DNA further enhances the coagulation cascade and promotes fibrin formation [19], which is concurrently formed by the coagulation cascade. Activated endothelial cells also express tissue factor, a potent pro-coagulant molecule involved in the cascade of events leading to thrombin production, which activates platelets and converts fibrinogen to fibrin.

Together, the vWF strands, NETs, and cross-linked fibrin form traps for RBCs. Thus, the acute thrombus is an amorphous laminar structure composed of RBCs entrapped in layers of fibrin and platelet aggregates. At this stage, the thrombus is a jelly-like consistency, easily probed by a guidewire for CDT. Its instability also makes the acute thrombus more likely to dislodge or have a section dislodge causing a PE. As the fibrin meshwork assembles, platelet aggregates accumulate in a twisted scaffold-like pattern through the brick-and-mortar structure of fibrin and RBCs. Moving into the chronic stage, fibrin is gradually replaced by collagen in a radially inward remodeling process [20]. With the progression of fibrosis, intraluminal synechia develop (Figure 1.1), increasing resistance within the vessel and creating a potentially un-navigable path for a guidewire. This process can permanently damage the valve leaflets leading to dysfunction and reflux. Any attempts at thrombolytic therapy on these chronic segments will be unsuccessful and put the patient at increased bleeding risk [21]. Similarly, anticoagulants will have no effect, leaving stenting as the only option for recanalization to relieve symptoms.

To further complicate matters, most thrombi are not cohesively “acute” or “chronic,” but rather an intertwined combination of phases, with older thrombus closer to the site of thrombogenesis. Additionally, the same chronologically aged thrombus in one patient may have a very different degree of organization compared to another patient, depending on the location and patient characteristics [22].

Figure 1.1 Post thrombotic femoral vein showing intraluminal synechia and thickening of the vein wall. Adapted from Perrin 2014 [23].

1.4 Clinical Thrombus Imaging

Ultrasound is the standard imaging modality for diagnosing DVT, however currently practiced compression ultrasound requires manual compression, making it difficult or impossible to perform on vessels above the inguinal ligament, in obese patients (endemic disease in our country), in patients with an excess of swelling, pregnant women, and patients in casts or other immobilization devices [24]. Ultrasound elastography has shown some preliminary promise in discriminating between acute and chronic DVT (thrombi >8 months old have decreased strain magnitude and increased echo amplitude compared to thrombi <14 days old) [25], however the clinical problem of importance is discerning the transition from acute to chronic, such as a ~10 day old thrombus from a ~18 day old thrombus. Further, ultrasound approaches are operator dependent and are limited in reproducibility [26].

If ultrasound or contrast venography is inconclusive or contraindicated, computed tomography (CT) or MRI may be used. MRI use has mainly been limited to diagnosis in such cases. However, the vast information readily attainable by MRI has the potential to provide patient specific information regarding thrombus composition and thus inform treatment approaches. Currently in the MRI research setting, thrombus is typically imaged using either fast imaging with steady state precession, in which contrast depends on the T2/T1 ratio and the thrombus appears dark relative to flowing blood [27], or a T1-weighted fast spoiled gradient echo sequence with magnetization preparation known as direct thrombus imaging (MR-DTI), in which thrombi rich in methemoglobin appear bright [28]–[31]. MR-DTI may be beneficial in avoiding incorrect diagnosis of recurrent VT because chronic (3 and 6 months post diagnosis) DVT appears dark whereas fresh thrombi is bright [29], [32]. Beyond these extreme acute/chronic ages, however, MR-DTI is incapable of aging the thrombus specifically enough to inform treatment planning.

1.5 Preclinical Models of DVT

The need for improvement in the standard of care is self-evident, and this impetus requires basic science investigations on the evolution of DVT in preclinical models. Unfortunately, there are several limitations to studying DVT in humans: thrombogenesis is unpredictable, patients become symptomatic when the clot is already several days or weeks old, and the only way to get a biopsy of the thrombus-vein wall interface is post mortem or post amputation. Additionally, thrombi develop under complex and continually changing flow conditions, making *in vitro* experiments insufficient for a total understanding of VTE. Thus, animal models are *key tools* for investigating this complex disease. Murine models provide a unique biological environment to study disease progression and treatment, with the added availability of genetically manipulated strains to give insight to molecular pathways.

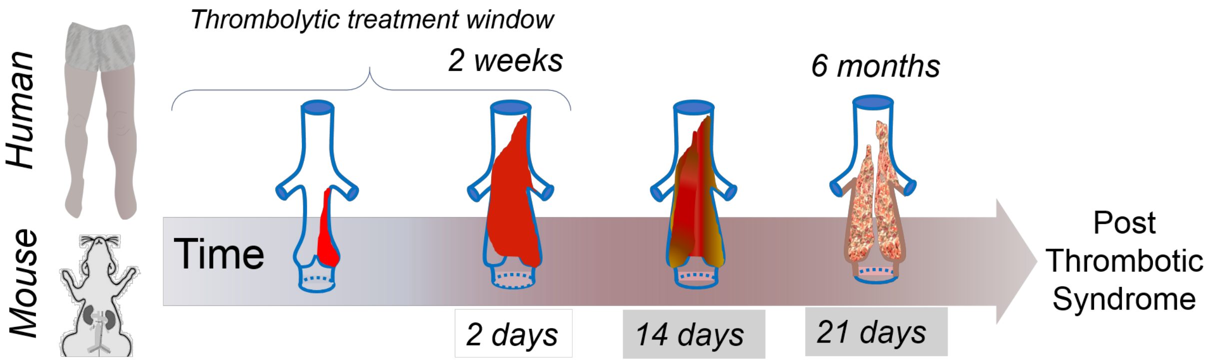

Figure 1.2 DVT composition changes over time, transforming from a jelly-like consistency (acute) to a strong scar-like tissue (chronic), which is not responsive to thrombolytic therapies.

1.6 Thesis Overview

Developing methods to assess thrombus composition and treatment response by MRI begins with understanding the preclinical venous system under both healthy conditions and the two possible disease scenarios of DVT: total or partial occlusion. Most studies prior to this work were focused on *ex vivo* characterization. Our limited understanding of venous biology emphasizes the need to first understand the healthy state to provide a foundation for investigating developing pathology. Thus, my first objective was to quantify structural and functional changes in the *healthy* venous system of young and aged mice of both sexes, at rest and under conditions which simulate exercise (Chapter 2). Understanding the healthy state of the animal model provides the foundation for investigating DVT in mice.

Following the first *in vivo* characterization of the murine venous system, my second objective was to uncover the best practices in the mouse models of venous thrombosis given some of the controversies and problems in the field. Towards this aim, I developed the first model selection algorithm as a tool for researchers and reviewers to select the most appropriate primary and secondary VT model depending on the research question at hand (Chapter 3). Importantly, using MRI techniques I proved the hypothesis that thrombus size variability if branching vessels are left uninterrupted is due to blood flow reversal (Section 3.2). Additionally, on discovering that the original equipment used in the only true blood flow model of VT had been discontinued, I developed an equipment alternative that reduced costs by 90% and provided a critical update on this model to the field (Chapter 4). Vascular obstruction prompts venogenesis, an understudied phenomenon that had previously been noted in animal models. However, the relevance of the most common preclinical model to the human condition was unclear. Thus, I performed a comparative analysis of collateral vein pathways between mice and humans in two mouse models of VT, demonstrating for the first time that mice develop collateral pathways consistent with humans (Chapter 5).

The thorough characterization of the healthy murine venous system, best practices in various VT models, and understanding of the endogenous response to VT provided the necessary foundation to develop imaging methods to advance the treatment paradigm in DVT. My third objective was to develop MRI methods to non-invasively reveal thrombus composition, and thus inform patient-specific treatment planning (Chapter 6). This work showed that multiparametric MRI can discern heterogeneities within the thrombus and thus characterize composition changes both along the thrombus and over time.

Non-invasive determination of thrombus composition provides a platform to investigate how composition changes in response to different therapeutics. Specifically, we were interested in looking at the systemic effects of exercise and its interactions with the current standard pharmacological therapeutic (LMWH). Thus, my fourth objective was to determine whether exercise – alone and coupled with the standard treatment of anticoagulants – correlates to changes in thrombus composition and resolution (Chapter 7).

Chapter 2

In Vivo Characterization of the Murine Venous System Before and During Dobutamine Stimulation: Implications for Preclinical Models of Venous Disease

2.1 Abstract

Although widely used as a preclinical model for studying venous diseases, there is a scarcity of in vivo characterization of the naïve murine venous system. Additionally, previous studies on naïve veins (ex vivo) have not included the influence of surrounding structures and biomechanical forces. Using MRI, we noninvasively quantified the cross-sectional area, cyclic strain, and circularity of the venous system in young and old, male and female C57BL/6 mice. We investigated the most common venous locations used to perform venous disease research: the common jugular vein, suprarenal inferior vena cava (IVC), infrarenal IVC, common iliac vein, and common femoral vein. Our results elucidate age-dependent changes in venous cross-sectional area, which varied by location. Maximum cyclic strain, a parameter of lumen expansion, showed 10% change across the cardiac cycle, approximately half the magnitude of arteries. Veins demonstrated noncircular shapes, particularly in the core vasculature. The cardiovascular stressor dobutamine had only a small impact on the venous system. Also, our data demonstrate that the peripheral veins tend to decrease in cross-sectional area and circularity with age. Conversely, the IVC tends to increase in size and circularity with age, with males exhibiting larger variability in response to dobutamine compared to females. This work provides a foundation for drawing age and sex comparisons in disease models, and represents the first in

vivo characterization of the murine venous system at rest and during the application of a pharmacological exercise surrogate.

2.2 Introduction

Venous diseases have been designated a national priority by the Surgeon General (Leavitt, 2008) and the Center for Disease Control [33]. The troubling statistics on the prevalence of venous disease and data suggesting sub-optimal treatment [34]–[36] emphasize the critical need for a more comprehensive understanding of the venous system, including the geometric and biomechanical characteristics of veins in the animal models so commonly used to investigate disease progression and therapeutic options. While the arterial system has been well studied in health and disease [37], [38], there are far fewer studies regarding venous disease, including a paucity of in vivo investigations of the healthy venous system of murine models.

Blood volume, flow, and pressure dictate vessel shape, in conjunction with vessel wall contents. As such, abnormal vein shape can be indicative of an underlying pathology in the vein lumen, such as thrombosis, or an extraluminal structure deforming a vein, such as a tumor [39]–[41]. Alterations in geometry can lead to changes in biomechanical forces, which play a primary role in the location, initiation, and progression of cardiovascular disease [42]. Thus, understanding the geometry and biomechanics of the healthy venous system establishes the baseline for investigating disease, enabling better interpretation of research results.

Most geometric and biomechanical investigations of the venous system have acquired data *ex vivo* [20], [43]–[45]. Such experiments provide valuable information on material properties and the stress-strain response of the vessel wall. However, *ex vivo* studies are inherently limited to a single time-point and subject to misinterpretations. Non-physiological pressures coupled with a lack of blood flow, external tethering from surrounding anatomical structures, and circumferential and axial stresses—all of which influence vessel structure and function—may alter results. While many intuit the relatively motionless nature of veins compared to arteries, *ex vivo* testing may confound some perspectives on the actual motion of veins *in vivo*, potentially compromising research on the venous system. There is little to no data quantifying cyclic strain of the venous system in humans or the preclinical models often used as surrogates.

Murine models are the most commonly used preclinical model for investigating venous diseases. Mice provide a unique biological environment to study disease progression and treatment in a highly controlled manner, with the added availability of genetically manipulated strains to uncover molecular pathways. Recently, the NIH has addressed concerns over lack of sex diversity in preclinical experiments [46]. In addition, some venous diseases disproportionally affect the older population [4], [47], [48]. Thus, it is imperative to understand the naïve venous system that considers age and sex differences, as outlined in this work.

Dobutamine is a β1-receptor agonist that increases cardiac output. As such, it is used clinically in the treatment of acute heart failure and as one of the most widely available pharmacological stress testing agents [49], [50]. Pharmacologically induced stress testing is used to diagnose cardiovascular disease in patients presenting with the inability to complete a treadmill test. Preclinically, dobutamine has been used in a similar manner [51], [52] and to reveal subtle phenotypic differences in conditional knockout mice [53]. The high field magnetic resonance imaging (MRI) used in this work allowed us to non-invasively characterize murine vasculature in both baseline and physiologically stressed conditions *in vivo*, with high spatial and temporal resolution.

Herein, we present in vivo quantification of the healthy venous system of murine models in the most common veins used to perform venous disease research: the common jugular vein, suprarenal inferior vena cava (IVC), infrarenal IVC, common iliac vein, and common femoral vein. Using MRI, we analyzed cross-sectional area, cyclic strain, and vessel circularity across age and sex. Additionally, we administered the cardiac stressor dobutamine to evaluate the venous response. These novel data provide foundational knowledge in the characterization of the naïve murine venous system.

2.3 Methods

All experiments were performed at the University of Michigan with approval from the University of Michigan's animal care and use committee.

2.3.1 Mice

Adult male and female C57BL/6 mice aged either 3-4 months or 15-18 months were used in this study. These ages are the human equivalent of a young adult or adult over the age of 50, respectively [54]. Data was acquired in 50 mice: n=15 young males, n=15 old males, n=10 young females, and n=10 old females; within this cohort, dobutamine was administered in n=5 mice per group. For imaging procedures, mice were anesthetized using 2% isoflurane, 1 L/min O2 carrier gas. Heart rate and respiration were monitored with ECG electrodes and a respiratory pillow, respectively (SA Instruments, Inc., NY). A PID controller was used to maintain the animal's temperature at 37±1ºC via warm air circulation through the bore of the magnet. Mean total imaging time was 1.5 hours, or 2.5 hours when administering dobutamine (approximately 1 hour with dobutamine).

2.3.2 Magnetic Resonance Imaging

Imaging was performed on a 7 Tesla horizontal bore magnet using a Direct Drive console (Agilent Technologies, Santa Clara, CA). All animals were imaged supine with the legs taped into an extended position. 3D time-of-flight (TOF) gradient echo sequences were used to acquire volumes at each of five locations: common jugular, suprarenal IVC, infrarenal IVC, iliac vein, and femoral vein (repetition time/echo time [TR/TE] 20/2 ms, field of view [FOV] 30 x 30 x 30 mm, flip angle [α] 20º, matrix 128 x 64 x 64 zero-filled to 256 x 128 x 128, number of excitations [NEX] 2, slab thickness 12 mm, imaging time 3 minutes). Coronal and sagittal maximum intensity projections (MIPs) of the venograms were used to plan cardiac-gated 2D TOF slices perpendicular to each vessel location (TR equal to the period of the cardiac cycle—approximately 180 ms, TE 6 ms, FOV $(25.6\ \text{mm})^2$, α 30º, matrix 512 x 256 zero-filled to 512^2, resolution 50 x 50 µm, slice thickness 1 mm, NEX 6, imaging time 6 minutes per location). These parameters resulted in approximately 25 voxels across the jugular vein, 31 across the suprarenal IVC, 25 across the infrarenal IVC, 17 across the iliac, and 12 across the femoral vein. The imaging parameters were chosen to enhance signal in moving blood, while maintaining a flip angle adequate to prevent saturation of the slower venous blood flow at the edge of the vessel. Twelve CINE frames were acquired across the cardiac cycle to quantify lumen expansion for each location.

2.3.3 Dobutamine Administration

In a subset of n=20 mice (5 of each sex and age group), a 30-gauge needle connected to a polyethylene catheter (PE10; Braintree Scientific) initially filled with saline was inserted into the tail vein for dobutamine infusion. Dobutamine infusion was initiated following acquisition of baseline (i.e. resting heart rate) CINE images at each of the five locations. A dosage of 40 µg/kg of body weight was infused by the tail vein catheter at a rate of 2 μL/min. Once the increased heart rate reached a steady state, CINE images were acquired using the same slice planning as the baseline acquisitions.

2.3.4 Image Quantification

Each of the five locations was analyzed for cross-sectional area, cyclic strain, and circularity using a semi-automated in-house MATLAB script. The k-space data acquired at 512 x 256 and zero-filled to 512 x 512 points in the frequency and phase encode direction were multiplied by a broad Gaussian weighting function to produce slight image blurring with a k-space attenuation chosen to have a root mean squares width of 0.8 voxels (voxel = three-dimensional pixel). This blurring step served to reduce random noise at a small cost of spatial resolution, due to the sub-voxel spatial width of our filter. The filtered data was then Fourier transformed, and the blurred image was up-sampled to obtain an image with 1024 x 1024 voxels for improved threshold searches. The added up-sampling step (implemented in MATLAB using 2D interpolation of the image) introduces information about the local derivative of voxel intensities at a vessel boundary, to better constrain the spatial location of a point identified to be on the vessel boundary by the thresholding algorithm.

To produce a reference image at a given vessel location, the 12 images acquired over the cardiac cycle were averaged. Then, a region of interest containing the vessel was defined and the voxel of maximum signal intensity was identified, allowing for 50% of the maximum signal intensity within the ROI to be used as a cutoff threshold in that frame. Starting at the maximum intensity voxel, an iterative radial search, subject to the thresholding condition, was used to find a connected patch of voxels surrounding the brightest voxel. The patch of voxels delineated the mean vessel shape. We then averaged the intensity of the patch, thus defining a reference intensity for the subsequent frame-by-frame analysis.

Each CINE frame was then examined individually, again using a 50% thresholding criterion to find the vessel, its center, and the coordinates of the voxels lying on the edge of the vessel—used to calculate vessel perimeter. The boundary coordinates were transformed to polar coordinates, taking the center found for the time-averaged image as our polar origin. Finally, the boundary data were fitted to the first 8 terms of a Fourier series, and the fit was used to calculate the area and center coordinates of the vessel by polar integration for each frame.

Green-Lagrange circumferential cyclic strain waveforms were calculated using

$$\varepsilon_i = \frac{1}{2}\left[\left(\frac{P_i}{P_{dias}}\right)^2 - 1\right] \times 100\%\ with\ i \rightarrow 1 - 12 \tag{1}$$

where P_i is the perimeter at a given frame in the cardiac cycle (i varying between 1 and 12), and P_{dias} is the minimum perimeter of the vessel across the cardiac cycle. It is worth noting that the Green-Lagrange circumferential strain measures changes in area, provided the vessel's expansion preserves its shape. In this case, a cyclic strain value of 50% corresponds to a doubling cross-sectional area. Circularity of the vessel was measured as a ratio of the average minimum and maximum axes lengths of the vessel across the cardiac cycle.

2.3.5 Statistical Analysis

All data are plotted as mean ± standard error (SEM). For location differences, groups were treated as categorical and repeated measures one-way ANOVA with Tukey's post hoc test was used to determine differences between locations. ANCOVA was used for comparisons between linear regression fits on cross-sectional area of veins distal to the heart. To determine group effects (age and sex) for baseline measurements and the effects of dobutamine, linear mixed effects modeling was used, accounting for the random effects of two separate imagers (ORP and CBC) and repeated measurements in the same subjects following dobutamine administration. An interaction term between group and treatment (dobutamine) was used to determine whether the response in treatment differed between groups. For mixed effects modeling, locations were viewed as independent and modeled separately. Significance was set at $p<0.05$. Data were analyzed using R version 3.3.2 (R Foundation for Statistical Computing, Vienna, Austria) and GraphPad Prism version 7.0 (GraphPad Software, La Jolla, CA).

2.4 Results

2.4.1 3D Maximum Intensity Projections Allowed Consistent Slice Planning Orthogonal to Veins

Coronal and sagittal maximum intensity projections (MIPs) from 3D gradient echo sequences using a 12 mm slab enabled consistent slice placement perpendicular to each vessel location in all mice (Figure 2.1). We were able to place the gated CINE TOF acquisitions based on anatomical markers, such as the renal veins and the iliac bifurcation. In locations where the corresponding artery was closely juxtaposed to the vein (infrarenal IVC, iliac, and femoral locations), we defined the vessel boundary by manually adjusting the boundaries produced by the thresholding technique.

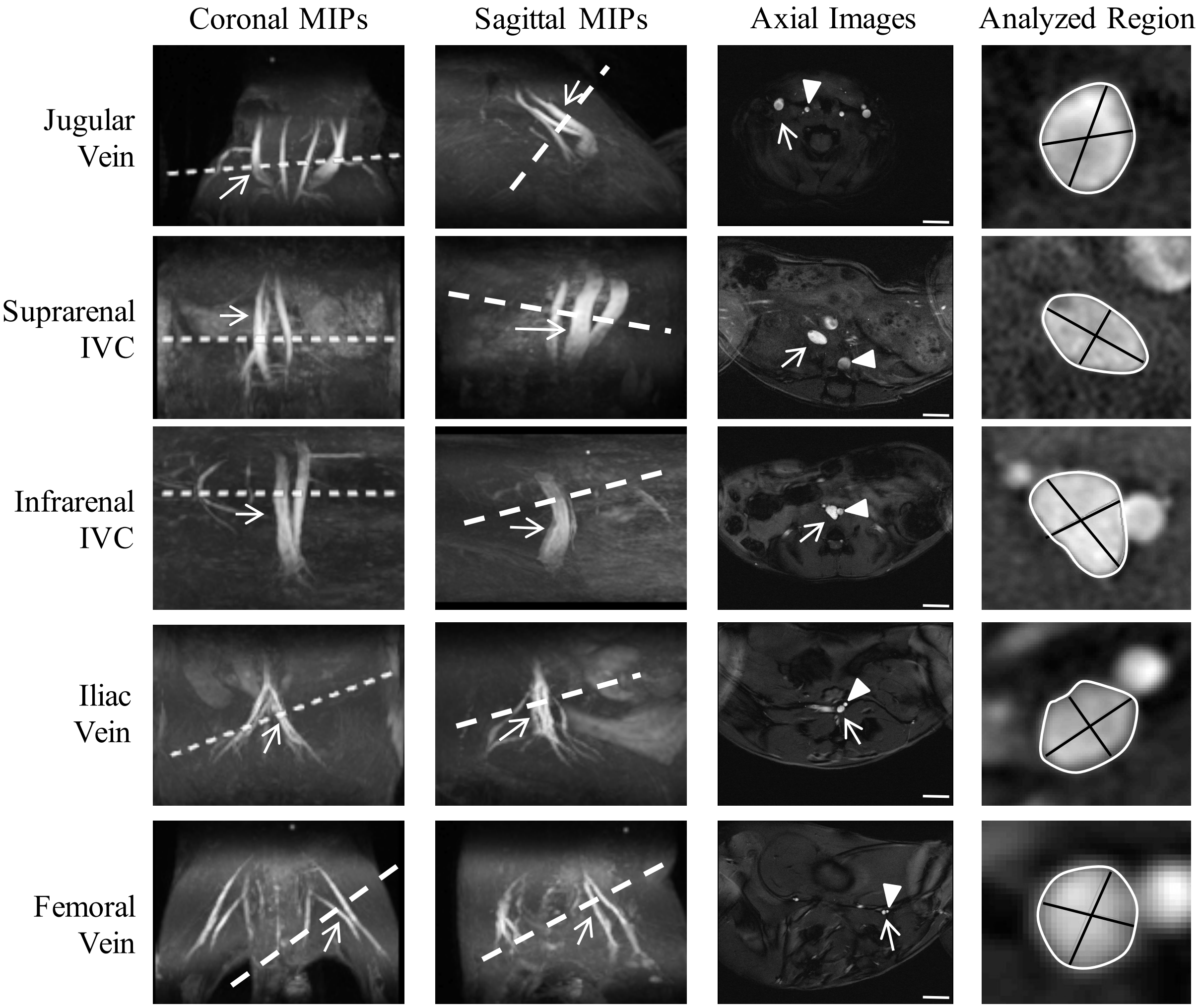

Figure 2.1 Representative maximum intensity projections (MIPs), axial images, and analyzed regions of five locations in the murine venous system. Slice planning (dashed line) is shown over coronal and sagittal MIPs. Arrows indicate vein of interest. Arrowheads in axial slices indicate corresponding artery. Venous boundaries in the analyzed regions are outlined, with the minimum and maximum axes of the vessel demarcated. Typical numbers of voxels across each vessel were: jugular=50, suprarenal IVC=62, infrarenal IVC=51, iliac=34, femoral=23. Scale bars in axial images represent 3 mm. IVC: Inferior Vena Cava.

2.4.2 Influences of Age and Sex on Vein Area Differ by Location

For age comparisons, means were adjusted for sex (μ_S); for sex comparisons means were adjusted for age (μ_A); and for location comparisons, means were adjusted for sex and age (μ_{SA}). Average body weights increased with age (μ_S: 24.2±0.4 young vs. 38.1±1.3 old, $p<0.001$) and were greater in young males compared to young females (25.8±0.4 g young male vs. 22.0±0.6 g young female, $p<0.001$). Old males were heavier on average than old females, but the weight difference was not statistically significant for our sample size of 25 old mice (39.6±1.3 old male vs. 35.8±1.4 old female).

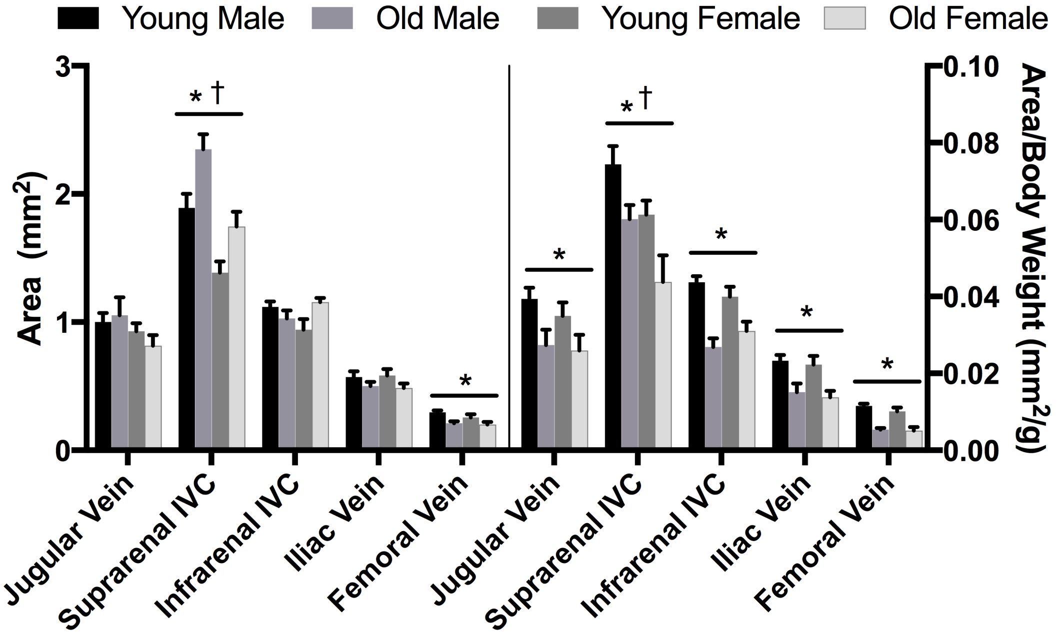

Figure 2.2 Average cross-sectional area across the cardiac cycle (mean ± SEM) at five locations in the venous system of C57BL/6 mice (left), and area adjusted to individual gram (g) body weight (right). Significant age differences denoted by *, and sex differences by †, $p<0.05$; young male n=15, old male n=15, young female n=10, old female n=10. IVC: Inferior Vena Cava.

Figure 2.2 shows the average cross-sectional area across the cardiac cycle (left) and the same area adjusted for body weight (right) at five locations for the four groups studied. Results are summarized in Table 1. The area of the suprarenal IVC increased with age (μ_S: 1.7±0.1 mm^2 young vs. 2.1±0.1 mm^2 old, p<0.001) and was larger in males (μ_A: 2.1±0.1 mm^2 male vs. 1.6±0.10 mm^2 female, $p<0.001$). Conversely, the area of the femoral vein decreased with age (μ_S: 0.28±0.02 mm^2 young vs. 0.21±0.02 mm^2 old, $p<0.001$). Cross-sectional area of the veins differed significantly along the vascular network (Table 1). Area, when plotted as a function of distance from the heart, decreases linearly from the suprarenal IVC to the femoral vein, with larger negative slopes in aged animals (slopes, R^2 values: male—young -0.052±0.003, 0.85 vs. old -0.067±0.004, 0.83, $p<0.001$; female—young -0.033±0.002, 0.80 vs. old -0.043±0.002, 0.90,

$p<0.001$). When linear regression of area was performed on individual animals, 10/15 young male, 5/15 old male, 5/10 young female, and 9/10 old female mice had slopes significantly different from zero. When adjusting for body weight, the average vessel area per gram of body weight decreased with age at every location, and the suprarenal IVC was larger in males.

2.4.3 Veins Show Minimal Circumferential Deformation Across the Cardiac Cycle

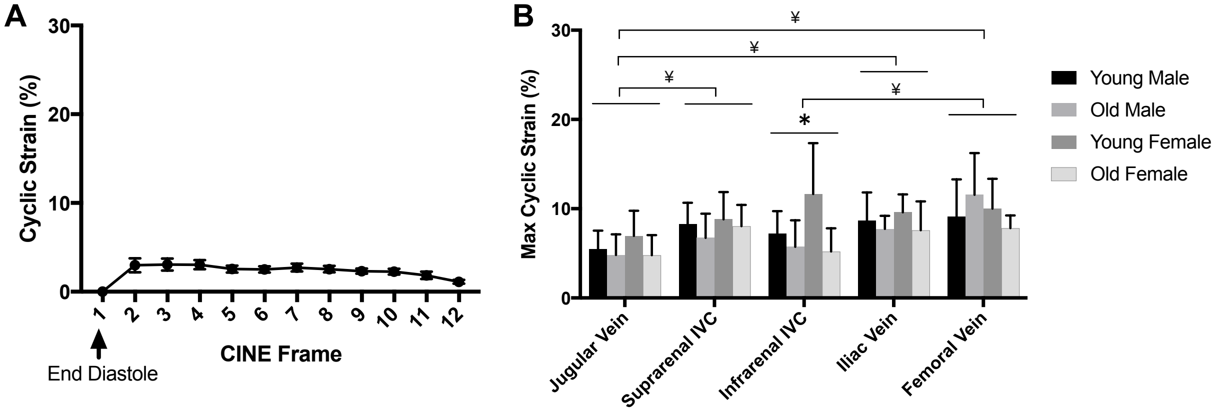

Figure 2.3 Cyclic strain values in the venous system typically remained below 10% across the cardiac cycle. (A) Representative data from n=15 young male jugular veins. (B) Maximum cyclic strain (mean ± SEM) is plotted at each location. There were no significant sex differences. Age differences denoted by *, and location differences by ¥, $p<0.05$; young male n=15, old male n=15, young female n=10, old female n=10. IVC: Inferior Vena Cava.

The veins showed little circumferential lumen expansion across the cardiac cycle, as represented in Figure 2.3A by young male jugular cyclic strain. As shown in Figure 2.3B, the maximum cyclic strain across the cardiac cycle remained below 10% with the exception of young females in the infrarenal IVC location (11.6±1.8%), and old males and young females in the femoral location (11.6±1.2% and 10.0±1.1%, respectively). Even so, in the suprarenal IVC location, max strain had a marginally significant decrease with age (μS: 8.5±0.8% young vs. 7.3±0.7 old, $p=0.05$). In the infrarenal IVC location, max strain was marginally smaller in males (μA: 6.6±0.8% male vs. 8.4±1.3% female, $p=0.06$) and decreased with age (μS: 8.9±1.1% young vs. 5.5±0.9% old, $p<0.01$). The iliac veins also had marginally decreased max strain with age

(μ_S: 9.1±0.8% young vs. 7.7±0.6% old, p=0.06). Location comparisons and the influence of age and sex on maximum cyclic strain are summarized in Table 1.

Table 1 Summary of main findings by in vivo MRI investigation of the murine venous system. ↑ indicates increase, ↓ indicates decrease.

AVERAGE AREA	MAXIMUM STRAIN	CIRCULARITY
Locations: • Veins > arteries • Suprarenal IVC > all locations • Jugular ≈ Infrarenal IVC > iliac, femoral • Iliac > femoral	*Locations:* • Veins < arteries • Jugular < suprarenal IVC, iliac, femoral • Infrarenal IVC < femoral	*Locations:* • Veins < arteries • Jugular most circular • Suprarenal, Infrarenal IVC least circular • Iliac ≈ femoral > suprarenal, infrarenal IVC
Sex and Age: • Suprarenal IVC ↑ with age, male > female • Femoral ↓ with age • Supra IVC to femoral ↓ linearly for all groups, > linear ↓ with age • Normalized to body weight, all locations ↓ with age	*Sex and Age:* • Suprarenal IVC marginal ↓ with age (*p*=0.05) • Infrarenal IVC marginal ↓ with age • Iliac marginal ↓ due to age	*Sex and Age:* • Suprarenal IVC marginal ↑ with age (*p*=0.07) • Infrarenal IVC ↑ with age • Iliac and femoral ↓ with age • Femoral: female > male
With dobutamine: • Small ↑, in general • % ↑ same across locations • Iliac greater ↑ due to age	*With dobutamine:* • Small ↑, in general (13/16 measurements) • Young male suprarenal IVC ↑ • Jugular < suprarenal IVC, femoral • No effects of age, sex, location	*With dobutamine:* • Jugular, Infrarenal IVC ↓ trend (*p*=NS) • Infrarenal IVC in young males ↓ • Femoral ↑ trend (*p*=NS)

2.4.4 Veins Demonstrate Ovular Shapes *In Vivo*

Circularity, as calculated from the ratio of minimum to maximum axes lengths of the vein, revealed differences across age and sex, as shown in Figure 2.4. The suprarenal IVC became slightly more circular with age, although this change did not reach statistical significance (μ_S: 0.61±0.04 young vs. 0.66±0.03 old, $p=0.07$), and the infrarenal IVC became more circular with age (μ_S: 0.57±0.04 young vs. 0.68±0.03 old, $p<0.01$). Conversely, the iliac and femoral locations were less circular in old mice (μ_A: 0.76±0.02 young vs. 0.69±0.04 old, $p<0.05$; 0.79±0.02 young vs. 0.74±0.03 old, $p=0.05$, respectively), with female mice having more circular femoral veins compared to males (0.74±0.02 male vs. 0.80±0.02 female, $p<0.05$).

Circularity varied by location. The jugular vein was the most circular, with circularity values significantly greater than all other veins studied (μ_{SA}: 0.86±0.02 jugular vs. 0.62±0.04 infrarenal IVC, 0.63±0.04 suprarenal IVC, 0.73±0.03 iliac, 0.76±0.02 femoral, $p<0.0001$ compared to each location). The suprarenal and infrarenal IVC locations were the least circular, and were not significantly different in circularity (0.62±0.02 and 0.63±0.02, respectively, p=NS). Circularity results are summarized in Table 1.

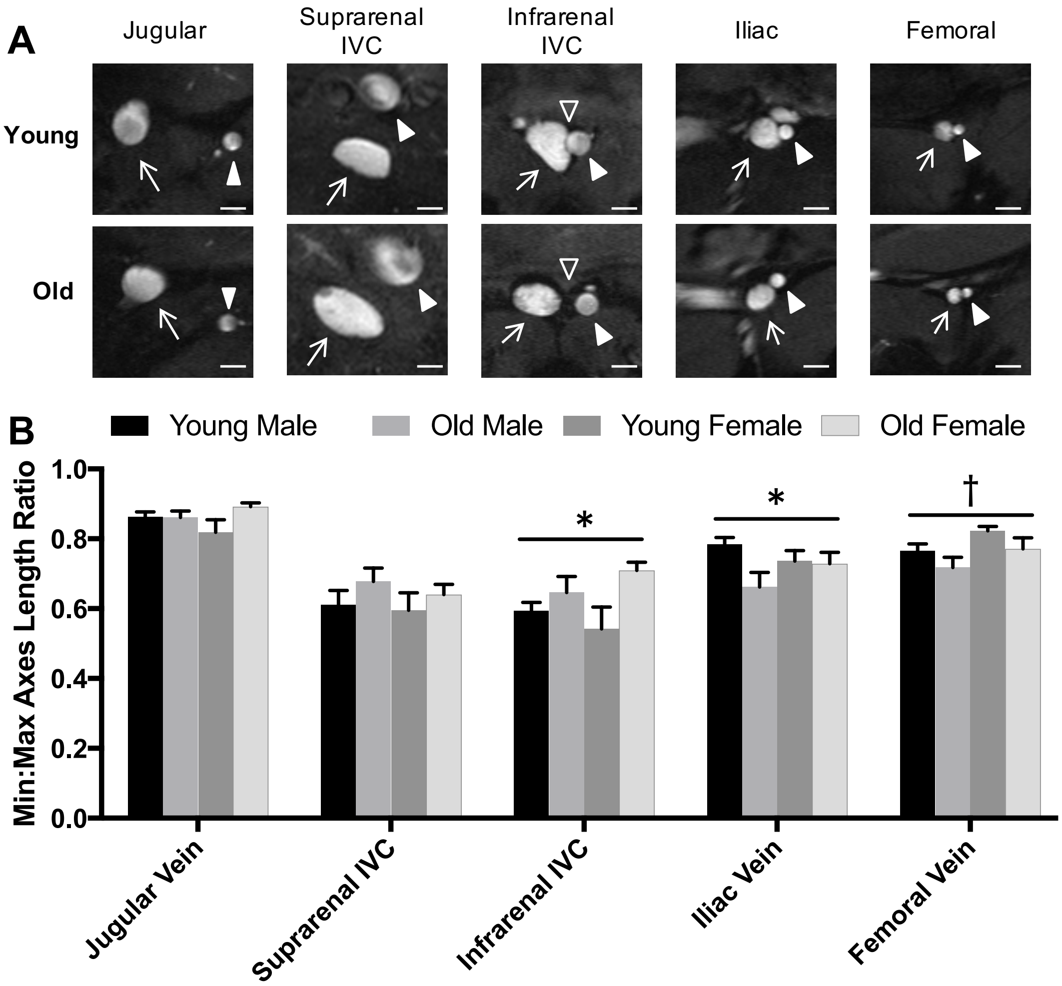

Figure 2.4 (A) Murine veins imaged in vivo tend to have oblong or irregular shapes. (A) Representative images from young and old (arrows = vein of interest, filled arrowhead = concomitant artery, open arrowhead in infrarenal IVC = artery-vein proximity difference with age). (B) Circularity (mean ± SEM), defined as the ratio of the minimum and maximum axes lengths of the vein, is plotted for each vessel location. Significant age differences denoted by *, and sex differences by †, p<0.05; young male n=15, old male n=15, young female n=10, old female n=10. Scale bars in A represent 1 mm. IVC: Inferior Vena Cava.

2.4.5 Dobutamine Has a Small Impact on the Venous System

Dobutamine infusion resulted in a 17±0.02% increase in heart rate (from resting heart rate of 508±43 to 591±15 beats per minute during dobutamine infusion, *p*<0.0001). There were no significant differences in heart rate increase between age and sex groups. The total infusion volume accounted for an average of 4.0±0.003% total blood volume (76.8±5.8 µL, assuming 58.5 mL blood/kg mouse body weight (National Centre for the Replacement Refinement & Reduction of Animals in Research, n.d.)). Figure 2.5 shows a representative image of the suprarenal IVC of an old male mouse, with the same slice acquired at baseline (Figure 2.5A) and following an increase in heart rate stimulated by dobutamine infusion (Figure 2.5C). The overlay of the two vessel segmentations illustrates a small increase in size during the second acquisition (Figure 2.5B).

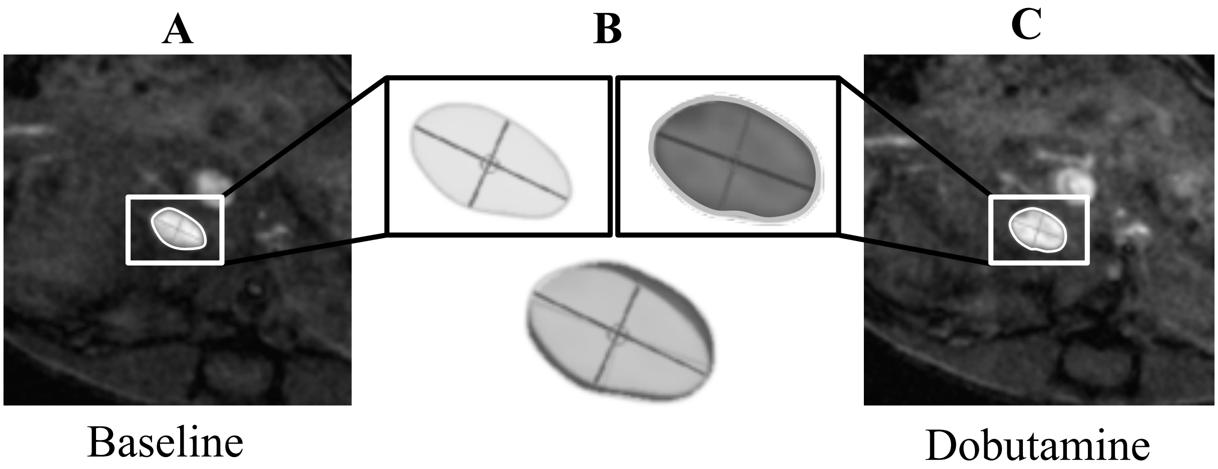

Figure 2.5 Representative images of the suprarenal IVC at baseline (A and B-light) and the same slice during dobutamine infusion (C and B-dark) from an old male mouse. When the two images are superimposed, a slight increase in area and circularity is apparent (B). IVC: Inferior Vena Cava.

2.4.6 Dobutamine Effect on Cross-Sectional Area

The change in area during dobutamine infusion, plotted in Figure 2.6, shows area increased during dobutamine-induced cardiac stress in all vessels except for young female infrarenal IVC and iliac, and young male femoral veins, which each had either zero or slightly negative change in area (a change of ≤ 20 voxels [voxel = three-dimensional pixel]). Significant increases in area due to administration of dobutamine were observed in old male jugular veins (change in area of 0.19±0.05 mm^2 or 76 voxels, $p<0.05$), old female suprarenal IVCs (change in area of 0.31±0.10 mm^2 or 124 voxels, $p<0.05$), and old female infrarenal IVCs (0.19±0.10 mm^2 or 76 voxels, $p<0.05$). In the iliac vein, the increase in vessel area was greater with age (μ_S: increase of 0.01±0.03 mm^2 young [4 voxels] vs. 0.07±0.04 mm^2 old [28 voxels], $p<0.05$), however this age effect was driven by female mice. Comparing across locations, the largest increase in vessel area was observed in the largest vessel, the suprarenal IVC, although across groups the dobutamine-driven increase in area of the suprarenal IVC was not statistically different from any other location. The change in area due to dobutamine in the jugular vein was larger than that in the femoral vein (μ_{SA}: 0.14±0.06 mm^2 jugular vs. 0.02±0.01 mm^2 femoral, $p<0.05$). Percentage-wise, however, increases in area due to dobutamine infusion were similar across vein locations (μ_{SA}: jugular 15±6%, suprarenal IVC 17±14%, infrarenal IVC 10±6%, iliac 9±7%, femoral 9±6%, p=NS across all location comparisons). The effects of dobutamine on average area are summarized in Table 1.

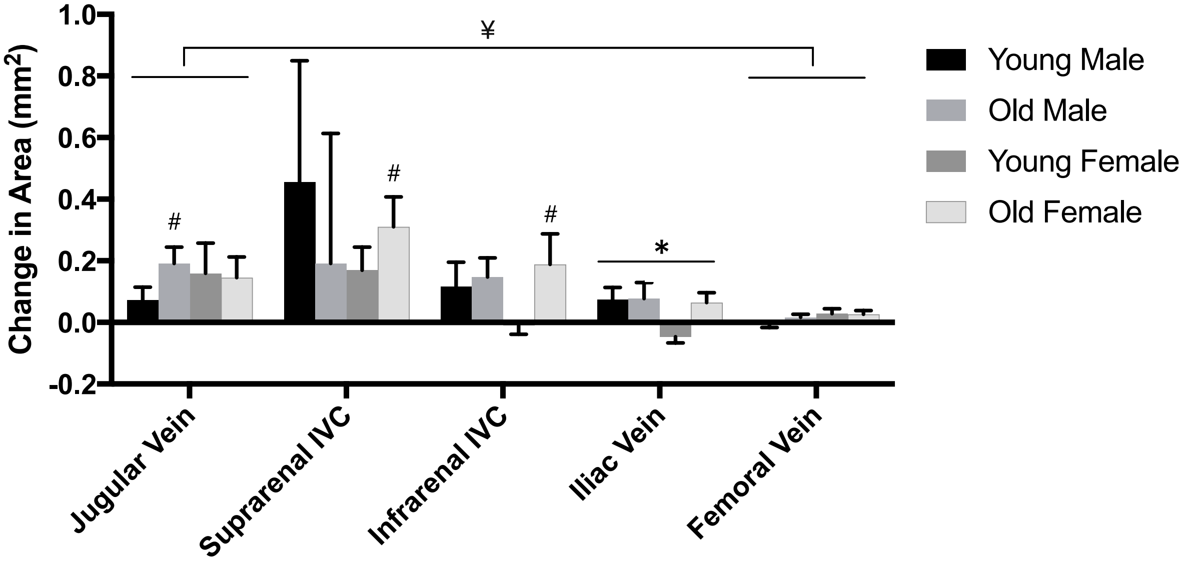

Figure 2.6 Change in area (mean ± SEM) due to dobutamine infusion is plotted for each location across age and sex. Significant changes in area under cardiac stress denoted by #, age differences in area response to dobutamine denoted by *, location differences in dobutamine response denoted by ¥, $p<0.05$; baseline measurements: n=5 across all groups. IVC: Inferior Vena Cava

2.4.7 Dobutamine Effect on Maximum Cyclic Strain

As shown in Table 2, maximum cyclic strain tended to increase slightly during dobutamine infusion (13 out of 16 measurements), but this increase was only significant in the suprarenal IVC location of young males (8.3±0.6% baseline vs. 11.6±1.1% dobutamine, *p*<0.05). Neither age nor sex nor vessel location had significant effects on the response to dobutamine as measured by the change in maximum cyclic strain. Similar relationships remained between locations during dobtuamine infusion, with max strain in the jugular vein significantly smaller than that in the suprarenal IVC and femoral vein (μ_{SA}: jugular 6.6±1.2% vs. suprarenal IVC 9.9±1.3%, $p<0.01$, femoral 9.6±1.6%, $p<0.05$). Max strain values in the suprarenal IVC, infrarenal IVC, iliac, and femoral locations were not significantly different during dobutamine infusion.

Table 2 Effects of dobutamine on cyclic strain and circularity. Results are presented as mean ± SEM. Bold text indicates values that are significantly ($p<0.05$) different from baseline. Baseline measurements: young male n=15, old male n=15, young female n=10, old female n=10; dobutamine measurements n=5 across all groups.

		Maximum Cyclic Strain		Circularity	
Location	Group	Baseline (%)	Dobutamine (%)	Baseline	Dobutamine
Jugular	Young Male	5.49±0.53	↑ 6.51±1.21	0.86±0.02	↓ 0.79±0.04
	Old Male	4.80±0.60	↑ 5.89±1.29	0.86±0.02	↓ 0.82±0.03
	Young Female	6.96±0.89	↑ 8.57±1.00	0.82±0.03	↓ 0.80±0.06
	Old Female	4.79±0.71	↑ 5.30±1.10	0.89±0.01	↑ 0.90±0.02
Suprarenal IVC	Young Male	8.26±0.62	**↑ 11.55±1.12**	0.61±0.04	↓ 0.50±0.07
	Old Male	6.73±0.70	↑ 8.65±1.04	0.68±0.04	↑ 0.73±0.09
	Young Female	8.81±1.02	↑ 10.38±1.30	0.60±0.05	↓ 0.50±0.08
	Old Female	8.04±0.76	↑ 9.15±1.60	0.64±0.03	↑ 0.65±0.05
Infrarenal IVC	Young Male	7.21±0.65	↑ 8.03±2.15	0.59±0.03	**↓ 0.47±0.05**
	Old Male	5.73±0.94	↑ 7.39±1.89	0.65±0.05	↓ 0.63±0.09
	Young Female	11.64±1.80	↑ 13.024.53	0.54±0.06	↓ 0.44±0.09
	Old Female	5.21±0.82	↓ 4.15±0.81	0.71±0.02	= 0.71±0.02
Iliac	Young Male	8.65±0.85	↑ 11.41±4.50	0.78±0.02	↑ 0.81±0.03

	Old Male	7.75±0.38	↑ 9.75±0.91	0.66±0.04	↓ 0.63±0.07
	Young Female	9.60±0.64	↓ 7.53±1.11	0.74±0.03	↓ 0.73±0.06
	Old Female	7.58±1.03	↑ 7.78±0.42	0.73±0.03	↑ 0.76±0.05
Femoral	Young Male	9.09±1.09	↓ 7.72±1.55	0.76±0.02	↑ 0.79±0.04
	Old Male	11.56±1.21	↑ 11.93±1.93	0.72±0.03	↑ 0.73±0.02
	Young Female	10.00±1.06	↑ 10.84±1.62	0.82±0.01	↑ 0.84±0.02
	Old Female	7.83±0.45	↑ 7.88±1.20	0.77±0.03	↑ 0.81±0.05

2.4.8 Dobutamine Effect on Circularity

Also shown in Table 2, dobutamine infusion had mixed effects on vessel circularity. Circularity tended to decrease in the jugular and infrarenal IVC locations during dobutamine infusion, with significant decreases in the infrarenal IVC of young males (0.59±0.03 baseline vs. 0.47±0.05 dobutamine, $p<0.05$). Circularity tended to increase in the femoral location, and a heterogeneous response was observed in the suprarenal IVC and iliac locations. Age and sex did not have significant effects on the response to dobutamine as measured by change in circularity. The same relationships between locations remained during dobutamine infusion, with the jugular vein remaining the most circular and the suprarenal and infrarenal IVC the least circular. However, during dobutamine infusion the jugular vein was no longer significantly more circular than the femoral vein due to a slight decrease in jugular circularity coupled with a slight increase in femoral circularity (μ_{SA}: 0.83±0.04 jugular vs. 0.79±0.03 femoral, p=NS). During dobutamine infusion, changes in circularity in the suprarenal IVC were greater than that in the iliac vein (μ_{SA}: change of 0.055±0.037 suprarenal IVC vs. -0.009±0.023 infrarenal IVC, $p<0.05$).

2.5 Discussion

Anatomo-physiology of the venous system in mice has been characterized in this work. Using CINE cardiac-gated MRI, we quantified venous geometry and lumen expansion at five locations in C57BL/6 mice across age and sex, at rest and during administration of a pharmacological surrogate to exercise. To the best of our knowledge, these data represent the first such comprehensive in vivo quantification in the murine venous system. We have shown that while the structure and function of veins do vary across location, they are consistently larger than arteries, deform less than arteries in the circumferential direction across the cardiac cycle, and are non-circular. The healthy venous system demonstrated only small changes when challenged by the administration of dobutamine. Age, rather than sex, more frequently influenced differences in area, maximum strain, circularity, and response to dobutamine infusion (Table 1). These methods represent an overall improvement in non-invasively quantifying the structure and function of the venous network in the most commonly-used preclinical model. Quantifying age and sex differences in normal physiological conditions provides a foundation for similar comparisons in disease models.

Venous research could be impacted by vein size such as the initial size of a vein used to host a thrombus in preclinical models. Both C57BL/6 and BALBc wild type mice, the most common backgrounds used in research, continue to increase body weight and size throughout their lifespan, dissimilar to the sigmoidal growth curve of humans [54], [55]. We quantified the influence of age and sex on venous cross-sectional area. In all five locations studied, the veins were visibly larger than the corresponding arteries (Figure 2.1 and Figure 2.4A). Without adjusting for body weight (Figure 2.2, left), there was a significant increase in vessel area with age in the suprarenal IVC. Conversely, there was a significant decrease in vessel area with age in the femoral vein. This finding is consistent with data acquired from human femoral veins using ultrasound [56] and may be related to reduced muscle mass in the lower limbs driven by a change in the activity levels of aged mice [57], [58]. Overall, four out of five locations studied showed either no difference (jugular, infrarenal IVC, iliac) or a reduction (femoral) in cross-sectional area of the vessel with age, suggesting that while mouse body weight continues to increase with age, the cross-sectional area of veins does not parallel this growth. The more rapid decrease in vein area from suprarenal IVC to femoral vein in aged animals compared to young (differences in regression slopes from data displayed in Figure 2) highlights the development of potential imbalances along the network with increasing age.

For metrics known to scale allometrically, it is common practice in research to adjust raw data to body weight when drawing comparisons between different age and sex groups. When adjusting for body weight, the area per gram of body weight decreased with age at every location. We can speculate that this consistent decrease could be attributable to a decrease in musculature coupled with an increase in fat content, which is less metabolically active than muscle and therefore demands less blood flow and, hence, less blood return [59]. For sex comparisons, males were significantly larger than females in the suprarenal IVC location, regardless of adjustments for body weight. This could be attributable to changes in reproductive capacity, as the old female mice used in this study were 7-10 months past breeding age (C57BL/6 mice typically have a reduced number of oocytes starting at 6 months of age and are retired from breeding by 8 months of age). Although the suprarenal IVC was the only location studied with significant sex differences in cross-sectional area, the relative difference between males and females (either no difference, males larger than females, or females larger than males) did not change when adjusting for body weight. This indicates that sex related differences in vein size are proportional to sex differences in body weight. These results suggest that adjusting for body weight may be appropriate when comparing across sex, but such adjustments for age comparisons could lead to misinterpretations depending on the biological question of interest. Rather, we propose that it would be beneficial to normalize data of disease models to baseline physiological metrics other than body weight when comparing across age and sex. For example, one would measure IVC length and diameter prior to inducing venous thrombosis in the IVC murine model. This could occur by gross anatomical measurement at the beginning of surgery or by imaging methods such as MRI or ultrasound.

Arterial pulsatility across the cardiac cycle is understood to be dampened before reaching the venous system. Until now, however, there was no in vivo data quantifying the presence or absence of luminal changes in the veins of mice across the cardiac cycle. Instead, the predominant data acquired with respect to the venous system has been ex vivo and focused on elucidating material properties of vessel components under non-physiological conditions (lacking tethering, blood flow, and respiration; and sometimes under supra-physiological pressures).

Lumen expansion, quantified using the biomechanical parameter of Green-Lagrange cyclic strain, showed minimal change over the cardiac cycle relative to the arterial system, maximum strain <10% compared to 19-23% in the suprarenal and infrarenal aorta [37]. This difference is one example of how quantifying in vivo venous cyclic strain provides baseline data to inform investigations of other disease states, such as arterio-venous fistula models. The jugular vein demonstrated the smallest lumen expansion across the cardiac cycle, which may be related to blood flow and pressure regulation associated with the central nervous system, even though valves are present at this location [60]. Although maximum strain in the femoral vein was only significantly different from the infrarenal IVC across age and sex groups (Figure 2.3), maximum strain values were consistently highest at the femoral location. This may be due to the fact that the femoral vein has valves that contribute to blood flow control and alter forces on the vein wall that would be relevant to measurements of circumferential cyclic strain. Alternatively, the proximity of the femoral artery may influence venous strain extraluminally. It is important to note for the femoral location, in particular, that the calculation of cyclic strain becomes more sensitive to subtle changes as vessel size decreases and the resolution limit of MRI is approached. Due to the size of the veins, this is likely less of a confounder as we were still able to achieve 23 voxels across the femoral vein. Additionally, the coefficients of variation for maximum strain did not vary significantly between locations (μ_{SA}: 0.43 jugular, 0.34 suprarenal IVC, 0.45 infrarenal IVC, 0.29 iliac, 0.36 femoral, p=NS). Interestingly, the young female infrarenal IVC group had both the largest cyclic strain and was the least circular vessel of all groups across locations (Figures 3 and 4). This could be attributable to the reproductive veins in young female C57BL/6 mice draining into the infrarenal IVC [61]. Circumferential strain in the arteries has been shown to be scale independent [62], and therefore venous strain is not normalized to body weight here.

At locations where the artery and vein are closely juxtaposed (infrarenal IVC, iliac, and femoral locations, Figure 4A, young images), the proximity of the corresponding artery and its changes in geometry over the cardiac cycle may impinge on the neighboring vein externally. As such, for locations where the artery abuts the vein, arterial conditions such as hypertension and atherosclerosis could potentially alter this effect. Understanding such factors is important to the overall health and performance of the venous system. For example, coronary artery bypass grafts, typically supplied by the saphenous vein, are prone to stenosis and thrombosis, which may be in part caused by the extraluminal biomechanical forces of the myocardium compressing the vein graft which does not have sufficient wall thickness to contest such forces [63].

Abnormal vein shape can be indicative of an underlying pathology, thus understanding the normal shape of veins is important for interpreting pathological vs. physiological geometries. We observed that the veins are typically oval, which is in part related to low pressure in the venous system. Differences in circularity between locations were evident. The jugular vein was the most circular, followed by the femoral vein. This is not surprising as pressure increases more distal from the heart, thus non-trunk veins are expected to have higher pressure relative to trunk veins. Higher pressure contributes to a more circular shape, as was observed here. Interestingly, the jugular and femoral locations are also the unique veins in this system that have valves which help regulate pressure to maintain venous return in the horizontal position (here in an anesthetized quadruped). We can speculate that venous valves contribute to circularity. Although comparable geometric comparisons along the venous network in humans is incomplete, the consistencies with human vein geometry we do see, which is dependent on the presence of valves and volume-pressure relationship [42], is noteworthy to observe in quadrupeds while under anesthesia.

Our quantification of shape again highlights the potentially under-appreciated influences of neighboring arteries in the infrarenal IVC, iliac, and femoral locations (Figure 2.4A, young images). Similar to how this intimate juxtaposition of structures may have an influence on cyclic strain, it appears to contribute to reduced circularity as well. The effect appears greatest on the infrarenal IVC of young mice, where the vessels are so closely juxtaposed that the infrarenal aorta appears ‘nested’ into one side of the IVC (Figure 2.4). The external influence of the infrarenal aorta on the concomitant IVC is reinforced by the fact that circularity of the infrarenal

IVC increased with age. Our images clearly show that while the aorta and infrarenal IVC vessels were directly next to each other in all young animals, there was a visible separation between these vessels in 13/20 old mice (Figure 2.4A, open arrowhead; 7/10 males, 6/10 females). This separation, which could be due increased fat content around the vessels often observed during surgical procedures in old mice, appears to have lessened the impact of the aorta on venous shape thus contributing to the increase in circularity with age at this location. These data suggest that a highly circular vein—particularly in the core vasculature—could be indicative of an underlying pathology. For example, in vivo studies using infrarenal IVC murine models of DVT show that in the presence of a thrombus, the IVC is greatly distended and becomes highly circular at peak thrombus size [64]. This dramatic change in vessel shape can be propagated distally into the iliac veins. Conversely, irregular vein shape in vessels that are physiologically more circular, such as the jugular or femoral veins, could be indicative of a mass such as a tumor producing changes in vessel shape. Understanding physiological conditions of vein shape provides an important reference for mouse models of disease.

Dobutamine is used clinically and preclinically as a surrogate for exercise to reveal functional arterial deficits. We used dobutamine to address whether response to cardiac stress alters the venous system, and whether those effects vary based on age and sex. Increasing cardiac output through dobutamine infusion had a relatively small impact on the venous system, whether measured by area, cyclic strain, or circularity (Figure 2.6, Table 2). While some groups of mice did see an increase in vessel area during dobutamine infusion (old male jugular, old female suprarenal IVC, and old female infrarenal IVC, Figure 2.6), this is likely attributable to a multi-factorial volume effect. During exercise, increased demand for oxygen in the muscles pulls more blood into active circulation, initially recruited from the unstressed venous reserve [65].

Dobutamine, however, stimulates ß1 receptors which increases cardiac output without stimulating skeletal muscles, thus we do not expect a decrease in venous cross-sectional area during dobutamine infusion. It is notable that the 4% increase in blood volume during dobutamine infusion did not result in significant changes in the iliac or femoral veins, across age and sex groups. This finding is consistent with the decreased compliance of veins in the extremities relative to splanchnic veins, diminishing their role as a blood reservoir [66]. The largest changes in vein area were observed in the suprarenal IVC, suggesting their important role as a reservoir in the murine venous system. Larger variability was observed in male mice, which could be due to the upstream variation in lateral branches draining into the IVC in C57BL6 mice. While the ovarian veins in female mice consistently drain into the infrarenal IVC, there is a large variability in the lateral branching patterns of male mice [67]. As such, mice with a bilateral infrarenal IVC branch phenotype may see variable downstream volume effects due to dobutamine compared to mice with no lateral infrarenal IVC branches. These results indicate that across age and sex, increasing cardiac output alone does not have a large impact on the healthy venous system. While a cardiovascular stressor such as dobutamine has been used to reveal subtle phenotype difference in cardiomyocyte-specific knockout mice [53], whether it can play the same role in murine models of venous disease will need to be evaluated.

Our study was not without limitations. First, the non-circular geometries and vessel curvature, particularly in the suprarenal IVC location, made image planning perpendicular to the vessel more challenging, and presents a source of uncertainty in the data. As such, complex vessel curvature could introduce partial volume effect biases in the cross-sectional area measurements. However, the imaging parameters optimized for this work adjusted for slower blood flow velocities, enabling us to reproducibly visualize branching structures and anatomical landmarks that led to consistency in measurements between two independent imagers (O.R.P. and C.B.C). Second, future studies of vessel pathology may require additional optimization of MRI parameters, as the bright signal intensity in TOF imaging can be influenced by blood velocity and T1 relaxation time. Thus, changes in blood velocity due to stasis or narrowing of a vessel, or changes in T1 relaxation due to the accumulation of red blood cells and methemoglobin concentration could confound TOF imaging in pathological conditions.

Third, in locations where the artery abuts the vein, manual segmentation for analysis was sometimes needed when thresholding alone was not adequate to segment the vein from the adjacent artery. Finally, irregular venous shapes were more sensitive to changes in vessel perimeter, used to determine cyclic strain.

To our knowledge, this is the first time that the structure and function of the murine venous system has been characterized non-invasively, at multiple locations across age and sex, and during application of a cardiovascular stressor. The results demonstrate that there are differences in size, luminal expansion across the cardiac cycle, and shape along the venous network and relative to the arterial system. Furthermore, location, age, and sex are relevant to consider when drawing conclusions from disease models. Our data can provide physiologically-relevant parameters to computational models and ex vivo studies. Although comparable venous data in humans is incomplete, there is harmonization of our results with available data. Being able to quantify structural and functional differences along the venous network in quadrupeds under anesthesia suggests the methodology we have developed could provide sensitive measurements of the venous system in the most commonly used preclinical rodent model. With ultrasound data in humans demonstrating marked decreases in femoral vein flow with age [56] due to a combination of reduced diameter and flow velocity, future work incorporating pressure measurements and flow velocity profiles would be useful for examining stress-strain properties and luminal biomechanical forces such as wall shear stress in vivo. We believe this work could be used as a benchmark for investigations of a variety of physiological and pathophysiolgoical conditions of the venous system. Finally, in vivo quantification of structure and function can inform ex vivo studies on the relevant physiological conditions in murine models as well as computational fluid dynamic models of the venous system, hopefully leading to a greater understanding of the biomechanics of venous diseases.

Chapter 3

Mouse Models of Venous Thrombosis: Research-Based Model-Selection Algorithm

3.1 Common Mouse Models of Venous Thrombosis

Several animal models have been developed to mimic DVT. A major preclinical approach for understanding the biology of VT and testing new therapeutics is the use of murine models, as they provide an accessible model with the availability of genetically modified strains. Many of these models have shown utility in discriminating a number of factors that can influence thrombosis—from genetic effects to therapeutic interventions—leading to a better mechanistic understanding of VT development and resolution.

The murine system has several relatively large and accessible veins. The most popularly used vein for hosting thrombosis is the IVC distal to its junction with the left renal vein. This region should not be confused with the more proximal region of the vena cava which lies just below the heart and is only accessible via thoracotomy. The IVC yields sample sizes sufficient for the study of both vein wall tissue and thrombus. The absence of valves in the IVC is a drawback of IVC models when comparing to venous thrombi in humans. The other easily accessible large veins are the jugular, the femoral and the saphenous veins. The jugular vein is less commonly used for thrombosis models in mice because of its highly branching anatomy, variable diameter with dissection or manipulation, and because it is rarely the site of VT in humans. Both the femoral and saphenous veins are directly accessible with a simple skin incision and can be used without any dissection, leaving the vein essentially in its natural bed.

Other venous systems that have been used in thrombosis research are the venules of thin-tissue structures, such as the cremaster muscle, the mesenteric microvasculature, and the ear. Although much has been gained from these venule models, they are qualitatively different, and are not categorically large veins.

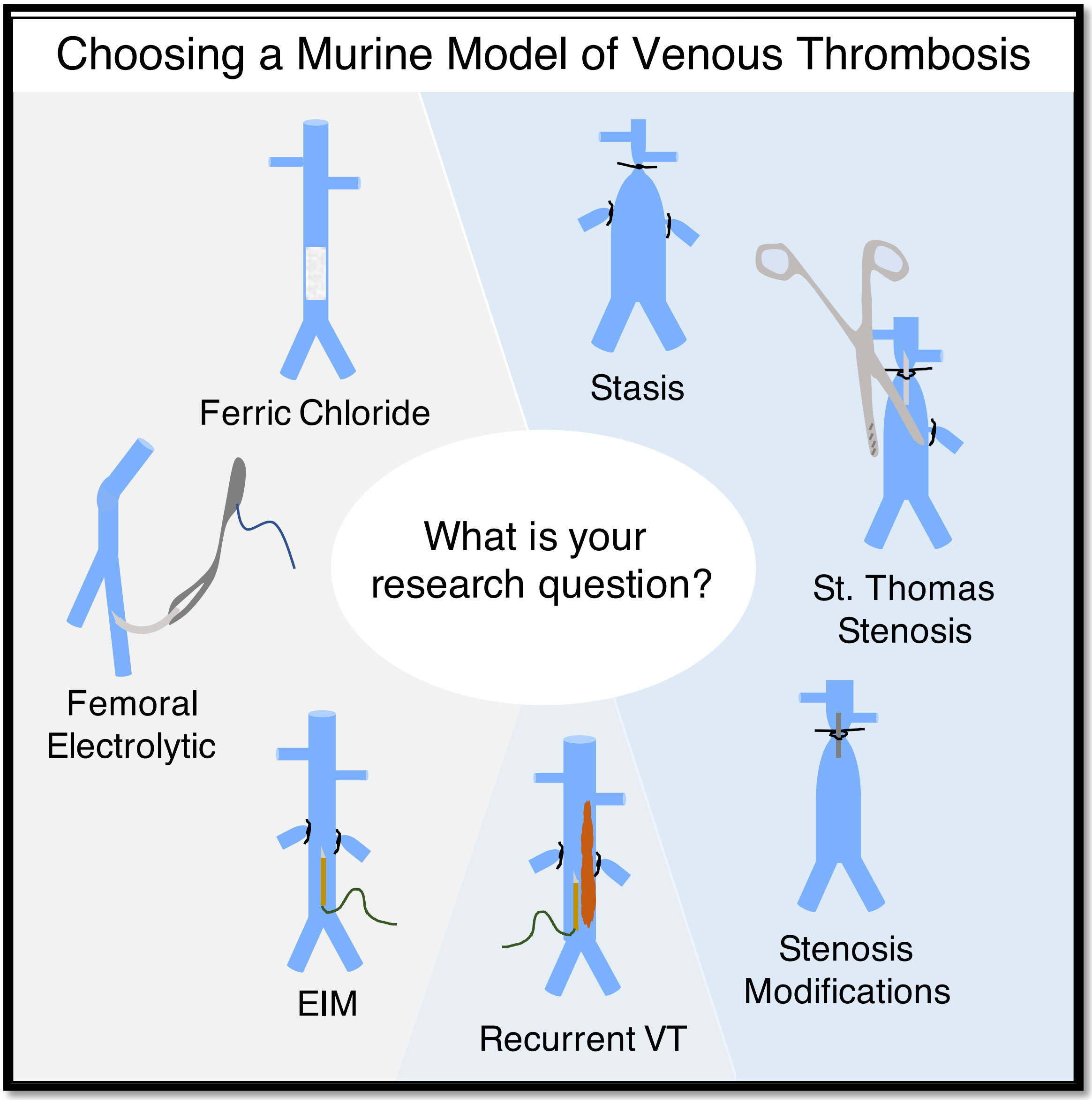

Figure 3.1 Choosing a Mouse Model of Venous Thrombosis. Representative schematic overview of common mouse models of venous thrombosis.

Thrombosis is induced by altering/stopping blood flow, or by free radical endothelial cell activation. Thrombus size is commonly used as a metric for understanding the phase of thrombogenesis, thrombus amplification, recanalization, and eventual thrombus resolution. It is important to note that these models have almost 100% survival, and to our knowledge none of the models cause pulmonary embolism. A summary of the well-characterized models is presented in Table 1, with suggested guidelines for validation of surgical technique.

Table 3 A listing of the Well-Characterized Murine DVT Models, Guidelines for Surgical Validation, and Their Advantages and Disadvantages

Model	Brief Description	Incidence of Thrombus Induction	Thrombus Size (Coefficient of Variation); Guidelines for Validating Surgical Technique	Advantages	Disadvantages
Stasis Model (Ligation Model)	Lateral branches ligated, posterior branches cauterized. The IVC is ligated with a nonreactive suture placed just distal to left renal vein	95-100%	Large (<10% variation); In 9 to 10-week-old male C57BL/6 mice weighing 25 grams, thrombus weights (IVC + thrombus at harvest) should be approximately 33 mg at day 2, 29 mg at day 6, and 18 mg at day 14.	Highly consistent thrombus size	Lack of blood flow may inhibit maximal effect of administered systemic therapeutics; thrombus forms against direction of blood flow
St. Thomas Model	Partial ligation of IVC, lateral branches interrupted, vascular clamp applied to IVC in two locations	*Strain dependent* — Balbc >90%; C57BL6 75-80%	Moderate to large (20% variation); In a 25g male BALB/C mouse, thrombus weight should be approximately 20 mg at 24 hours with a volume of 18 mm^3. C57BL/6 mice produce slightly smaller thrombi	Thrombus develops in the presence of blood flow, combines stasis and endothelial injury	Induction incidence is strain dependent; relevance of clamp injury is unclear; thrombus forms against direction of blood flow
Stenosis Model Modifications	Partial ligation of IVC without an endothelial damage step	40-100% (variable)	Small to large (85% variation)	Thrombus develops in the presence of blood flow; variability mimics that seen in humans	Variable incidence of induction; large variation in thrombus size; variation of branching phenotype introduces variability if branches are

					left open
Electrolytic IVC Model (EIM)	Small (≤250 µA) direct current applied to copper wire with the end inserted into a 25-g needle placed inside IVC on anterior wall for ≤15 min. Lateral branches ligated.	100%	*Current and time dependent* – moderate to large (<10% variation); 10-week-old 25 g C57BL/6 mice show approximate thrombus weights (IVC+thrombus at harvest) of 17 mg at 2 days, 12 mg at 6 days, and 8 mg at 14 days when induced with 250 µA for 15 min.	Thrombus forms in direction of blood flow; highly consistent thrombus size; ability to modify current or application time to fit research question	Longer surgery time required (~30+ minutes)
IVC Ferric Chloride ($FeCl_3$) Model	A piece of filter paper satured in a solution of $FeCl_3$ is placed on the IVC	100%	*Concentration and time dependent*—Small (20% variation); In 20-25g male C57BL6 mice, wet thrombus weight (separated from the IVC in saline) should be approximately 1.3 mg at 30 min following induction with 3.5% $FeCl_3$ for 3 min.	Thrombus forms in direction of blood flow; ability to modify conc. or application time	Only early time points (≤1 hour) can be studied; small thrombus size requires microbalance and may not be adequate for biochemical assays
Femoral Vein Electrolytic Model	A 1.5 to 3-volt direct current is applied to the exposed but un-dissected femoral vein (standard application of 30 seconds; modifications can range from 1s up to 2 min)	100%	*Current and time dependent*—Small (25% variation); In 12-16 week old male C57BL6 mice, thrombus histomorphometric volume should be 0.015 mm^3 at day 1 when induced with 1.5V for 30 seconds, or 0.140 mm^3 at day 1 when induced with 3V for 90 seconds.	Presence of valves in femoral vein; thrombus forms in direction of blood flow; ability to modify current or application time; vein un-dissected	Small thrombus size may not be adequate for biochemical assays

The work in this dissertation used the ligation (stasis) model and the electrolytic IVC model (EIM). However, I had the opportunity to work with leading experts in the field on a consensus of mouse models of VT. As part of my contribution, I developed a model selection algorithm to assist researchers in selecting a model appropriate for a given research question. Seven models, shown in Figure 3.1 were included based on their use and thorough characterization to enable reproducibility between laboratories.

3.1.1 Ligature Based IVC Models

Ligature models, which include stasis and stenosis models, involve the placement of a ligating or stenosing ligature around the IVC just caudal to the left renal vein to achieve stasis or low flow induction of thrombosis, respectively. The selection of this site and the various manipulations are based on the capacity to generate a sizable thrombus that can be weighed with a standard micro-balance and subsequently evaluated with Western blotting or ELISA, or processed for histology or immune-based detection of specific antigens. Surgery can be performed in 20-30 minutes, with limited surgical setup (anesthesia machine and surgical microscope). In ligature-based models, the thrombus forms in the upstream distal direction, whereas clinical VTs are generally seen to form downstream from a nidus, such as a valve pocket. This reverse direction of growth may not be trivial and requires more investigation. However, resulting thrombi have been shown to be structurally similar to human thrombi [68]–[71].

Stasis Model

The stasis model, also known as the ligation model, seeks to achieve complete stasis in the IVC, mimicking the clinical scenario of an occlusive thrombus. Any lateral or lumbar branches draining into the IVC between the left renal vein and the iliac bifurcation are interrupted, and the IVC is completely ligated. This total stasis leads to a severe vein wall reaction and nearly a 100% incidence of thrombosis. This widely used and well-characterized model produces thrombi highly consistent in size, with 10% variability [72]. A consolidated thrombus (with consistency transitioning between liquid and solid) is observed beginning 2 hours post ligation, with reported outcomes extending to 28 days in most mouse strains. It has proven valuable in the study of interactions between the vein wall and thrombus during the progression from acute (first 2-3 days) to chronic inflammation and remodeling of the vein wall [73], [74]. Retraction of fibrosed thrombus into the vessel wall is observed as a consequence of a total vein wall/thrombus retraction at chronic time points, specifically 21 days post thrombosis or further. Avoiding interruption of side and/or back branches, even due to surgical challenge, significantly reduces thrombus size and introduces variation in thrombus size between mice [67].

St. Thomas Stenosis Model

The St. Thomas stenosis model, named for its development and standardization at St. Thomas Hospital in London, involves a combination of reduced blood flow and endothelial damage (two out of three components of Virchow's triad) [75]. Posterior branches are left intact, while lateral branches are ligated, if present. The ligature, placed immediately distal to the left renal vein, is tied over a spacer such as a small length of 5-0 Prolene, which is subsequently removed to generate a ~95% reduction in blood flow. A neurovascular clamp is then applied to the vena cava wall at two locations in the upstream area for 15-20 seconds on each location sequentially, which causes apparent "bruising" and an additional thrombogenic stimulus to the vein. This model results in formation of a thrombus under low flow conditions with 90% incidence in the Balb/c mouse strain, with moderately lower rates of 75-80% incidence for the C57BL/6 strain (unpublished observational data).

Stenosis Modifications

The St. Thomas stenosis model has been subjected to several surgical modifications that are all broadly recognized under the stenosis model. Modifications avoid the endothelial damage step, and further vary in their treatment of side branches as well as the chosen spacer. One variation leaves all branches open and uses a 0.36 mm wire spacer [70], while other variations interrupt side branches and use either a 30-gauge needle spacer [69], [76]–[79], or a 0.26 mm wire spacer [80]. Experts in the field have noted that these modifications which avoid the endothelial damage step open a different and often unpredictable thrombotic process in the model. The incidence and size of the resulting thrombus is largely dependent on the variation used; ligating side branches draining into the IVC between the left renal vein and iliac bifurcation can increase incidence of thrombus induction, and the spacer used has a direct effect on the degree of stenosis. Stenosis models result in thrombi that are smaller than those induced with the stasis model. The variability of this model mirrors the variability seen in humans and this may be useful in translating findings to the clinic. Variations on the stenosis model may be useful for studying pro-thrombotic conditions [81]. This model has been used to study early thrombotic events based on the apparent simulation of the clinical low-flow risk state [70].

Up to today, models performed with stenosis in the IVC have been collectively known as "stenosis models" despite the large degree of variation in surgical technique. Due to the amount of variation combinations, it is difficult to provide independent names for each surgical technique. Therefore, when using a stenosis model, it is imperative to specify either "St. Thomas Stenosis Model" or "Stenosis Model" with a detailed description of the surgical technique in the methods section of the publication. This will clarify to the field the actual surgical approach and serve as a comparative tool between laboratories. We also encourage reviewers to ensure thorough descriptions of the specific surgical modification used in addition to citing previous papers. Importantly, thrombus variability among mice subjected to the same surgical procedure, as is common in the variations of the stenosis model, are welcomed if the research question involves variability in thrombus size, but should be reported.

3.1.2 Free Radical Thrombosis Models

Murine models of free radical induced thrombosis are achieved by either application of ferric chloride to the surface of the vein, or an electrolytic application of free radicals using non-injurious direct current to deposit metal cations (ferric ions) onto or within the vein. Importantly, free radical models induce thrombus formation in the direction of blood flow, as is observed in humans. Additionally, the surgical procedures are not as technically difficult compared to ligature-based models as no dissection is required between the IVC and aorta.

Ferric Chloride Model

Free radical induced thrombosis may be performed chemically, using the ferric chloride ($FeCl_3$) model. This model has been widely used in murine carotid artery models, and has been adapted for the IVC. A small piece of filter paper soaked in a solution of 3.5% ferric chloride by weight in water is applied to the IVC for 3 minutes [82]. This model may only be used to study very early time points (<1 hour), as the mouse cannot be safely recovered with the presence of $FeCl_3$ in the abdominal cavity. If used in the jugular or sapheno-femoral vein, however, chronic time points may be studied if the site of application is thoroughly irrigated [83]. The $FeCl_3$ applied to the IVC induces a thrombus that is typically very small, requiring an ultrasensitive micro-balance (error of measurement should be < 0.05 mg on the balance, as the thrombi are typically 1-2 mg) and offering little thrombus material for evaluation.

Femoral Vein Electrolytic Model

The femoral vein electrolytic model was designed to combine a simple method of thrombus induction commonly used in arterial models with intravital fluorescence microscopy. A 1.5-volt direct current is delivered to the surface of the exposed but un-dissected femoral vein for 30 seconds. Modifications in time—as short as 1-2 seconds and as long as 90 seconds—as well as current—up to 3 volts—can be used if a smaller or larger thrombus is desired, respectively. Thrombus can be studied in both acute and chronic time points, with resolution extending out to 28 days in larger thrombi [84]. The size of the thrombus is generally too small for weight measurements or subsequent protein analysis. The advantage is that the relatively small diameter (~0.6 mm) allows application of intravital fluorescence microscopy imaging for quantitative analysis of the development of a variety of thrombotic elements at the site of thrombus induction [85]. Additionally, the murine femoral vein has valves, which are thought to play an important role in human thrombogenesis.

Electrolytic IVC Model (EIM)

The electrolytic IVC model (EIM) induces thrombosis by constant current application to a copper wire inserted into the IVC [86]–[88]. This generates free radicals in the wire which activate endothelial cells without injuring or destroying them. Prior to needle insertion, lateral branches are ligated while posterior branches remain open. Thrombi develop quickly, forming in the direction of maintained blood flow (without causing occlusion), with consistent size which can be evaluated for weight and subsequent protein/cellular composition [88]. Electrolysis does not alter intravascular temperature, but does require a longer operative time for current application and some damage to the vein wall at the needle insertion site. It is important to note that the needle insertion causes a 0.5 mm tear in the endothelial layer, which represents 14% of the vessel perimeter [89]; insertion of the needle without current application does not induce thrombosis [88]. The EIM is recommended for the study of anti-thrombotic, thrombolytic agents or any new agents in VT treatment and prophylaxis. Recently the EIM application was expanded for the study of pro-thrombotic conditions [90], [91]. Further, imaging studies recently demonstrated the consistent thrombus size is both current and time dependent, enabling researchers to modify these parameters to create thrombi of consistent size to study both pro-thrombotic and anti-thrombotic phenotypes, supporting the modification introduced in 2015 [92]. Additionally, a new approach was recently introduced to address lack of equipment availability and high cost, following the same principles but significantly reducing equipment cost [92].

3.1.3 Recurrent Model of Venous Thrombosis

Among VT patients, 30% will suffer a recurrent episode within ten years, with 45% occurring in the ipsilateral leg leading to an increased risk of post thrombotic syndrome. The IVC recurrent VT model was thus developed to investigate this biology by producing two episodes of VT in the same animal. Because of the high rate of recurrent thrombosis in humans, this model is a novel and direct application to the human condition. The initial thrombus is induced using the electrolytic IVC model (EIM), and a secondary episode is induced 21 days later using either the EIM or a ligature-based model. At the time of induction of the secondary episode, the primary thrombus has become incorporated into the vein wall and the lumen has been recovered. Using EIM as the primary insult allows for continuous blood flow and the opportunity to induce a second episode without needing to remove any ligature. This clinically relevant model has proven valuable in the study of recurrent VT biology [93].

3.1.4 Comparison and Critique of the Models

An ideal model would recapitulate the disease onset and pathology that are seen clinically. Because of our relative lack of understanding about VT development and progression, current animal models represent our “best guess”, and thus, may lack critical features of clinical VT. A likely scenario for VT development, frequently presented by many in the field, is a low-flow or stasis state within the vein, often in a valve pocket, which can be compounded by genetic or acquired systemic prothrombotic propensity, an inflammatory state, or other factors that may enhance thrombogenesis. As such, none of the models mimic thrombogenesis in its natural form, but we can use them to study the stages of VT once a thrombus has formed.

Each model has its own unique benefits and limitations. For example, ligature-based models use slow flow or an occlusion to generate the thrombus. This is an opposite scenario to clinical VT development, for which the thrombus generates occlusion of the vein, with the exception of May-Thurner syndrome and portions of thrombus that develop distally following total occlusion. The free-radical-based models induce rapid thrombus growth and are more attuned to testing acute thrombogenesis. The maintained flow in the vein, with the possibility of thrombus regression or embolization, provides a level of relevance not available with the ligature-based models. It should be noted that while stenosis models are often thought of as blood flow models, the resulting thrombus often leads to full stasis as the thrombus occludes the site of stenosis.

While most models may be used to study both pro-thrombotic and anti-thrombotic phenotypes, the research question may lead investigators to consider the sensitivity required for detecting differences between experimental groups. For example, the IVC stasis (ligation) model creates a close to peak growth in control conditions, so it is mostly relevant for evaluating anti-thrombotic phenotypes, i.e. experimental conditions expected to reduce thrombus size. In the case of pro-thrombotic phenotypes, a large effect should be expected for adequate sensitivity when using the stasis model [71], [94]. In contrast, the stenosis model variations have a lower thrombus incidence and smaller thrombus size under control conditions, so these may be applied to pro-thrombotic phenotypic testing, with attention paid to rates of incidence between experimental groups. The EIM produces thrombi sufficiently large to test anti-thrombotic therapeutics, and may also be adjusted (decreasing the current or duration of current application) to study pro-thrombotic conditions [90].

It is of the utmost importance that publications give clear and detailed descriptions of the model with justification of any modifications used in the materials and methods section. Additionally, for rigorous science we recommend reporting data regardless of whether a thrombus developed in all mice, as variation in thrombus incidence could have important research implications. Further, robust end-point measures should be taken into consideration dependent on the model chosen during experimental design [95]. Researchers should continually strive to balance accurate and rigorous science with the highest standards of animal care, with the principles of the 3Rs (refinement, replacement and reduction) firmly in mind. Increasing the number of animals to match a representative or significant number should absolutely be avoided, unless this is highly justified towards a specific research question. An initial power calculation should be carried out based on the variability of the endpoint measure chosen in order to determine how many mice will be required [96].

3.1.5 Choosing a Model Based on the Research Question

There is no single “best” model to represent this complex disease in all its stages. Therefore, the choice of model should be based on the specific research question. Investigators should consider the clinical scenario the model should represent, including relevant time points, what outcomes will be measured, the strain of mouse that will be used, and available resources. All surgical models require a surgical microscope and anesthesia. Given the faster metabolic rate of mice compared to humans, thrombi ≤ 3 days old are considered acute, and the thrombi naturally resolve and become incorporated into the vein wall by day 28. When studying chronic VT, it can become increasingly difficult to remove the thrombus from the vein wall from 14 days following induction, which can hamper analysis.

Once a research question has been clearly defined, Figure 3.2 may provide an aid in model selection. Because a clear "best murine model" for simulating VT does not exist, a practical and more generalizable approach to experimental investigations of VT is to apply two or more different models under similar conditions, such as in evaluating new transgenic/knockout mouse lines or novel pharmaceutical therapies [79]. By using multiple mechanisms for inducing thrombus growth in a vein, a broader representation of thrombogenesis is presented for testing a potential phenotype. Relevant options for secondary models are listed under each model in Figure 3.2. The selected models should have a response range that is commensurate with the anticipated or hypothesized response.

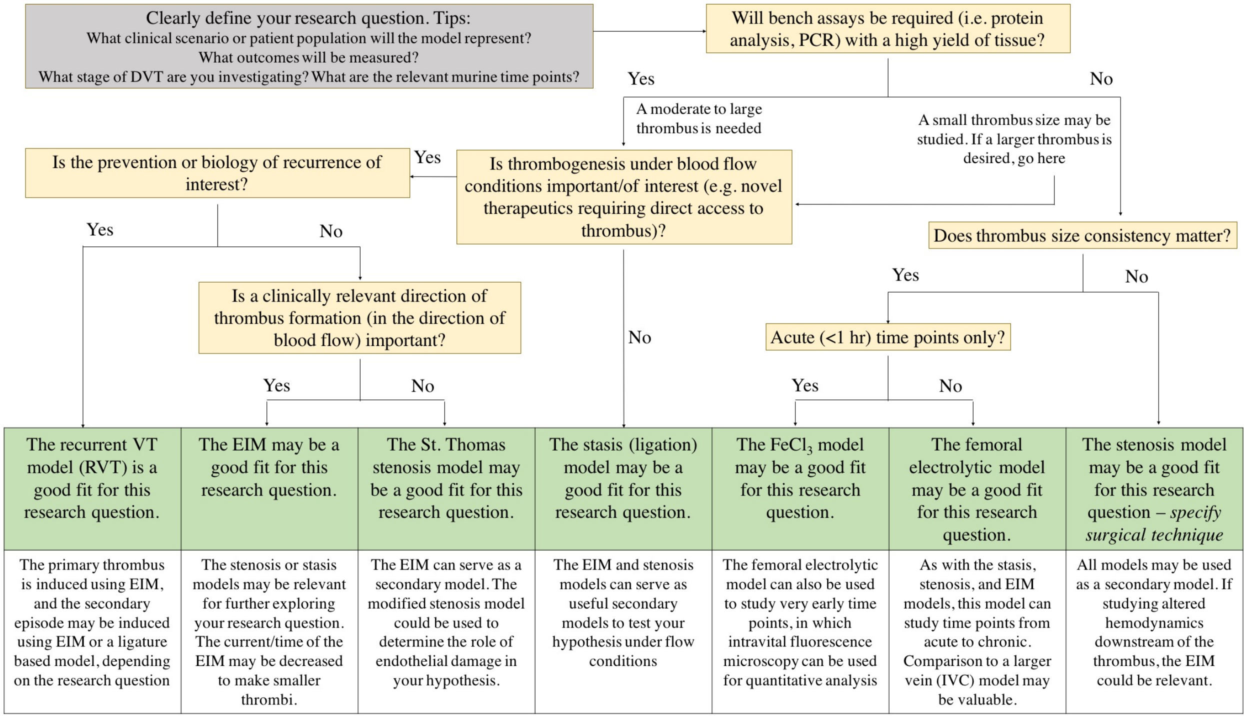

Figure 3.2 Model Selection Algorithm. This flow chart may serve as a starting point for considerations in model selection. No single model is adequate to capture the complexity of VT; thus, we recommend alternatives and secondary model options below each model. Mouse strain and sex should also be considered in model selection, as induction rates are strain dependent in stenosis models, and lateral branches draining into the IVC (common in mice from a C57 background) may not be interrupted in female mice.

Anatomic Considerations & The Use of Female Mice

In choosing a mouse strain, it is important to note the anatomical differences between mice from BALBc vs. C57BL/6 backgrounds. BALB/c mice have very few if any lateral branches compared with C57BL/6. Although posterior branches in BALB/c mice are increased in number, they are of a smaller caliber than in C57BL/6 mice. Thrombus size is generally larger and less variable in BALBc compared to C57BL/6 mice. There are, however, far more genetically-modified mice available on a C57BL/6 background.

An important note for any model requiring the interruption of lateral branches is that in female mice from the C57BL/6 background, the right uterine vein commonly drains into the IVC, with ligation resulting in necrosis of the reproductive organs [61]. Thus, if an IVC model is being used, either the stenosis model variation that does not interrupt branching vessels or the use of BALB/c mice (which typically do not present lateral branches) is recommended to study VT in females. If mice from the C57BL/6 background are used, the branching phenotype should be noted as a variable influencing thrombus size and larger numbers of animals may be required. In conclusion, there is no single “best” model to study VT, as areas of peri-thrombus blood flow and total stasis occur in human deep vein thrombosis. Model selection should be determined by the specific research question, and an additional model should be implemented to examine the experimental conditions under more than one setting. While no single mouse model can capture the complexity of VT, this method brings us closer to a rigorous understanding of the disease.

3.2 Importance of Interrupting Side Branches

Variation in thrombus size is a current concern that limits the ability to detect small differences between experimental groups. In the IVC ligation model, there has been debate over whether to interrupt branching vessels draining into the IVC [80], [97]. Leaving branches uninterrupted has been shown to significantly decrease thrombus burden and increase variability in thrombus size [67]. We aimed to understand the mechanism of this variation. We hypothesized that thrombus size variability results from altered flow dynamics involving venous branches. Using MRI, we investigated the path of blood flow in the murine IVC ligation model.

VT was induced in 11-15-week-old C57BL/6 mice (n=9) via IVC ligation with either interruption of all venous branches (IB), or all branches left open (OB). Mice were imaged by MRI 2 days post ligation to examine IVC patency and/or presence of thrombus. Venous flow was saturated to determine venous branching phenotype and flow direction, which was compared to pre-surgical MRI. Then, axial slices were acquired from the renal to iliac vessels to quantify thrombus volume. Finally, thrombus weight (TW) was quantified at harvest.

Thrombus volumes were larger in IB mice compared to OB mice (Figure 3.3, 38.0 ± 4.6 mm^3 IB vs. 11.3 ± 8.3 mm^3 OB), with greater variability in OB mice (variation coefficient 12% IB vs. 73% OB). Open branches had great impact on reducing TW due to reversed flow direction, increasing thrombus size variability. IB mice showed flow compensation through the vertebral veins and collateral vessels. At harvest, TWs confirmed MRI findings (Figure 3.3, 34.5 ± 3.8 mg IB vs. 15.7 ± 9.8 mg OB; variation coefficient 11% IB vs. 62% OB). The OB mouse with the highest TW had 2 side branches, whereas the other OB mice had 1 right branch only.

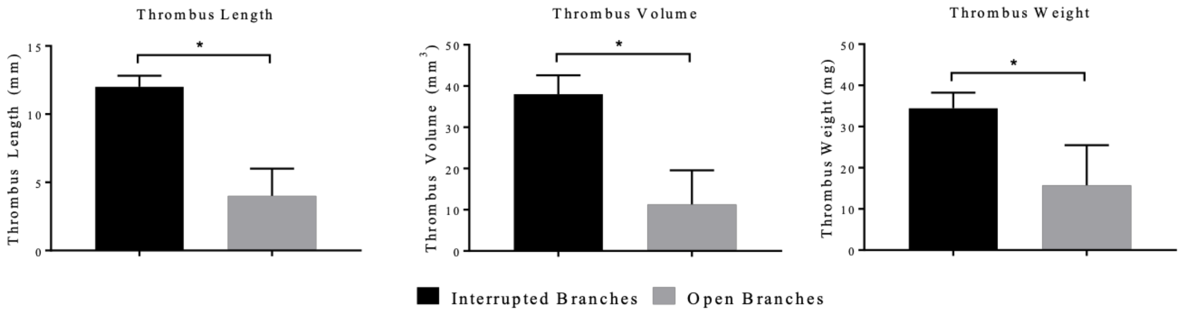

Figure 3.3 Thrombus length and volume (measured by MRI) and thrombus weight (IVC + thrombus) 2 days following IVC ligation in IB and OB mice. * indicates $p<0.05$.

Using saturation bands in a plane perpendicular to branching vessels, we observed a clear reversal of blood flow at day 2 compared to pre-surgical imaging (Figure 3.4). All of the distal back branches reversed direction, whereas only 3 of the 5 proximal back branches reversed direction (Figure 3.5). The branches where flow reversal was not detected were all occluded by the thrombus.

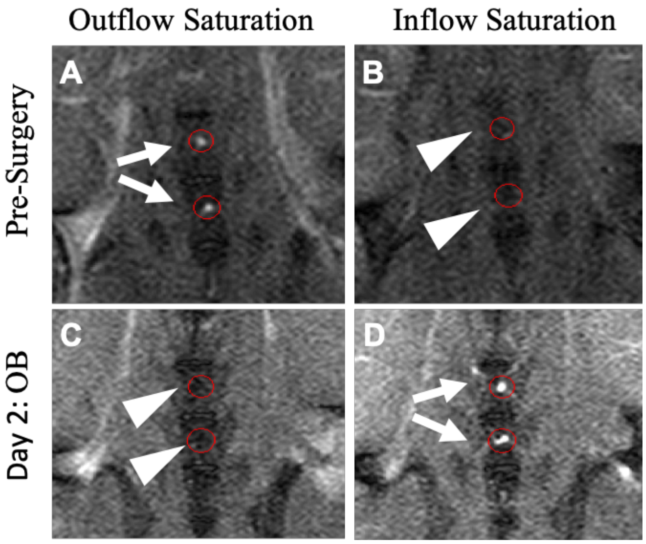

Figure 3.4 Sagittal MRI slices with saturation bands placed to saturate either outflow (veins bright) or inflow (outflow bright). Back branches flowing into the IVC prior to thrombus induction (A and B) reversed direction 2 days following IVC ligation when branches were left uninterrupted (C and D).

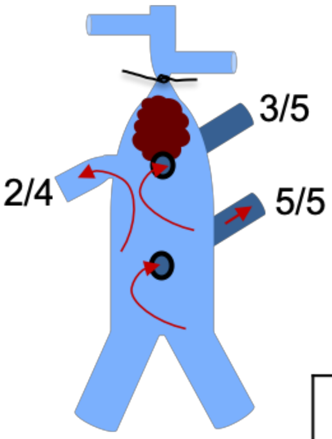

		Flow Reversal (n/N)
Side Branches	Left	-/0
	Right	2/4
Back Branches	Proximal	3/5
	Distal	5/5

Figure 3.5 Schematic representation of blood flow reversal in branching vessels. None of the mice in this study had left branches. Four mice had right branches, in which two reversed blood flow direction. All mice had two back branches; all distal back branches reversed blood flow direction, three of five proximal back branches reversed blood flow direction.

Thrombus size variability increased when branches were not interrupted. Blood flow dynamics detected by MRI were critical for understanding the “flow escape phenomenon” from the IVC that occurs through branches when they are left open. This study supports that the anatomical branching pattern affects blood flow in the IVC. Non-invasive MRI brings to light the important role of venous branches inducing thrombus variability in VT models.

The thrombus-venous interface is important in understanding the mechanisms involved in venous thrombosis. Thrombus size has a direct impact on venous wall remodeling, thus variability in thrombus size changes the impact on the vein wall. Moreover, thrombus size variability in control groups can make experimental comparisons difficult, particularly in therapeutic intervention studies. This study noninvasively explains the thrombus size variability observed when branches are uninterrupted in a venous thrombosis model. It supports the need to interrupt all venous branches in studies requiring a comparison of thrombus size between groups. By understanding the sources of variability in our preclinical models, we can control for them. This will improve conclusions derived from therapeutic studies, potentially expediting decisions to advance or reject therapeutic candidates.

Chapter 4

A Cost-Effective Flexible Pre-Clinical Tool for Studying the Fibrinolytic System in Venous Thrombosis: An Update on The Electrolytic IVC Model (EIM)

4.1 Abstract

We chose to use the EIM as one of the models in this work to represent the clinical scenario of a non-occlusive thrombus. However, the equipment used to induce thrombosis in the original model description was expensive and had since been discontinued. Further, the fibrinolytic system had not been previously studied in the EIM. Thus, I developed an equipment alternative using a voltage to current converter powered by a direct current power supply, providing an added benefit of significantly reducing costs. Additionally, we further characterized the model through mapping the current and time dependency of thrombus resolution dynamics, and investigated the fibrinolytic system from acute to chronic VT. The current and time dependency of thrombus volume dynamics was assessed by MRI, demonstrating the flexibility of the EIM to investigate both pro-thrombotic and anti-thrombotic conditions. Additionally, the fibrinolytic system was characterized in EIM. Centripetal distribution of plasminogen was observed over time, with peak staining at day 6 post thrombus induction. Both active circulating plasminogen activator inhibitor-1 (PAI-1) and vein wall gene expression of PAI-1 peaked at day 2, coinciding with a relative decrease in tissue plasminogen activator and urokinase plasminogen activator.

4.2 Introduction

The EIM was developed to simulate VT in the clinical scenario of a non-occlusive thrombus. By applying a small constant current to a copper wire inserted into the IVC, free radicals are released which activate endothelial cells and initiate the thrombotic process in the constant presence of blood flow. These conditions mimic the clinical scenario of a non-occlusive thrombus (Figure 4.1)[86]–[88]. This method produces a thrombus that is highly consistent in size. The EIM has been used in the United States and beyond to study VT in both anti-thrombotic and pro-thrombotic conditions, demonstrating the flexibility of the model [90], [91].

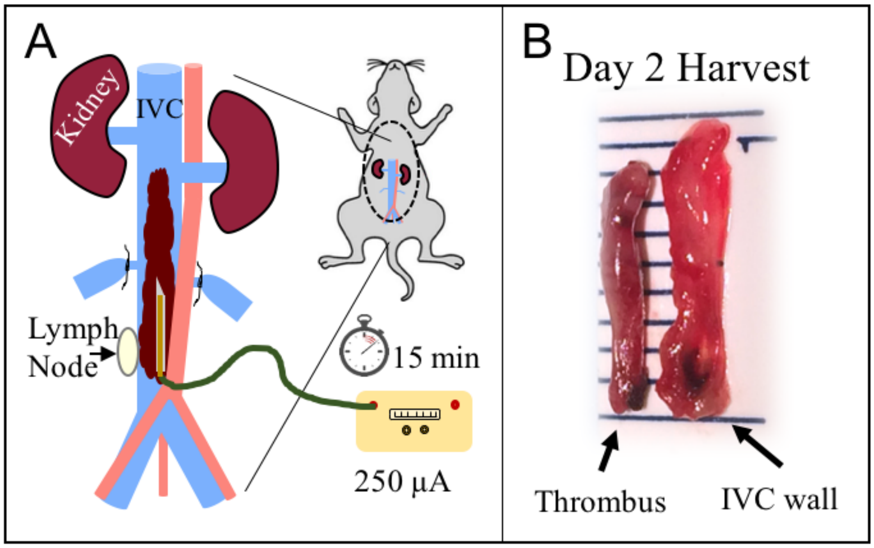

Figure 4.1 A) Schematic representation of the EIM. Any lateral branches draining into the IVC distal to the left renal vein are ligated, and a 250 μA current is applied to a copper wire placed within the IVC against the anterior wall. The right lymph node, consistently located near the bifurcation, serves as an anatomical reference for placement of the 25-gauge needle containing the copper wire. B) Gross anatomy images of the thrombus and vein wall at day 2 harvest; line markings denote mm. References: EIM – electrolytic inferior vena cava model, IVC – inferior vena cava.

Since the initial development of the EIM in 2010, several changing circumstances have driven a need for an update on the model. First, the originally described stimulator equipment was expensive and has since been discontinued. Second, the dependence of thrombus size on current and time were assumed, but had not previously been demonstrated. Third, increasing interest in targeting the fibrinolytic system for treatment of VT and the results of the ATTRACT trial emphasize a need for basic science evidence on the fibrinolytic system of thrombi in the presence of blood flow [98], [99]. The EIM provides a favorable environment for such therapeutic targets due to the sustained blood flow access to the thrombus. However, the fibrinolytic system had not previously been investigated in the EIM. In this communication, we addressed all three of these important updates; we developed an equipment alternative to the previously described system, investigated the current and time dependency of thrombus size, and characterized the fibrinolytic system in the EIM.

4.3 Methods

4.3.1 Mice and EIM Surgical Procedure

All experiments were performed at the University of Michigan with approval from the University of Michigan’s Institutional Animal Care and Use Committee and conducted in accordance with *The Guide for the Care and Use of Laboratory Animals* [100]. Male C57BL/6 mice aged 10-12 weeks were anesthetized with 2% isoflurane, placed in dorsal recumbency, and a midline laparotomy was performed. The IVC was exposed, any lateral branches were ligated using 7-0 Prolene suture (Ethicon, Inc., Somerville, NJ), and back branches remained patent. A 30-gauge silver coated copper wire (KY-30-1-GRN, Electrospec, Dover, NJ, USA) with exposed copper wire at the end was attached to a 25-gauge needle and inserted into the IVC and positioned against the anterior wall (anode). Another needle was implanted subcutaneously at the proximal end of the laparotomy incision, completing the circuit (cathode). A detailed video demonstrating the surgical technique is available [87].

A constant current of 250 μA was applied for 15 minutes for standard procedures [87]. To investigate the current and time dependency of the EIM, either the current or time was modified to 100 μA or 7.5 minutes, respectively. The current was supplied by either the previously described Grass S48 square wave stimulator and constant current unit (Grass Technologies, Astro-Med, Inc., West Warwick, RI), or by the voltage-to-current converter, described below (Figure 4.2). The direct current results in the release of free radicals within the IVC, which in turn activate endothelial cells and initiate a thrombogenic environment in the constant presence of blood flow. The needle was then removed and the abdomen closed in two layers; the muscle and peritoneum was closed with 5-0 Vicryl (Ethicon, Inc., Somerville, NJ), the skin closed with Vetbond (3M, St. Paul, MN).

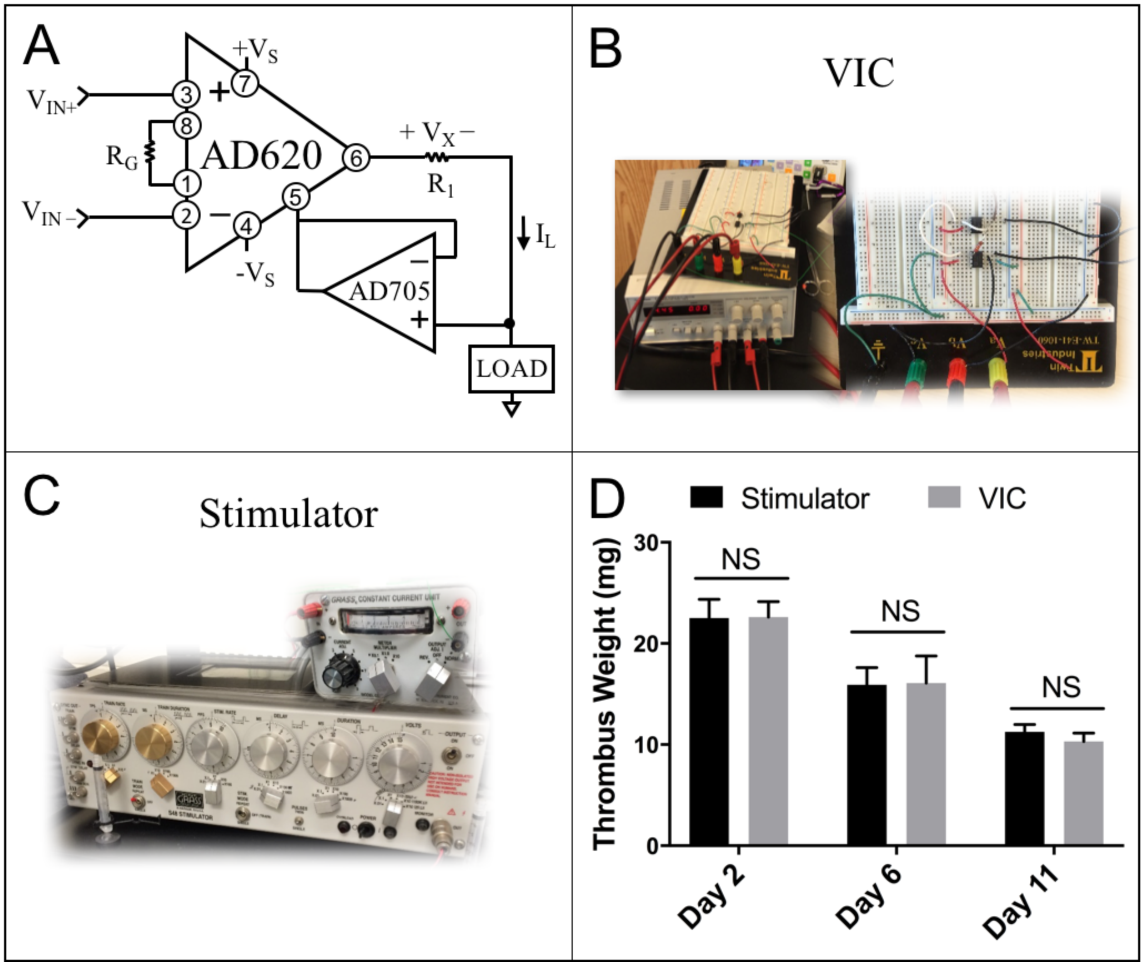

Figure 4.2 The EIM was developed using a square wave stimulator and constant current unit (C, Grass Technologies), both of which are discontinued. Construction of a standard voltage-to-current converter (VIC) – circuit diagram shown in A and constructed circuit with standard DC power supply shown in B – provide a cost-effective alternative. The VIC was validated on the benchtop and then *in vivo* by thrombus weights at days 2, 6, and 11 to the Grass S48 system (n=5 per group, mean ± SEM, D). References: EIM – electrolytic inferior vena cava model, VIC – voltage to current converter, DC – direct current, NS – not statistically significant.

Mice not undergoing magnetic resonance imaging (MRI) were euthanized at specific time points post thrombosis in order to analyze thrombus weight and perform histology, PCR, or ELISA. True controls (TC), surgically naïve mice, were utilized for baseline molecular assays.

4.3.2 EIM Equipment

EIM was performed either with the previously described discontinued stimulator and constant current unit, or with a voltage to current converter (VIC), as pictured in Figure 4.2. The AD620 operation amplifier may be used in conjunction with a second operational amplifier, such as the AD705 (DigiKey, Thief River Falls, MN). A 40 kΩ resistor (R1) was used with an input voltage of +5 and -5 volts, but the desired resistor and/or voltage may be calculated based on the input current as follows:

$$I_L = \frac{V_x}{R1} = \frac{[(V_{IN+}) - (V_{IN-})]G}{R1} \tag{2}$$

where I_L is the current applied to the load, typically 250 µA, R1 is the resistor used, V_{IN} is the positive and negative input voltage, and G is the gain. A gain resistor (R_G) is not needed for this application, so the gain (G) remains at 1. The circuit was powered by a DC power supply (Agilent E3630A, KeySight Technologies, Santa Rosa, CA). Prior to surgery, a sample load resistor (e.g. 100 Ω) was connected to the circuit and a multimeter was connected in series to fine tune the supplied voltage to deliver 250 µA (or desired current) to the load.

4.3.3 Validation and Characterization

In vivo validation of the VIC was performed by comparing thrombus weights at days 2, 6, and 11-post thrombus induction against thrombi produced using the stimulator and constant current unit. Following validation, the vein wall was isolated for qRT-PCR analysis, and 500 µL of blood was collected for circulating plasminogen activator inhibitor (PAI)-1 activity assay.

EIM was performed in a separate group of mice for immunohistochemistry at the same time points.

Additionally, to investigate the current and time dependency of the EIM, thrombus was induced in three groups: standard, 250 μA for 15 min; reduced current, 100 μA for 15 min; and reduced time, 250 μA for 7.5 min. Thrombus volume was followed over time using MRI, described below.

4.3.4 Thrombus Weight

At the time of euthanasia, the IVC and the associated thrombus were removed and weighed for wet thrombus weight. The IVC was separated from the aorta and surrounding tissue, and a segment from just below the left renal vein to the iliac bifurcation was removed for weighing. The lymph nodes were removed from the IVC prior to weighing. After determining thrombus weight, the vein wall was separated from the thrombus for subsequent assessment by qRT-PCR.

4.3.5 Thrombus Volume Assessment by MRI (*in vivo*)

The current and time dependency of the EIM was investigated in three groups of mice (standard, reduced current, or reduced time). Thrombus size was monitored *in vivo* by MRI at days 1, 2, 4, 6, 9, 11, and 14 following thrombus induction. Mice were anesthetized using 2% isoflurane and imaged supine on a preclinical 7 Tesla MRI scanner. Respiration was monitored with a respiratory pillow (SA Instruments, Inc., NY), and a PID controller was used to maintain the animal's temperature at 37±1ºC via warm air circulation through the bore of the magnet. To assess thrombus volume, 2D time-of-flight gradient echo axial slices were acquired from the renal vessels to the iliac vessels (18 contiguous slices, each 1 mm thick; repetition time 15 ms, echo time 4.9 ms, field of view 30 mm x 30 mm, flip angle 20º, matrix 256 x 256 zero-filled to

512 x 512, in-plane resolution 58.6 μm x 58.6 μm, number of excitations 3, imaging time 4 minutes). Thrombus volume was assessed by summing thrombus area in each axial slice (MRVision, Winchester, MA).

4.3.6 Quantitative Real-Time Polymerase Chain Reaction

Ribonucleic acid (RNA) was isolated from the IVC wall by homogenizing in TRIzol reagent (Invitrogen, Carlsbad, CA) per the manufacturer's protocol. Gene expression of PAI-1, tissue plasminogen activator (t-PA), and urokinase plasminogen activator (u-PA) were determined by qRT-PCR using commercially available primers (mouse PAI-1: PPM03093C, mouse t-PA PPM03855B, mouse u-PA PPM03095D) and SYBR master mix (SA Bioscience, Frederick, MD) in a Rotor-Gene 3000 thermocycler (Corbett Life Science, San Francisco, CA), as previously described [7], [72]. Gene expression was normalized to β-actin (mouse β-actin: PPM02945B) levels for each specimen.

4.3.7 Immunohistochemistry

Harvested IVC samples containing thrombus were formalin fixed for 2 hours, dehydrated in alcohol, paraffin embedded, and cut into 5 μm longitudinal sections. Nonspecific sites were blocked with normal serum, and sections were incubated with primary antibodies to Plasminogen (1:500, Genetex, Inc.; Catalog number GTX102877, Irvine, CA.) A species-specific ABC peroxidase kit (Vector Laboratories Inc., Burlingame, California) was used according to the manufacturer's instructions for the corresponding secondary antibody and subsequent steps. Color development was performed with diaminobenzidine (DAB). Mosaic images were created via light microscopy (Nikon, Tokyo, Japan) under 40x magnification and quantification of percent positive staining was performed as previously described [101].

4.3.8 PAI-1 Activity Assay

500 µL of blood was collected by cardiocentesis at harvest using a syringe with 0.05 mL of sodium citrate, and active and total PAI-1 was determined as previously described [102]. In brief, to measure active murine PAI-1 concentrations in plasma samples, human u-PA (rheotromb) was coupled to carboxylated beads (Luminex, Austin, TX) and used to capture active PAI-1. A standard curve was generated using known concentrations of murine PAI-1 in PAI-1 depleted mouse plasma (Molecular Innovations, Novi, MI). The assay was performed by adding 25 µL of either the standards or samples to a 96 well plate filter plate (Millipore, Billerica, MA). Each well then received 25 µL PBS-1% BSA and 5000 beads in 30 µL of PBS-1% BSA. The wells were incubated overnight in the dark at 4°C. The solution from each well was removed by vacuum suctioning and each well was washed twice with 200 µL PBS-0.05% Tween-20. The beads were mixed with continuous shaking in the dark at room temperature for 2 hours with 50 µL of 2µg/mL biotin-labeled rabbit anti-mouse PAI-1 (Molecular Innovations, Novi, MI). The wells were vacuum washed and 25 µL of 4 µg/mL streptavidin-R-phycoerythrin (Molecular Probes, Eugene, OR) was added to each well, and the mixture incubated in the dark with continuous agitation at room temperature for 30 minutes. Finally, the solution was removed from each well by vacuum suctioning, the beads were washed three times with 200 µL of PBS-0.05 % Tween-20, and 150 µL of sheath fluid was added for 5-10 minutes. The beads were then read with a Luminex 100 (Luminex, Austin, TX), median setting, 100 µL sample size, 100 events/bead.

4.3.9 Statistical Analysis

All statistical analyses were completed using GraphPad Prism 7 (GraphPad Software, San Diego, CA). Comparison of thrombus weight between the VIC and Grass S48 was performed using an unpaired t test with Welch's correction. A two-way ANOVA analysis using the Tukey's multiple comparison test was performed between VIC groups for the current and time dependency investigation as well as comparison of immunohistological plasminogen expression between time points. Relative expression of t-PA, u-PA, and PAI-1 in the vein wall as well as active circulating PAI-1 was compared to true controls for each time point using two-way ANOVA with Dunnett’s multiple comparison test. A p value of ≤ 0.05 was considered significant. Data was reported as mean ± standard error of the mean (SEM).

4.4 Results

4.4.1 Voltage-to-current circuit provides cost-effective system for performing EIM

We constructed a voltage-to-current converter (VIC) powered by a common DC power supply to offer an equipment alternative to perform the EIM. The development of the VIC provided an added benefit of a significant cost reduction (Table 4). *In vivo* validation of the VIC was performed by comparing thrombus size by wet weight at days 2, 6, and 11 post thrombus induction to thrombi produced using the Grass S48. Thrombus weights were not significantly different between the VIC and Grass S48 at any of the time points studied (Figure 4.2).

Table 4 Equipment required and price ranges for the previously described system compared to the VIC. Sample product numbers are provided for each component for reference. References: VIC – voltage to current converter.

Previously Described System
Stimulator: $2000-$5000 • Grass S48 Square Wave Stimulator [86] • Nihon Kohden SEN-3401 [90]
Compatible Constant Current Unit $200-$2100 • Grass CCU1 [1] • Nihon Kohden SS-203J [90]
VIC
DC Power Supply $500 • Agilent E3630A
VIC Circuit – 2 operational amplifiers, 1 resistor $10 • AD620, AD705

4.4.2 Thrombus Size in EIM is both Current and Time Dependent

The dependence of thrombus size on the supplied current and duration of application in the EIM was assessed by MRI from day 1 to 14 post-thrombosis to enable tracking of thrombus size (via volume) in the same mouse over time. Time-of-flight imaging confirmed continuous blood flow at peak thrombus size, day 2 post-thrombus initiation (Figure 4.3). Reduction of either current or time resulted in significantly smaller thrombus volume across time points compared to standards (at day 2: 20.5±1.3 mm^3 standard vs. 5.88±0.7 mm^3 reduced current vs. 5.93±0.6 mm^3 reduced time, $p<0.05$) (Figure 4.3). Interestingly, no statistical differences were found between the two modified groups. Importantly, thrombus size within each group was highly consistent between mice (coefficient of variation at day 2: controls 11%, reduced current 20%, reduced time 19%).

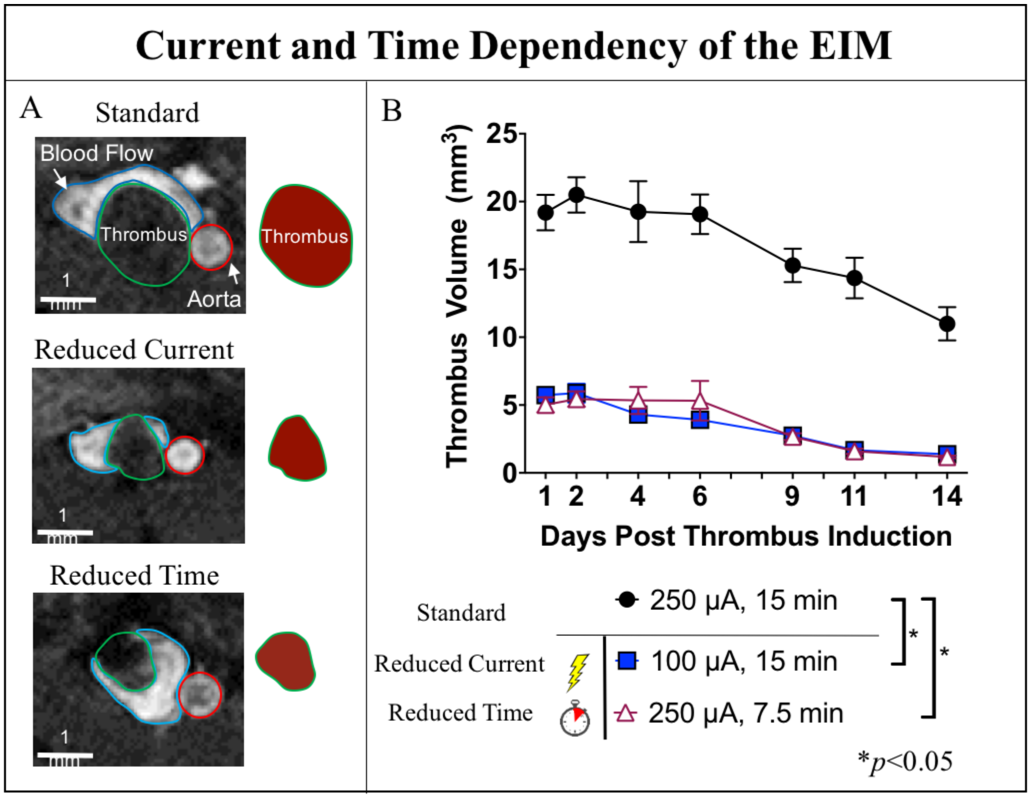

Figure 4.3 A) Contiguous axial MR images were used to quantify thrombus volume. Axial sections at the approximate midpoint of the thrombus at day 2 are shown for each group. Blood flow is visible surrounding the thrombus in all groups. The IVC is outlined in blue, the thrombus in green, and the aorta in red. Schematic representation of the thrombus is shown to the right of the

MR images to highlight the thrombus size at day 2. B) Modifications to the model demonstrate the current and time dependency of thrombus size (n=3 per group, mean ± SEM) in the EIM, as measured by MRI. Time points were compared across groups, *$p<0.05$. References: MR(I) – magnetic resonance imaging, IVC – inferior vena cava.

4.4.3 The Fibrinolytic System is Suppressed in Acute VT

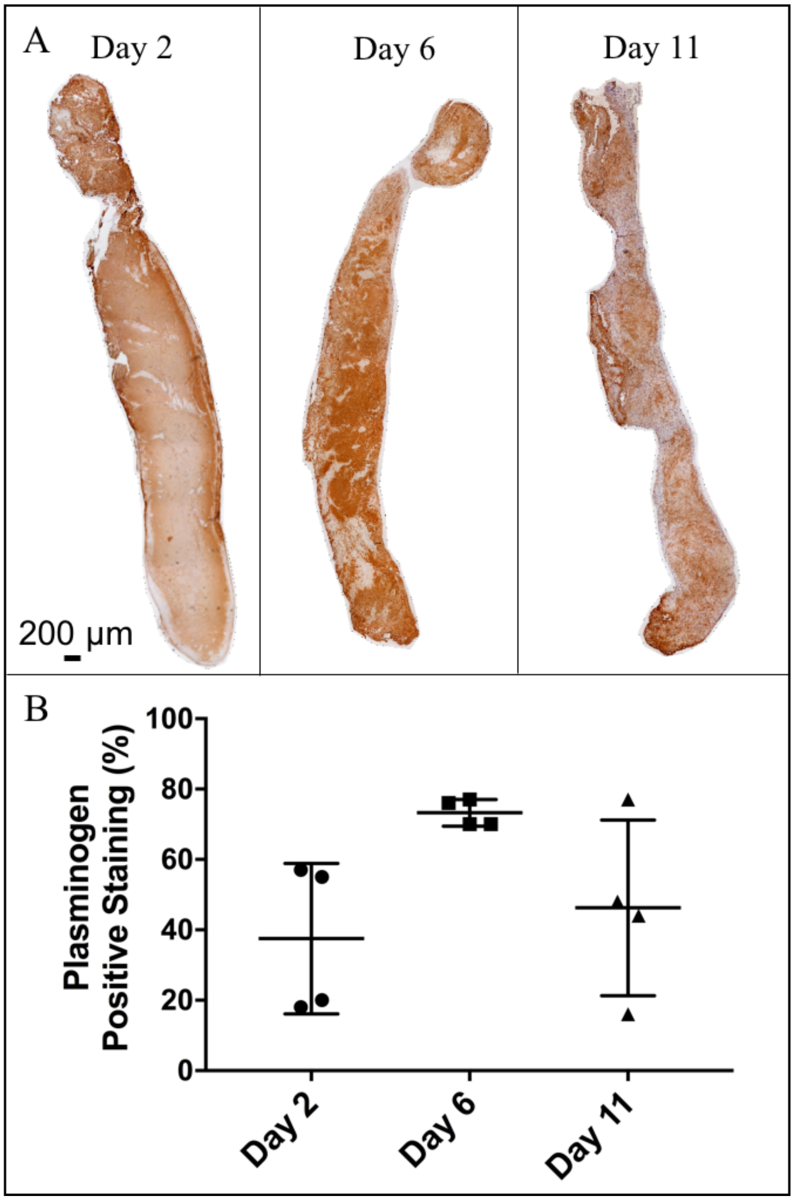

Figure 4.4 A) Representative composite longitudinal images of thrombus stained for plasminogen at days 2, 6, and 11 post thrombus induction. B) Analysis for positive staining as a percentage of total thrombus area.

The fibrinolytic system was investigated in the EIM at days 2, 6, and 11. Qualitatively, positive immunostaining for plasminogen was initially found along the perimeter day 2, with distribution throughout the thrombus at days 6 and 11. Maximum staining was measured at day 6

(Figure 4.4). Active circulating PAI-1 was significantly increased compared to true controls at days 2 and 11, with peak concentration at day 2 post thrombus induction (day 2: 2764±120 pg/mL, day 11: 1775±292 pg/mL vs. controls: 1063±140 pg/mL, $p<0.05$) (Figure 4.5). Interestingly, active circulating PAI-1 at day 6 was not different from true controls, indicating a dynamic process of thrombus burden with changing thrombus composition. PAI-1 expression in the IVC wall paralleled active circulating PAI-1 expression (Figure 4.5). Vein wall PAI-1 expression peaked at day 2, with a down-regulation trend of t-PA and u-PA at the same time point (p=NS). The opposite PAI-1 to t-PA and u-PA relationship was observed at day 11 (Figure 4.5).

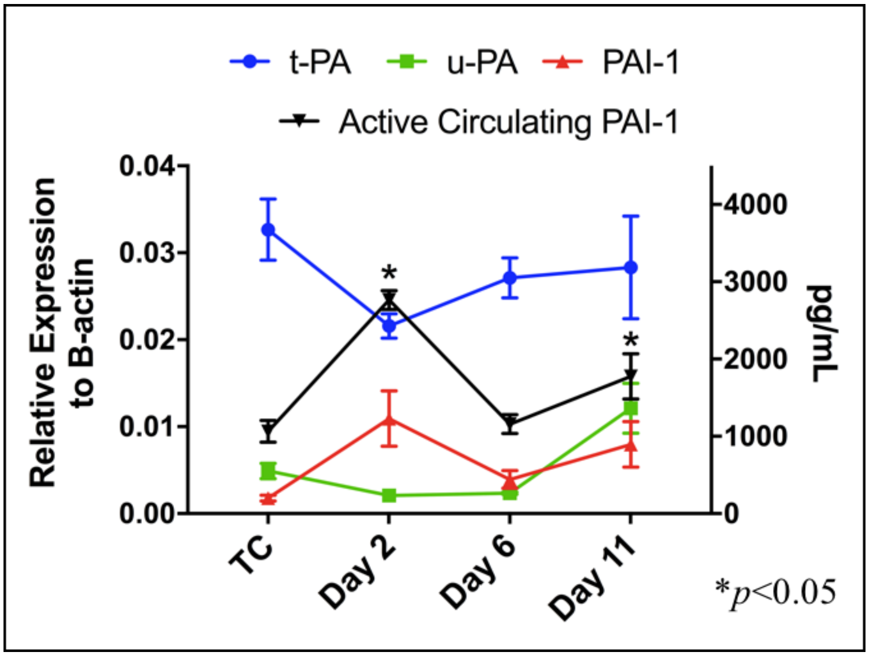

Figure 4.5 Dynamics of fibrinolytic system markers tissue plasminogen activator (t-PA), urokinase plasminogen activator (u-PA), and plasminogen activator inhibitor 1 (PAI-1) from the vein wall were assessed by qRT-PCR (left axis). Active circulating PAI-1 was assessed by ELISA (right axis). Data presented as mean ± SEM. TC – true controls (naïve animals). References: TC – true control (surgically naïve mice), qRT-PCR – quantitative real time polymerase chain reaction.

4.5 Discussion

Animal models provide critical insight to understanding the mechanisms of VT. However, there is no single model that can replicate the complexities of deep vein thrombosis. Moreover, model selection should be driven by the specific research question. Thus, a deep understanding of each available animal model including detailed characterization is necessary for choosing the appropriate model for a given research question. The EIM is the only currently available mouse model that provides both thrombus size consistency and maintained blood flow in the IVC and around the thrombus independently of the time point investigated, which is favorable for systemically administered therapeutic investigations.

The EIM was originally described using a stimulator and constant current unit from Grass Technologies to follow the procedures used by Luchessi and collaborators [103] in their canine coronary artery thrombosis model. This equipment was expensive and has since been discontinued. Alternative compatible stimulator and constant current units are difficult to find, but products from a Japanese company Nihon Kohden have been used [90]. This equipment also can be expensive, amounting to several thousands of dollars (Table 4). Thus, the high cost and discontinuation of the originally described equipment warranted an update to improve accessibility and characterization of the EIM.

Induction of thrombosis in EIM is accomplished by application of a very small constant current. In the original model description, this was regulated by the constant current unit (CCU1, Grass Technologies), which was powered by a compatible stimulator providing a very high voltage (150 V). The unit required this high voltage input to achieve accuracy in delivering 250 μA. Alternative current sources, however, do not require high voltage sources, eliminating the need for a high-voltage stimulator. Other constant current sources sold typically do not provide a range sufficiently low for this application. We chose to implement an operational amplifier constant current source for cost effectiveness, which we powered with a common DC power supply that many labs will have readily available. The VIC was validated on the bench using a multimeter and *in vivo* by comparing thrombus weight at days 2, 6 and 11, yielding results that were not statistically different from the stimulator and constant current unit. Thus, the model may be implemented at costs comparable to other murine models which only require a surgical scope and anesthesia machine.

Recently, a Japanese group presented a modification to the original EIM description to study a pro-thrombotic phenotype [90]. Typically, maximum thrombus burden is observed at day 2 with a thrombus-to-lumen ratio of 3:1 making this method very suitable to study "thrombus reduction", an attractive option when it comes to drug development and testing the potential role of pharmaceutical compounds for VT. Banno et al. adapted the original EIM by modifying the time (10 minutes instead of 15 minutes) and the current (200 μA instead of 250 μA), resulting in a smaller initial thrombus size for control mice, allowing them adequate sensitivity to detect larger thrombi in pro-coagulant mice. Their modification relied on the current and time dependency of the model, but also opened the question of how individual modifications of these variables would influence the dynamics of thrombogenesis and resolution.

Taking advantage of MRI to follow each mouse over time, we performed EIM with the original descriptive technique and in two experimental groups—one with a reduced current of 100 μA and one with reduced time to 7.5 minutes. The results of this experiment demonstrated thrombus size in this model is current and time dependent, and that these modifications still produce highly consistent thrombus size. These results corroborate the flexibility of the EIM to fine tune the model to a desired thrombus size for a specific research question. Of note, modifications served to decrease either current or time rather than increase. This is because in our experience with the development of this methodology, we concluded that 250 μA was the highest safe current without inducing off-target pathology (we observed lower limb paralysis with currents beyond 250 μA, independent of the time of application; observational data).

The recently completed ATTRACT trial investigated the impact of prompt thrombus removal via pharmacomechanical catheter directed thrombolysis (PCDT) on post thrombotic syndrome [104]. PCDT involves both mechanical and chemical lysing of the thrombus from a catheter-based device embedded within the thrombus. Currently, there are no fibrinolytic drugs with FDA approval for the treatment of VT [105]. However, the use of t-PA as a chemical lysing agent is commonly used in endovascular procedures ("off-label" use). Its mechanism of action is conversion of plasminogen into plasmin, which breaks down fibrin. Thus, studying plasminogen content in this VT model provides a platform for further investigations from both a biological and therapeutic perspective. The continuous blood flow channel in the EIM at all time points provides the possibility of direct drug access to the thrombus, even with systemically delivered therapies. However, before we move to therapeutics, the fibrinolytic system should be characterized in each animal model, as we did for this methodology (EIM). Our experiments addressed plasminogen concentration at different time points, gene expression of markers of the fibrinolytic system (PAI-1, u-PA and t-PA) in the vein wall directly in the area where the thrombus occurred, and active circulating PAI-1.

Plasminogen, the inactive precursor of the enzyme plasmin which degrades fibrin, is activated by t-PA and u-PA. Interestingly, the immunohistochemistry for plasminogen showed higher total concentrations at day 6, with plasminogen arranged from the thrombus perimeter (day 2) towards the center of the thrombus over time. This centripetal integration suggests that blood flow access to the thrombus may play an important role in the fibrinolytic process. Understanding plasminogen dynamics may provide basic science insights that could lead to a better understanding of therapeutic efficacy at different stages of VT.

PAI-1, one of the key inhibitors of t-PA and u-PA, was measured by gene expression in the vein wall and in its active circulating form. Total circulating PAI-1 correlated with PAI-1 gene expression in the vein wall, and interestingly, the peak of PAI-1 was observed at day 2, coinciding with the decreased expression of t-PA and u-PA. Taken together, this information supports that there is an impairment of the fibrinolytic system activity at day 2 (acute VT) favoring the development of a thrombus. This is aligned with previous work demonstrating that PAI-1 levels peaked at day 2 in the total IVC ligation model, which is considered a blood stasis model [102]. The impairment of the fibrinolytic system during acute VT suggests that VT is not only attributable to coagulation processes, but also a decrease in the fibrinolytic system, regardless of blood flow conditions. This insight not only improves our knowledge of the model but also increases our understanding of VT and is aligned with previous human VT publications [106].

In conclusion, we have demonstrated that the EIM can be performed using a VIC with the added benefit of reduced cost. Thrombus size in the EIM is both current and time dependent. We characterized the dynamics of thrombus resolution in reduced current and time of application experiments, further confirming the flexibility of this model to study both anti-thrombotic and pro-thrombotic conditions. Regardless of the current and time of application used, this model generates thrombi that are highly consistent in size, as was demonstrated previously with thrombus weight and ultrasound [88], and now by MRI. Additionally, the EIM can be used to investigate the fibrinolytic system under flow conditions. The functionality of the fibrinolytic system increases over time as t-PA and u-PA are up-regulated and plasminogen disseminates throughout the thrombus, providing insights for improving future therapeutic approaches. Hence, the EIM provides a cost-effective, flexible pre-clinical tool for studying the fibrinolytic system in venous thrombosis.

Chapter 5

Collateral Vein Pathways of C57BL/6 Mice: Comparative Analysis with Human Anatomy

5.1 Abstract

Unlike arteriogenesis, prolific collateralization in the venous system has been associated with more severe disease. However, there is a scarcity of information on venogenesis, and little is understood regarding the relevance of the most common preclinical model—the mouse—for studying venous collateralization. Thus, we aimed to characterize collateral vein development and progression in two murine models of deep vein thrombosis by using multiple overlapping thin slice acquisition (MOTSA) MRI. VT was induced in 12-14-week-old male C57BL/6 mice using either the IVC ligation model (n=5) or the electrolytic IVC model (n=5). Mice were imaged at 7-T on days 2, 6, 14, and 21 following VT induction. 2D time-of-flight (TOF) images with and without saturation bands to distinguish venous flow for collateral cross-section measurements at the midpoint of the thrombus and assess thrombus volume, respectively. MOTSA was optimized for collateral imaging and used to assess collateral pathway. MOTSA enabled tracking of collateral veins ≥200 μm in diameter. Collateral patterns were influenced by pre-existing anatomy; mice with bilateral IVC branches showed a predominant superficial collateral pathway (superficial and internal epigastric veins), whereas mice with no lateral branches exhibited a strong intermediate collateral pathway (gonadal and periureteric veins) and were less likely to develop ascending lumbar collaterals. The degree of venogenesis showed a positive correlation with thrombus volume ($R^2=0.64$, $p<0.0001$). MOTSA enables quantification

of murine venogenesis following IVC obstruction. Venous collateral patterns in C57BL/6 mice are consistent with those described in humans, are influenced by pre-existing anatomy, and correlate with the degree of obstruction.

5.2 Introduction

Vascular obstruction creates physical forces that promote the remodeling and maturation of pre-existing arterioles/arteries or venules/veins known as arteriogenesis and venogenesis, respectively. While arteriogenesis and therapies augmenting collateral arterial flow restore function in cases such as peripheral artery disease [107] and cerebral ischemia [108], collateral veins typically do not have valves and cannot fully compensate for impaired venous function [109]. As such, while prolific arterial collateralization reduces clinical symptoms, excessive venous collaterals are unable to restore function [109], [110] and indicate more severe disease [111], [112]. Additionally, when venous obstruction is treated by stenting, competitive flow in large collaterals increases the risk of thrombotic stent occlusion [110], making collateral size assessment an important consideration for stenting procedures.

Four collateral pathways resulting from vena cava obstruction in humans have been identified [113]–[116]. The deep pathway is the most commons in humans, involving enlargement of the azygos-hemiazygos system and/or ascending lumbar veins. The intermediate pathway involves the gonadal veins and periureteric veins, which drain into the renal veins or IVC, and is most common in humans with occlusion in the infrarenal segment of the IVC [117]. The superficial pathway involves the superficial and internal epigastric veins, also known as the external and internal mammary veins, which originate from the femoral and iliac veins and drain into the cephalic and brachiocephalic veins, respectively. The portal collateral pathway makes up the fourth pathway, with several subtypes identified following portal obstruction or hypertension.

Unlike arteriogenesis which has been extensively studied, venogenesis is poorly understood in part due to a paucity of preclinical studies. Collateral veins have been noted but not characterized in a porcine model of venous thrombosis [118] and a rat model of varicose veins [119]. A retrospective veterinary study of dogs with caudal IVC obstruction or increased flow resistance found collateral pathways similar to those reported in humans [117]. Additionally, a study using a non-human primate model of ilio-femoral venous thrombosis showed collateral veins persistent through day 21 but absent in treatment and prophylaxis groups [6]. To our knowledge, little is understood regarding the relevance of the most common preclinical model—the mouse—for studying venous collaterals.

MRI has been used to examine collateral vessels both clinically [110], [120], [121] and in preclinical models [6], [122]–[124]. Non contrast-enhanced angiography methods are increasingly desirable as safety concerns of gadolinium-based contrast agents have risen [125]. Additionally, bolus gadolinium contrast enhancement holds limited application in mice as administered contrast agents rapidly perfuse tissue, resulting in an inability to temporally separate the arterial pass from the venous pass of the contrast agent, as well as an inability to image for longer times before contrast becomes ineffective. Multiple overlapping thin slab acquisition (MOTSA) is a commonly used non contrast-enhanced angiography method that reduces signal saturation while maintaining good signal to noise ratios [126], [127], enabling visualization of collateral vessels. The purpose of this work was to characterize collateral vein development and progression in two murine models of deep vein thrombosis using high-resolution, time-of-flight (TOF) MOTSA.

5.3 Materials and Methods

All experiments were performed with approval of the University of Michigan Institutional Animal Care and Use Committee. Adult male C57BL/6 mice weighing 27 ± 2g were used in the study.

5.3.1 MOTSA Optimization

The tail arteries of naïve mice were used for optimization of MOTSA parameters because their diameter (~350 μm) is comparable to previously reported peripheral artery collateral vessels (318±20 μm) [128]. Starting values for the 3D-TOF datasets were chosen based on literal values of collateral imaging performed at 4.7 T [122]. The RF excitation thicknesses tested were prescribed as a percentage of the thin slab, with the goal of optimizing small vessel conspicuity while minimizing total imaging time for a complete volume. Because TR and FA are the most influential parameters in determining the contrast-to-noise ratio (CNR) in TOF MR angiography of blood vessels, quantitative optimization of these parameters was performed. To optimize TR, the TR was varied from 10 to 50 ms in 5-10 ms increments, while holding FA constant at 20°. Similarly, FA was optimized by holding TR constant at 30 ms, and varying FA from 10° to 90° in 5° increments.

Tail artery voxels were manually segmented from 2D axial slices derived from the 3D-TOF optimization datasets. Because a region of interest (ROI) based CNR calculation, i.e. taking the average CNR over an ROI, is sensitive to under/over segmentation when there are a small number of voxels across the object of interest (10-14 voxels for the tail artery), the maximum contrast-to-noise ratio ($CNR_{max} = MAX[(\text{signal intensity}_{vessel} - \text{signal intensity}_{tissue})/\sigma \text{ noise}]$) was determined for each slice. The average CNR_{max} and 95% confidence interval (CI) was calculated from ~55 axial slices (covering ~7 mm of resolvable vessel) for each dataset acquired for TR or FA and compared across TR or FA values.

5.3.2 Mouse Models

Two models of VT were used to represent total or partial venous occlusion. Mice were anesthetized using 2% isoflurane, their abdomen shaved, placed on a heating pad and a laparotomy was performed. The intestines were exteriorized and placed between saline-soaked gauze pads. In the total occlusion cohort, VT was induced by IVC ligation immediately distal to the left renal vein using 7-0 Prolene (Ethicon, Inc., Somerville, NJ), including ligation of any lateral branches and cauterization of both posterior branches emanating from the IVC between the left renal vein and the iliac bifurcation. In the partial occlusion cohort, VT was induced using the electrolytic IVC model (EIM), which produces an ~80% occlusion while maintaining blood flow. For EIM procedures, the stripped end of a 30G copper wire (approximately 3 mm exposed length, KY- 30- 1- GRN, Electrospec, Dover, NJ) was placed in the blunted end of a 25G needle cut to 5 mm in length. Following ligation of any lateral branches draining into the IVC, the needle with copper wire was inserted into the IVC at the level of the lymph node just proximal to the iliac bifurcation, and a second wire was inserted subcutaneously (at proximal end of incision) to complete the circuit. A voltage to current converter was used to supply a constant current of 250 μA for 15 minutes, releasing free radicals in the copper wire and activating endothelial cells within the IVC [92]. Following current application, sterile saline was applied to the IVC and the needle was carefully removed. The intestines were then placed back into the abdominal cavity and the muscle was closed with continuous sutures using 5-0 Vicryl (Ethicon, Inc., Somerville, NJ). The skin was closed with Vetbond (3M, St. Paul, MN, USA).

5.3.3 MRI

All mice were imaged on a 7 Tesla small animal MRI scanner at days 2, 6, 14 and 21 post VT induction. Mice were anesthetized with 2% isoflurane, 1 L/min O_2 carrier gas. Respiration was monitored with a respiratory pillow and maintained at 60-100 breaths/min (SA Instruments, Inc., NY). A PID controller was used to maintain the animal's temperature at 37±1 ºC via warm air circulation through the bore of the magnet. Mean total imaging time was 1.25 hours.

Collateral vessels were imaged using the optimized MOTSA parameters: TR/TE: 30/2.84 ms, FA 25°, FOV: 34 x 34 x 17 mm, matrix: 128 x 128 x 64 zero-filled to 256 x 256 x 128, in-plane resolution (132 μm)^3, NEX 2, 8 slabs each 6 mm thick with 50% overlap, imaging time 3m 25s per slap with a total of 8 slabs. Using an in-house MATLAB script (Mathworks; Natick, MA), Thin slabs were overlapped and aligned using the spatial coordinates of each dataset and merged into a single continuous 3D volume. In areas of overlap between two adjacent thin slabs, voxel pairs were evaluated individually and the highest intensity voxel was assigned to the final volume. 3D volumetric renderings of the MOTSA were used to count and classify collateral vessels.

To assess thrombus volume, 2D TOF gradient echo axial slices were acquired from the renal to iliac vessels (18 contiguous slices, each 1 mm thick; TR/TE: 15/4.9 ms, FA 20°, FOV: (30 mm)^2 x 30 mm, matrix 256 x 256 zero-filled to 512 x 512, in-plane resolution (58.6 μm)^2, NEX: 3, imaging time 4 minutes). Thrombus volume was assessed by manual segmentation (MRVision, Winchester, MA). Cross-sectional area of collateral veins was quantified at a slice 6 mm proximal to the iliac bifurcation (the approximate midpoint of the thrombus) using thresholding. To distinguish venous flow (i.e. flow directed in the superior direction), an acquisition with saturation bands placed either proximal to (saturating arterial flow) or distal to (saturating venous flow) the slice of interest was used: TR/TE: 20/4.9 ms, FA 20°, FOV: (30 mm)^2, matrix: 256 x 256, NEX 6, saturation band thickness 5 mm, imaging time 30 s.

5.3.4 Statistical Analysis

Data were analyzed using GraphPad Prism version 8.0 (GraphPad Software, La Jolla, CA). A repeated measures one-way ANOVA was used to compare collateral numbers and cross-sectional area across time points within each model. An unpaired two-tailed t-test was used to compare the two models. All data are plotted as mean ± standard error (SEM). Significance was set at $p < 0.05$.

5.4 Results

5.4.1 Multiple overlapping thin slice acquisition reveals collateral vein pathways

Collateral vessels were visualized using MOTSA optimized for imaging collateral vessels. Despite collateral tortuosity, previous studies of collateral veins have shown primarily longitudinal alignment [6], [113], [115]–[117]. Therefore, we reduced the FOV in the axial direction (thin slab direction) by half to minimize saturation effects of blood passing through the imaging volume. The matrix size was also halved to maintain isometric resolution and thus increase the changes of resolving venous collaterals in any anatomical plane. TR and FA optimization was performed on the tail arteries of naïve mice to balance high CNR with acquisition time. As shown in Figure 5.1A, a TR of 30 ms provided a comparable CNR_{max} to that of 50 ms (TR 30: 23.3 ± 3.9 vs. TR 50: 26.4±2.9) with a 40% reduction in acquisition time, while significantly improving CNR_{max} compared to a TR of 20 ms (19.5±3.4, p<0.01). Flip angle was quantitatively optimized over the same anatomical region as TR, holding TR constant at 30 ms. As anticipated, higher flip angles resulted in a higher CNR_{max}, but a lower median CNR (horizontal marks) along the length of the vessel due to TOF saturation effects as blood passes through the volume. A final flip angle of 25° was chosen because it had the greatest number of CNR_{max} measurements (78.2%) above a selected CNR value of 10, and nearly the highest median CNR (Figure 5.1B). The optimized MOTSA parameters using 50% overlap of successive acquisitions enabled visualization of collateral vessels as small as 200 μm in diameter.

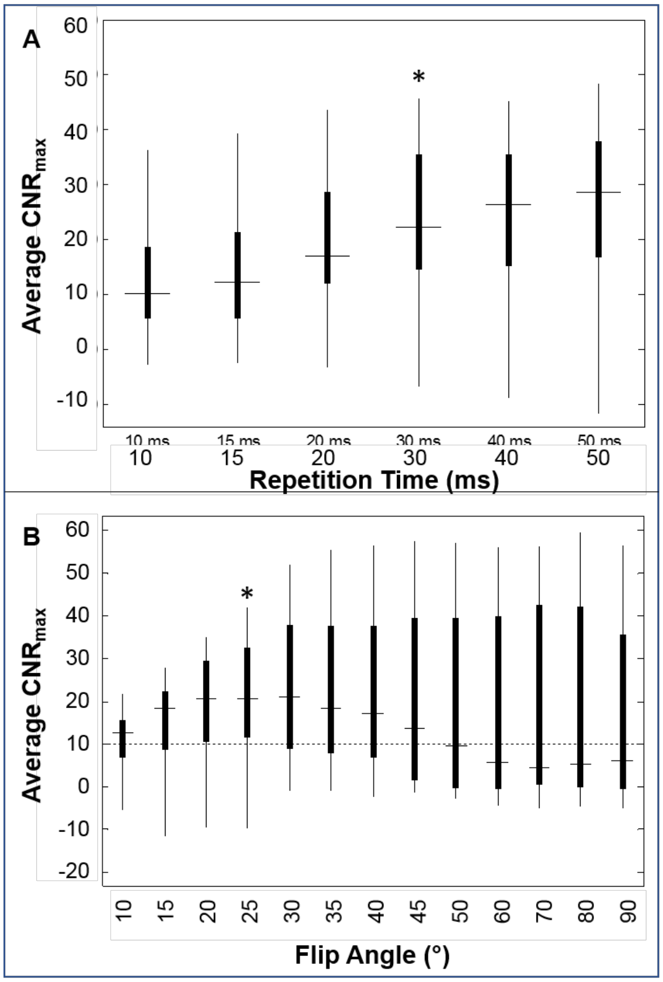

Figure 5.1 2D axial slices from single slab 3D-TOF acquisitions the tail artery of a naïve mouse were used to optimize repetition time (A) and flip angle (B). Asterisks represent the chosen parameter.

3D renderings of the stitched volume enabled tracking of the collateral vessel path. Collaterals in the extraperitoneal space showed a tortuous pattern, whereas gonadal and superficial epigastric veins took a nearly straight path (Figure 5.2, green arrowheads and blue arrows, respectively). Internal epigastric and periureteral veins showed a corkscrew pattern (Figure 5.2, white arrowheads and red arrows, respectively).

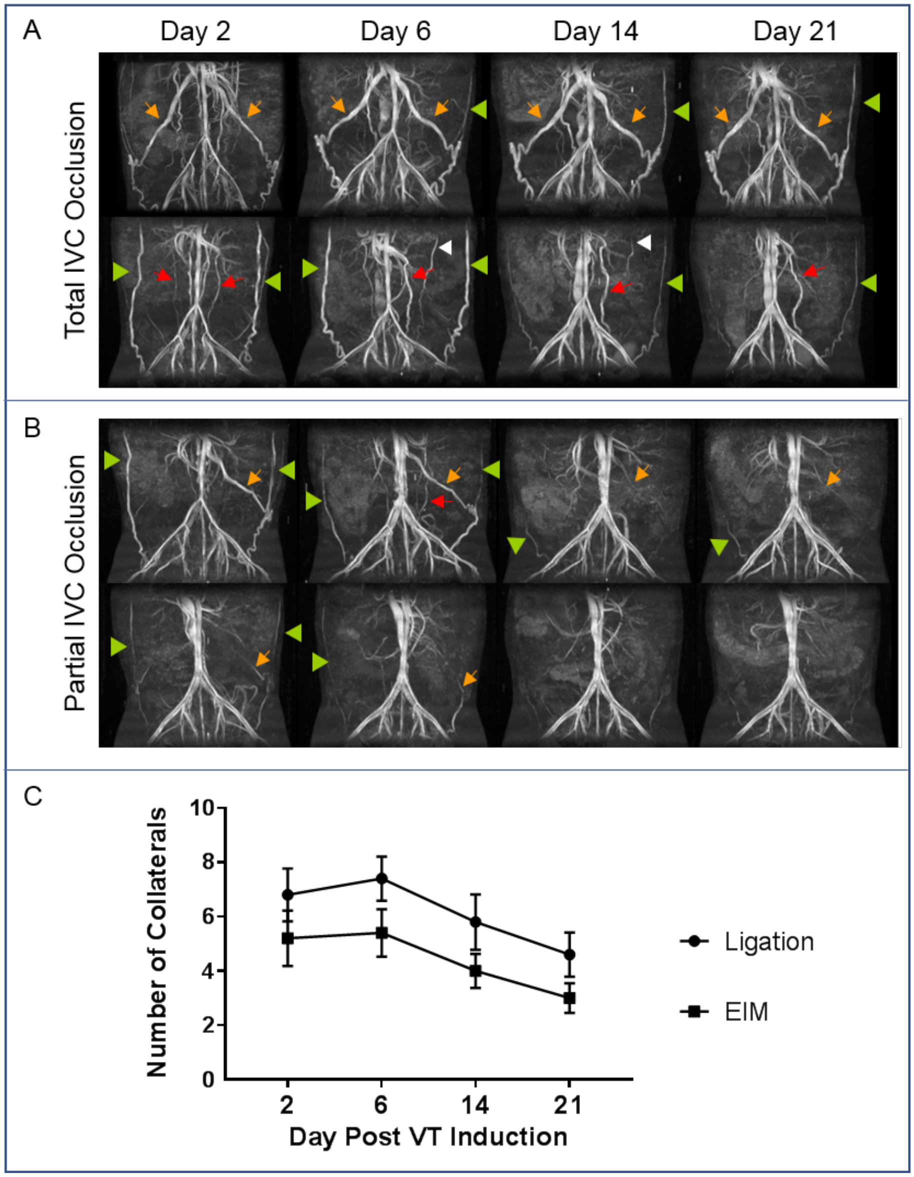

Figure 5.2 Representative coronal MIPs from MOTSA of two mice at days 2, 6, 14, and 21 following A) inferior vena cava ligation (total IVC occlusion) or B) electrolytic induced IVC stenosis (partial IVC occlusion). Green arrowheads: superficial epigastric veins; white arrowheads: internal epigastric veins; orange arrows: gonadal veins; red arrows: periureteric veins. Vertebral veins not visible in coronal images. C) Number of collateral veins over time following two models of caval thrombosis.

Collateral vessels were most prominent at early time points following thrombus induction (Figure 5.2). In both models, the number of collaterals peaked at day 6, although none of the time points studied were significantly different from one another (Ligation—D2: 6.8±0.9, D6:

7.4±0.8, D14: 5.8±1.0, D21: 4.6±0.8; EIM—D2: 5.2±1.0, D6: 5.4±0.9, D14: 4.0±0.6, D21: 3.0±0.5). While total vessel occlusion via ligation had more collateral vessels compared to partial occlusion induced by EIM at every time point, there was no significant difference in total number of collaterals between the models.

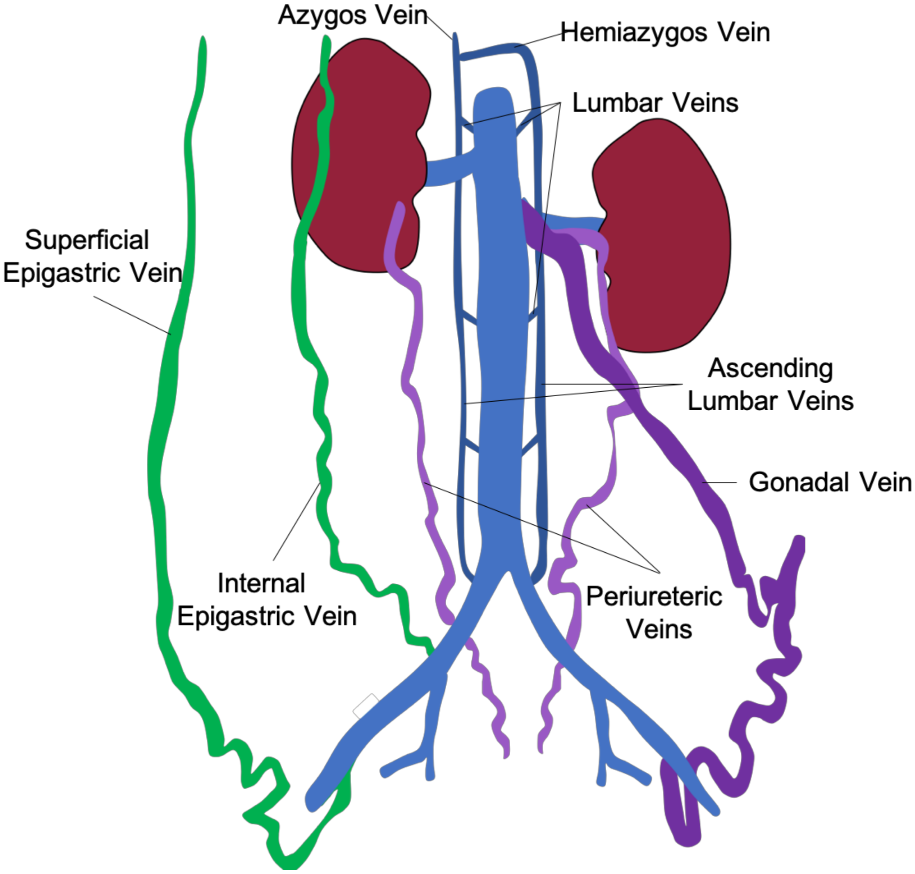

Figure 5.3 Schematic representation of the superficial (green), intermediate (purple), and deep (dark blue) collateral vein pathways in C57BL/6 mice following inferior vena cava obstruction.

Three of the four collateral vein pathways described in humans were observed in mice (Figure 5.3). Both models exhibited the deep, intermediate, and superficial collateral pathways (Figure 5.4). Deep collaterals (ascending lumbar veins, Figure 5.4A, black arrowhead) were observed in 4/5 ligation and 3/5 EIM mice, most commonly rejoining the IVC via a lumbar vein proximal to the thrombus (Figure 5.4A, white arrowhead). Interestingly, for the mice with thrombus induced by EIM exhibiting ascending lumbar collaterals, this deep collateral pathway persisted across time points, whereas in the ligation model only one of the three mice with the deep collateral pathway continued to show visible ascending lumbar collaterals beyond day 2 (Figure 5.4A). The intermediate collateral pathway was observed in all mice (Figure 5.4B). The superficial collateral pathway, also observed in all mice, was more prevalent in the ligation model (Figure 5.4C, $p<0.05$).

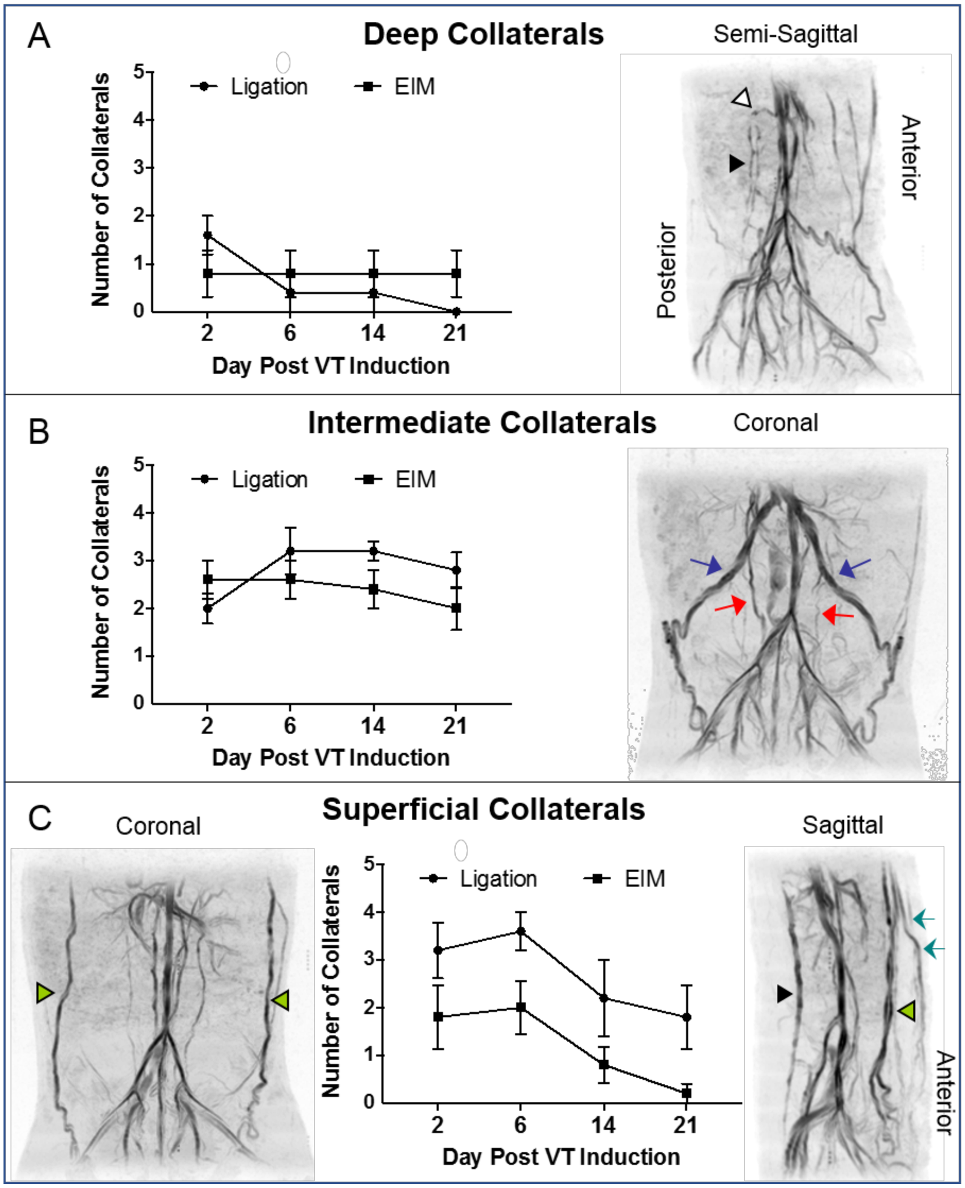

Figure 5.4 Number of collaterals in each collateral pathway with corresponding MOTSA data, inverted color scale for clarity: deep collaterals (A), ascending lumbar veins noted by black arrowhead, white arrowhead denoting the rejoining with the IVC through the lumbar vein; intermediate collaterals (B) with gonadal (blue arrows) and periureteral (red arrows) veins; and superficial collaterals (C) with superficial (green arrowheads) and internal (teal arrows) epigastric veins.

5.4.2 Collateral pattern is influenced by pre-existing vascular anatomy

The pattern of collateral vessels showed consistent trends depending on the pre-existing anatomical pattern of branching vessels draining into the IVC (Figure 5.5). C57BL/6 mice have four anatomical patterns of branching vessels draining into the IVC: no branches – 21%, right branches only – 34%, left branches only – 20%, and bilateral branches – 25%. [67] Any lateral branches that drain into the IVC between the left renal vein and iliac bifurcation are interrupted during thrombus induction for both models used. Interestingly, mice with no lateral branches tended to predominantly rely on the intermediate collateral pathway (Figure 5.5A), whereas mice with bilateral side branches predominantly exhibited the superficial collateral pathway, with some involvement of the periureteral but not gonadal veins from the intermediate pathway (Figure 5.5C). When unilateral branches were present, the side with the interrupted branch followed the superficial collateral pathway, while the contralateral side took an intermediate collateral pathway (Figure 5.5B).

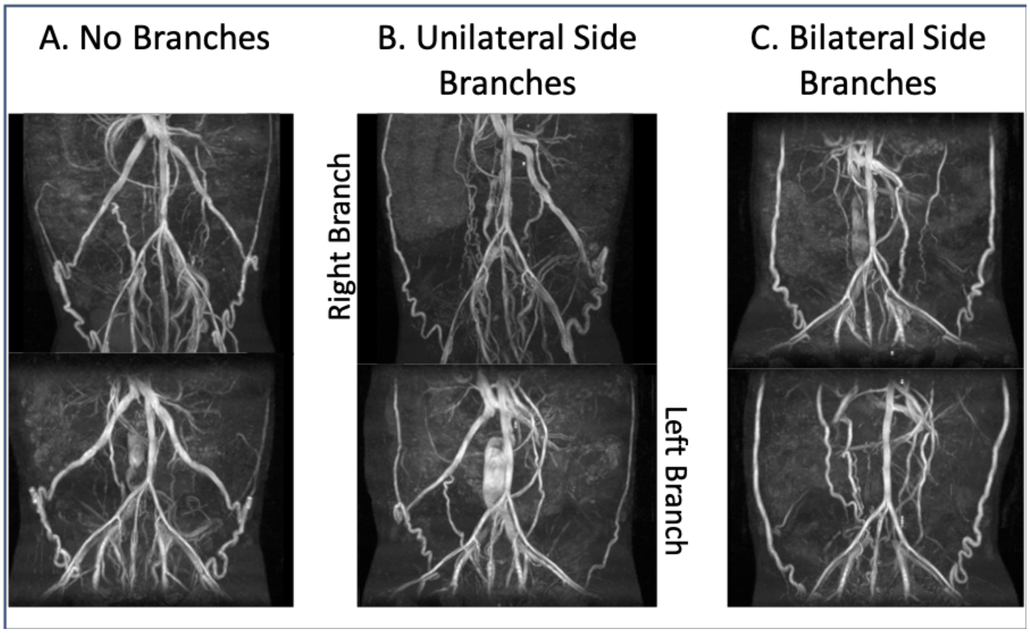

Figure 5.5 Representative coronal MIPs from MOTSA showing collateral vessel patterns in mice 6 days post thrombus induction grouped by anatomical patterns of branches draining into the IVC, which are interrupted during thrombus induction.

5.4.3 Collateral veins correlate with degree of stenosis

Measurements of collateral cross-sectional area in a slice 6 mm proximal to the iliac bifurcation (approximately the midpoint of the thrombus) were made on axial time-of-flight data using thresholding. As shown in Figure 5.6A-C, a saturation band placed first proximal then distal to the slice of interest was used to verify venous flow for measurements. Cross-sectional area of collateral vessels following total IVC occlusion by ligation was more than double that of partial occlusion by EIM (Figure 5.6D, D2: 2.3±0.6 mm^2 ligation vs. 0.8±0.4 mm^2 EIM, D6: 2.5±0.6 mm^2 ligation vs. 0.8±0.3 mm^2 EIM, D14: 1.2±0.5 mm^2 ligation vs. 0.4±0.2 mm^2 EIM, D21: 1.1±0.5 mm^2 ligation vs. 0.2±0.1 mm^2 EIM, ligation vs. EIM overall $p<0.05$). The cross-sectional area peaked at day 6 following thrombus induction in both models. In the ligation model, cross-sectional area of collaterals at days 14 and 21 were significantly smaller than at day 6 ($p<0.01$). In the EIM, cross-sectional area of collaterals at day 21 was significantly smaller than at day 6 ($p<0.05$).

In both VT models, the thrombus naturally resolves over time, with peak thrombus burden at day 2. To determine whether the blood volume diverted to collateral vessels correlated with the degree of IVC obstruction at the same time point, a linear regression of collateral cross-sectional area vs. thrombus volume from both models across time points was performed (Figure 5.7). The cross-sectional area of all collaterals at a slice approximately 6 mm proximal to the iliac bifurcation showed a significant correlation with thrombus volume ($R^2=0.64$, $p<0.0001$).

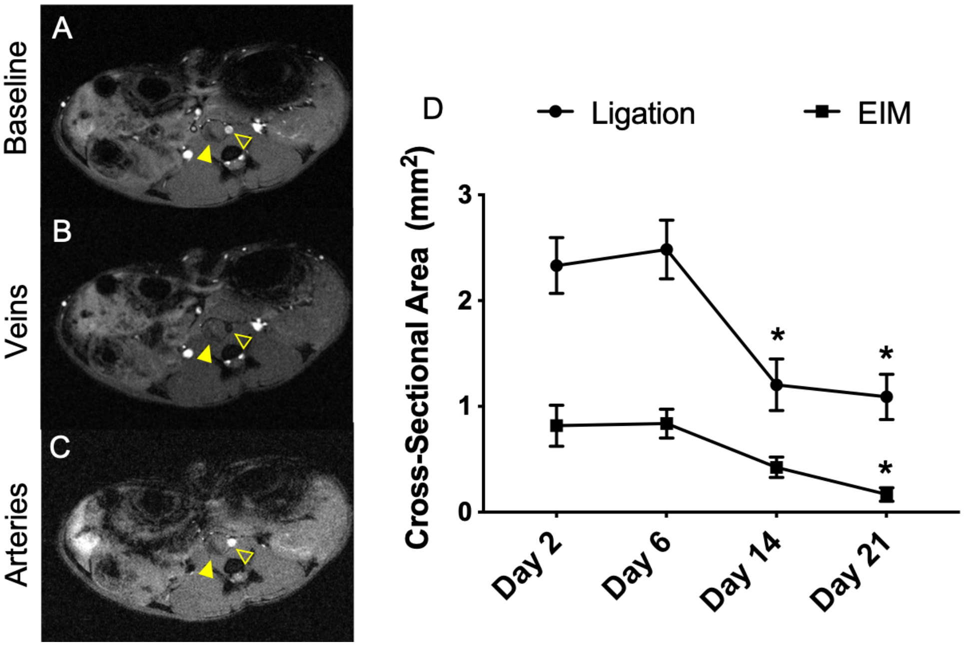

Figure 5.6 Representative axial time-of-flight image at baseline (A), saturating arterial flow to show venous collaterals (B), and saturating venous flow to show arteries (C). D) Collateral vein cross-sectional area from a cross-section taken 6 mm proximal to the iliac bifurcation. * denotes difference from the same model at day 6, $p<0.05$.

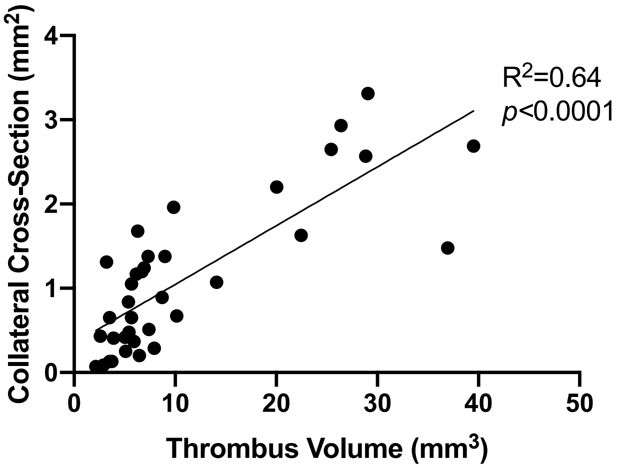

Figure 5.7 Collateral cross-sectional area correlates with the degree of vessel occlusion ($R2 = 0.64$, $p<0.0001$). Data is from two models of inferior vena cava thrombosis (partial or total occlusion) at days 2, 6, 14, and 21 following thrombus induction.

5.5 Discussion

Using two well-established mouse models of VT, we have quantified the endogenous venogenic response to IVC thrombosis through high resolution MOTSA. Three of the four collateral pathways previously reported in humans were observed in mice. As in humans, the degree of collateralization correlated with the amount of obstruction [110], [111]. The ligation model, which produces a total stasis environment in the IVC and larger thrombi than the EIM, had larger collateral vessels at all time-points compared to EIM. In mouse models of VT, the thrombus size peaks at day 2 and then gradually decreases as the thrombus resolves and IVC blood flow is restored. The number and size of collateral vessels parallels the thrombus resolution process, with decreasing collateral presence at days 14 and 21. However, the presence of a thrombus permanently alters the vein wall, leading to increased vein wall intimal thickness and fibrosis [7]. Thus, restoration of flow attenuates collateral presence but does not eliminate it; at least 2 collateral vessels continued to be visible through day 21 in all mice.

Interestingly, the peak collateral cross-section following total IVC obstruction was more than double that of pre-surgical IVC cross-sectional area previously reported in male C57BL/6 mice of the same age (collaterals: 2.5±0.6 mm^2 vs. baseline IVC: 1.12±0.04 mm^2) [89]. Conversely, peak collateral cross-sectional area following partial IVC obstruction (0.8±0.3 mm^2) accounted for roughly 70% of baseline IVC cross-sectional area [89].

The tortuous path of collateral vessels combined with slower blood flow in veins typically makes visualization with non-contrast enhanced MRI challenging. MOTSA overcomes some of the challenges of MR angiography by enabling imaging of longer extents of blood vessels [126]. The stitching of overlapping slices results in venetian blind artifacts which are due to a combination of the Gaussian radiofrequency pulse profile, the motion of blood between excitation and echo, and vessel geometry that may be other than the cranial-caudal direction. However, our efforts to minimize these artifacts using a slab thickness of 6 mm with 50% overlap, optimizing TR and FA for CNR, and acquiring isometric voxels enabled us to resolve both small vessels and vessels following a tortuous path.

The deep collateral pathway was observed in 7/10 mice via enlargement of the ascending lumbar veins. However, the deep collateral pathway in mice reconnected to the IVC through a lumbar vein proximal to the thrombus in all cases rather than extending to the azygos and hemiazygos veins, a preferential collateral pathway in humans with superior vena cava obstruction [113]. C57BL/6 mice consistently have 2 lumbar veins draining into the IVC between the left renal vein (which sits lower than the right in mice) and iliac bifurcation. These lumbar veins are cauterized in the ligation model, but remain patent in the EIM. As such, the deep collateral pathway presents less flow resistance in the EIM compared to the ligation model, which supports the observed persistence of this pathway over time in the EIM.

Interestingly, the deep collateral pathway was present in all mice with at least one lateral branch, whereas only 1 of 4 mice with no lateral branches exhibited deep collaterals. Likewise, mice with no lateral branches displayed less prominent superficial collaterals. In the anatomical variation with no lateral branches, the right gonadal vein connects with the IVC at or proximal to the left renal vein, while the left gonadal vein connects with the left renal vein. The gonadal veins are the largest pre-existing vessels of the collateral pathways, making venogenesis via the intermediate pathway the most prevalent when the anatomical variant did not necessitate their interruption during thrombus induction. Conversely, mice with bilateral branches (both gonadal veins draining into the IVC between the left renal vein and iliac bifurcation) displayed the most prominent superficial collaterals, persisting through day 21 in the ligation model and day 14 in EIM (Figure 5.2A-B, green arrowheads). As expected, the portal collateral pathway was not observed in these models because the thrombus in both the ligation model and EIM do not extend beyond the renal veins, thus the portal vein was not obstructed. The phenotype of a possible portal collateral pathway in mice remains to be investigated.

Female mice were not used in this study due to an anatomical challenge in C57BL/6 females; ligation of the right uterine vein, necessary for both models as it drains into the infrarenal IVC, leads to necrosis of the reproductive organs [61]. Thus, we would not be able to humanely study chronic time points in female C57BL/6 mice. This limitation may be overcome through the use of mice from the BALBc background, which often do not have lateral IVC branches but rather increased lumbar branches. Differences in collateral patterns between mouse strains and the presence and relevance of BALBc collateral pathways to humans remains to be investigated.

In conclusion, three-dimensional renderings of MOTSA data enabled tracking of small tortuous veins, and revealed that collateral pattern is influenced by pre-existing anatomy. These data support that murine models are relevant tools to study venogenesis, and support the use of MOTSA as a tool of choice with which to study this process. Importantly, we have shown that the collateral pathways in mice are consistent with those described in humans. Additionally, similar to humans, collateralization in mice correlates with the degree of obstruction. This work represents the first characterization of the collateral pattern following IVC obstruction in mice, which is critical for understanding the pathophysiology in preclinical modeling. This mapping may be helpful for researchers to make observations of potential therapeutic effects in mouse models.

Chapter 6

Thrombus Composition by Multiparametric MRI

6.1 Introduction

Clinical response to current DVT therapies has large variability due to variation in the composition and age of a thrombus. The use of MRI has mainly been limited to diagnosis when ultrasound or contrast venography is contraindicated, however, the vast information readily attainable by MRI can go beyond diagnosis to provide patient specific information regarding thrombus composition, which could be used to model and eventually predict susceptibility to different types of treatments.

The potential of MRI as an interventional tool for DVT is just beginning to be realized. One hospital in the Netherlands recently developed their own qualitative classification of thrombus age based on gadolinium-enhanced MR venography (MRV) [129]. Their preliminary data showed that thrombi they defined as acute by MRV lysed within just over 24 hours by CDT, sub-acute thrombi lysed in just under 48 hours, and chronic thrombi showed little or no lysis after 3 days [21]. While promising, their qualitative classification is highly subjective; to be used as an interventional tool, quantitative metrics are needed.

Another group applied multiparametric MRI to post mortem human thrombi samples imaged *ex vivo* to compare acute VT to acute/chronic PE and sedimented clots (formed post mortem) using T2 and apparent diffusion coefficient (ADC) values. They showed distinct ADC-T2 2D distributions between the different groups of thrombi, demonstrating the potential of MP-MRI to assess thrombus structure [130]. However, this study had major limitations such as long scan time (>5 hours), lack of heterogeneity consideration, and they did not show feasibility for the *in vivo* setting where the thrombus is surrounded by blood flow, inflammation, and extravascular structures. Further, another study showed similar ADC values in RBC-rich thrombi and collagen-rich thrombi [131], which would therefore only enable distinction of subacute thrombi and not be clinically informative.

Saha et al showed that a short T1 is associated with fibrin in the St. Thomas stenosis murine VT model, and thrombi with the shortest T1 had the greatest percentage of lysis following t-PA administration, as measured by phase contrast MRI [131]. However, similar to ADC, the transient nature T1 attenuation limits its potential as a single metric for thrombus aging. Perhaps the most promising metric tested to date is magnetization transfer rate, which is shown to increase with increasing fibrin and collagen content [64]. When used in combination with ADC, which peaks at day 14, Phinikaridou et al showed a sensitivity of 87.5% and a specificity of 83.3% at identifying intermediately aged murine thrombi (days 7 and 14).

These methods share a common limitation – they treat the entire thrombus as a homogenous entity with one single identifiable disease stage. On the contrary, thrombi are known to be highly heterogenous both spatially within a given patient and longitudinally between patients. Multiparametric MRI, commonly used in tumor imaging [132], [133], offers the possibility of identifying heterogeneities that are not fully discernible in single-parametric assessments.

6.2 Study Design

6.2.1 Mouse Models

DVT was induced in male C57BL6 mice aged 10-12 weeks by either total IVC ligation (n=15), or by the EIM (n=15). Each model group was divided into 3 time points of interest: day

2, 6, or 14, n=5 each. Mice were imaged at 7T on days 2, 6, or 14 using TOF imaging and multiparametric MRI (MP-MRI). TOF imaging enabled distinction of a clear boundary between thrombus (filling defect—hypo-intense) and flowing blood (hyper-intense) during thrombus recanalization. Mice were sacrificed and thrombi were harvested for histology immediately following imaging. Thrombi were harvested with surrounding tissue to maintain anatomical landmarks, and fixed sections were cut into proximal, middle, and distal slices for pairing with MRI (Figure 6.1).

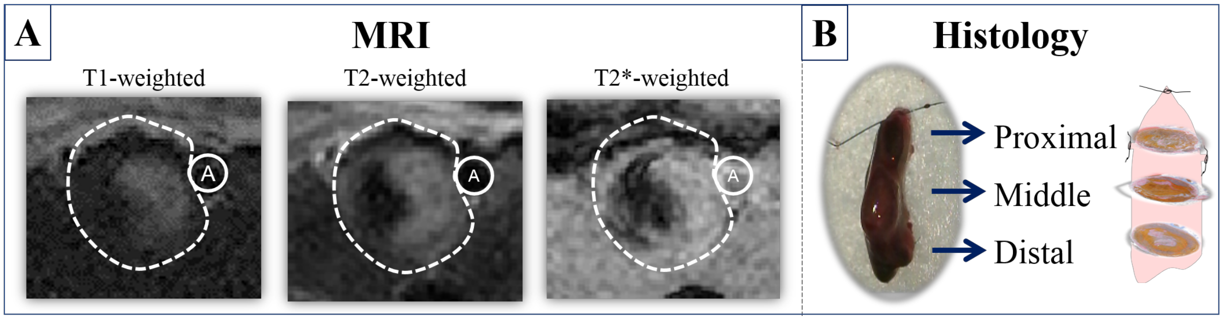

Figure 6.1 A: Representative MR images of the same location. Dotted white line – thrombus; solid line – aorta (A). B: Following imaging, mice were harvested, the thrombus was fixed, and 5 µm sections from 3 blocks were used for histology.

6.2.2 Multiparametric MRI Methods

T2*-, T2-, and T1-weighted acquisitions enable the distinction of spatial heterogeneities across a thrombus. We decided to use T1-, T2-, and T2*-weighted imaging for three reasons. First, these scans are readily translatable to the clinic. Second, contrast agents cannot be used in patients with chronic kidney disease, which is becoming more prevalent with the rise of diabetes and hypertension, so by not relying on contrast agents we ensure that this method can be used in all patients. Third, weighted scans are much faster than proper mapping.

All MP-MRI acquisitions were acquired with a FOV of 30^2, a matrix of 256^2 zero-filled to 512^2, and 1 mm slice thickness. We used a fast spin echo for the T2-weighted acquisition that is sensitive to fluid such as edema and unorganized thrombus ($TR/TE_{effective}$ 1500/20ms, echo spacing 10ms, echo train length 2, NEX 3, ~10min). For T2*-weighting we used gradient echo with a short TE that's sensitive to structured material and blood products (TR/TE: 200/6 ms, FA 20º, NEX 4, 3 min 25 sec). For T1-weighting we used a fast spin echo with a short TR that is sensitive to trapped proteins such as platelet aggregates which appear bright on T1-weighted imaging (TR/$TE_{effective}$ 200/12 ms, NEX 8, 6 min 50 sec). Red blood cell rich regions also appear bright on T1-weighting, but this signal is lost as the red blood cells die and release iron.

We expected fibrin to appear dark on T2- and T2*-weighted scans due to its highly structured nature. As the thrombus remodels to a collagen-rich scar, platelets and RBCs are cleared and we expected remaining thrombotic regions to appear dark on T2-, T2*-, and T1-weighted scans. Platelets form tight aggregates mimicking solid tissue structure, with an accumulation of cellular proteins released by the activated platelets and trapped in the platelet plug. The trapped proteins shorten the spin-lattice relaxation times causing platelet aggregates to appear bright on T1-weighted scans [134]–[136]. RBC-rich regions also demonstrate T1 shortening due to the accumulation of paramagnetic Fe^{3+}, however the lack of extracellular serum in platelet aggregates outweighs the spin-lattice relaxation for clots with hematocrit levels up to 60% [135]. As such, there may be differences in signal intensity for RBC-rich regions depending on the model used (stasis model compared to EIM blood flow model) as well as the organization of the thrombus over time. In high enough concentrations, we expected iron from RBCs to result in loss of signal in T2*-weighted images.

6.2.3 Histology

Excised thrombi with surrounding tissue were formalin fixed overnight, dehydrated in alcohol, paraffin embedded, and cut into 5 µm longitudinal sections. Sections were stained for gross anatomy (Hematoxylin & Eosin), collagen (Masson's Trichrome), and fibrin/red blood cell content (Martius Scarlet Blue – MSB). Stained sections were photographed via light microscopy

(Nikon, Tokyo, Japan) under 40x magnification. Regions of interest containing the thrombus and vein wall were manually traced in ImageJ (NIH) and quantification of each component was assessed through color threshold values as previously described [101].

6.3 Analysis Methods & Preliminary Findings

6.3.1 Manual Thresholding of MP-MRI

First, thresholding techniques were used to assess the individual MRI signals for similarities/differences across animals and between models (Figure 6.2), focusing on low T2* signal as an indicator of highly structured material and/or the potential entrapment of deoxygenating RBCs (average signal intensity in a region of dark thrombus + 2 standard deviations = maximum threshold) and high T2 signal as an indicator of fluid related to edema (average signal intensity in a region of bright thrombus + 2 standard deviations = minimum threshold).

Thrombus composition varied spatially and temporally. Low T2* signal, indicating structured material such as a fibrin mesh or deoxygenating RBCs, was most prevalent at day 2 in both models (Figure 6.2 left). Interestingly, thrombi developed under stasis conditions saw a sharp decrease in regions of low signal intensity in T2* at days 7 and 14 (Figure 6.2A left), whereas thrombi developed under flow saw a more gradual decrease in the amount of low T2* signal intensity regions with time (Figure 6.2B left). Thrombi from the blood flow model showed low intensity T2* regions through day 14, centered on the site where current was applied to activate the endothelium. This suggests that totally occlusive thrombi may begin to remodel more quickly compared to thrombi in the presence of blood flow, via deposition of disorganized collagen eventually forming a collagen-rich scar. Regions with high T2 signal were more prevalent in the stasis model across time points (Figure 6.2 right), indicating an increased inflammatory response in occlusive thrombi.

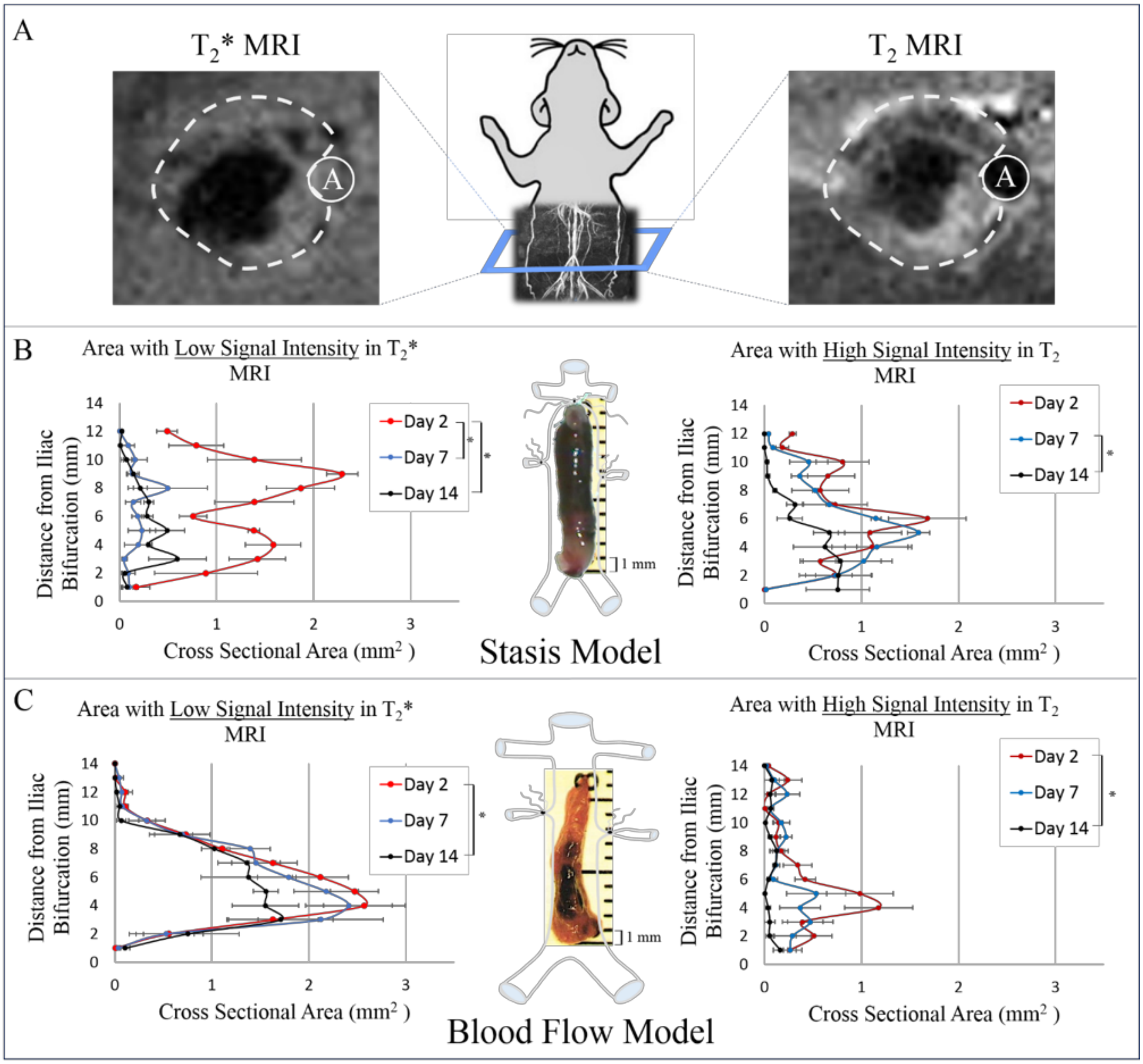

Figure 6.2 A: Contiguous axial slices were acquired using T_2* and T_2 MRI. Thrombi (dashed line), shown adjacent to the aorta ('A', solid line) displayed heterogeneity in signal intensity. B & C: Representative gross anatomy images for each model are shown in the center. For each axial slice along the thrombus, the area of low signal intensity in T_2* MRI (left) and high signal intensity in T_2 MRI (right) was measured by thresholding techniques for both the stasis model (B) and the blood flow model (C). Time points were compared using two-way ANOVA, * $p<0.05$.

6.3.2 Unsupervised Classification

Rather than assessing each MP-MRI acquisition separately, more information can be gained from combining the signals to form a tissue composition map informed by the signal signature from each MP-MRI scan. Thus, we implemented unsupervised classification techniques to assign each voxel a classification based on its signal signature from the T1-, T2-, and T2*-weighted acquisitions. Thrombi were manually traced with a paired TOF scan to aid in defining the boundary between the thrombus and blood flow. Signal intensities from each scan were normalized to a mean of 0 and a standard deviation of 1 to enable comparison between signals. Normalizing the entire MRI signals from each scan to a uniform mean and standard deviation is more objective and consistent than the commonly used method of normalizing to an internal reference tissue. A reference tissue, typically back musculature, introduces some level of subjectivity based on the size and location of the region chosen for normalization. This would also become a time-consuming process with 11 slices x 3 images = 33 regions of interest for normalization to be defined per mouse. Additionally, the signal intensities in the three scans are vastly different from one another, thus there is a benefit to also normalizing the signal intensities to standard deviation of 1, which would not be achieved by normalizing to a reference tissue.

K Means Clustering

Initially, a k-means clustering algorithm was used to classify voxels within the thrombus into three populations based on the T2 and T2* MP-MRI. Tissue classification by k-means clustering further supported that blood flow conditions affect thrombus composition (Figure 6.3). The drawback of k-means clustering is that it gives a hard assignment, and updates the classification assignment using only the points in the same class with an equal distribution of data points in each cluster. Therefore, we decided to move to a different unsupervised classification algorithm.

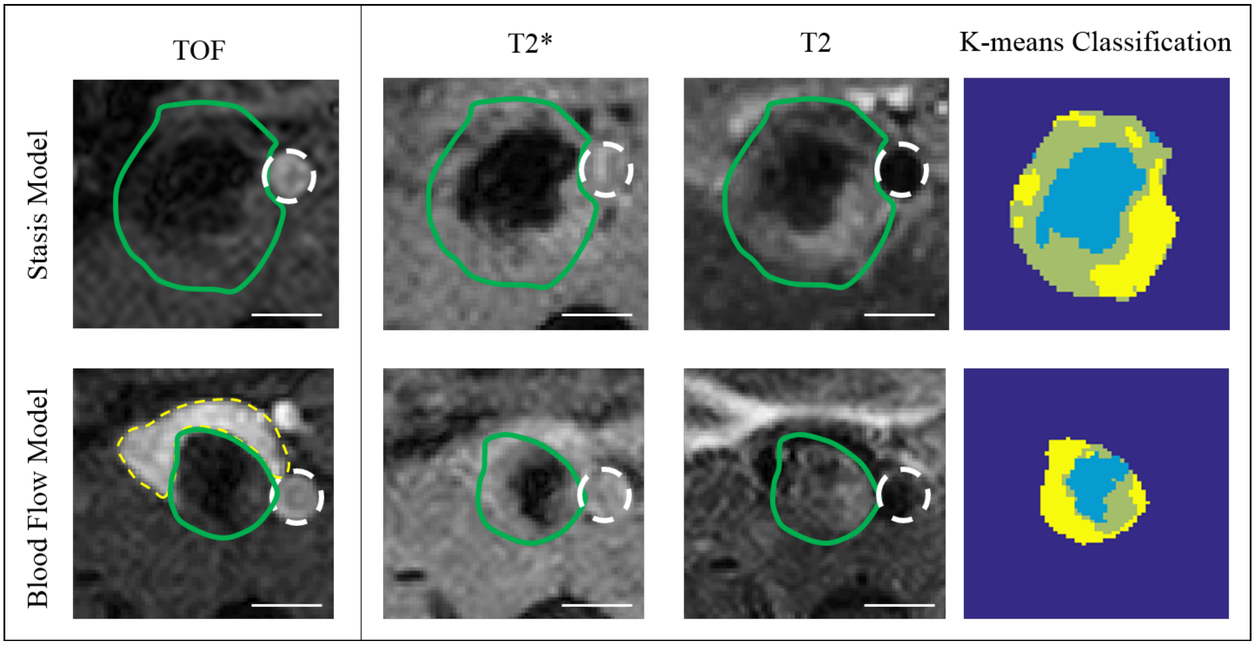

Figure 6.3 Representative T2* and T2 MR images (windowed and leveled individually) used for classification in two murine models of venous thrombosis at day 2 post induction. Thrombus – green, aorta – white dashed line, scale bar 1 mm.

Gaussian Mixture Model

We chose a Gaussian Mixture Model (GMM) because it uses soft classifications and updates the classification using all points in the population, which helps express uncertainty. The GMM fits a finite number of Gaussian distributions to a set of data, where the outcome is not known a priori. In our case, the objective was to fit the model to the MRI intensities to identify underlying features and determine whether such features correlated to known composition by histology. An expectation-maximization statistical algorithm is used to maximize the likelihood that each intensity pair belongs to one of a user-defined number of total clusters.

We used the Akaike information criterion, or AIC, to determine the appropriate number of clusters to use. The AIC is an estimate of the relative quality of a statistical model given the data, with a lower the score indicating a better fit. Figure 6.4 shows the AIC score for a given number of clusters. There is a clear elbow point at 3 clusters, beyond which there is not much improvement in the model thus risk of overfitting the data. Thus, we chose to use 3 clusters for probabilistic tissue classification.

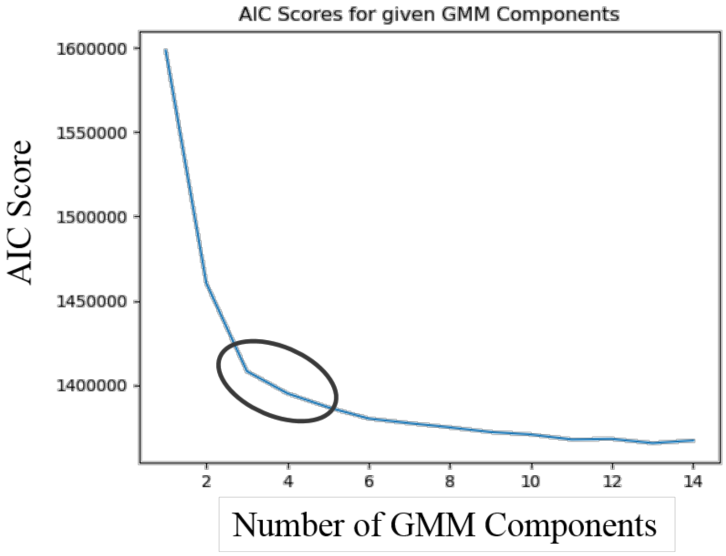

Figure 6.4 Akaike information criterion (AIC) parameter search scores for the first 15 clusters to reduce the relative information lost in the Gaussian mixture model. The circle indicates good options for minimizing AIC without overfitting the model.

The GMM was applied to n=5 mice per 3 time points (day 2, 6, or 14) in 2 models (ligation or EIM), with roughly 11 axial slices through each thrombus for a total of 330 data sets. Following GMM classification, a color was assigned for each tissue class and a classified tissue map was generated for each slice (Figure 6.5). Stacking the 2D slices in a 3D representation of the thrombus emphasize the spatial heterogeneity along the thrombus. Proximal, middle, and distal histological sections were manually paired with their approximately corresponding MRI slice. It is important to note that the histology is 5 μm thick, whereas each MRI slice is 1 mm thick (200x thicker). Hence, the MRI represents an average of what is going on in the general region of each histological slice. Despite this limitation, qualitative comparison shows promising co-localization. MRI from each time point with the corresponding martius scarlet blue (MSB) staining is shown in Figure 6.6.

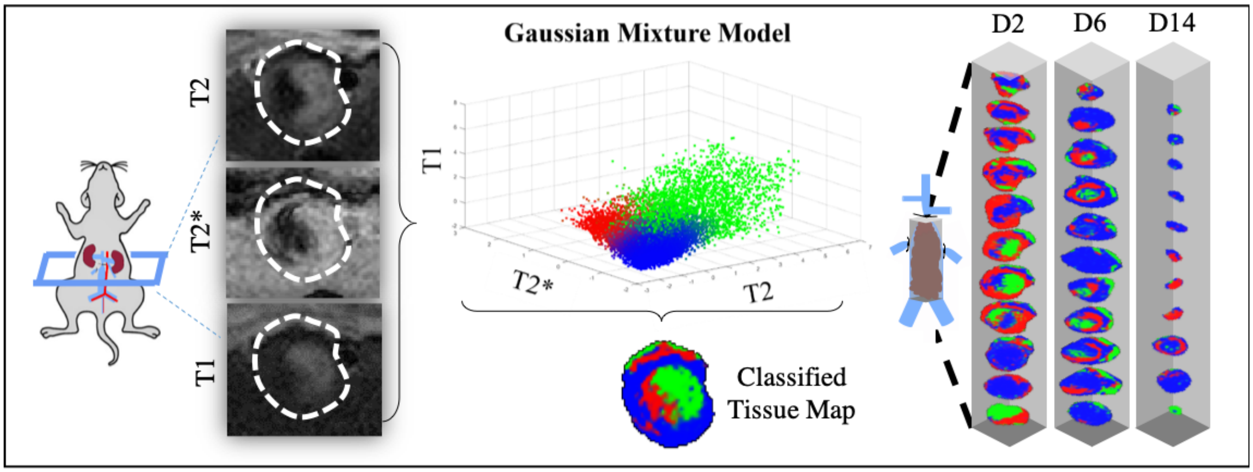

Figure 6.5 Schematic representation of GMM workflow. Voxels are classified using a GMM and mapped back to the thrombus to form a classified tissue map for each axial slice. 3D stacks of 2D images for the ligation model at days 2, 6, and 14 are shown at the right.

6.4 Results

The MP-MRI revealed clear differences between the ligation and EIM models. This is consistent with *ex vivo* findings that thrombus composition is dependent on the blood flow conditions under which it has formed and resolved. Total stasis resulted in a bulls-eye pattern that resolved radially inward, whereas partial occlusion resulted in a binary distribution between the site of origin and the (slightly younger) tail of the thrombus. The proximal (tail) end of the EIM thrombi more closely resembled the ligation thrombi.

We observed that the blue tissue class was more prevalent at chronic time points, the red tissue class was most prevalent at day 2, and the green tissue class decreased over time. Based on this hypothesis, we hypothesized that the blue tissue class may correspond to organized thrombus (characterized by collagen content, blue on MSB), red to RBCs (yellow on MSB), and green to fibrin (pink on MSB).

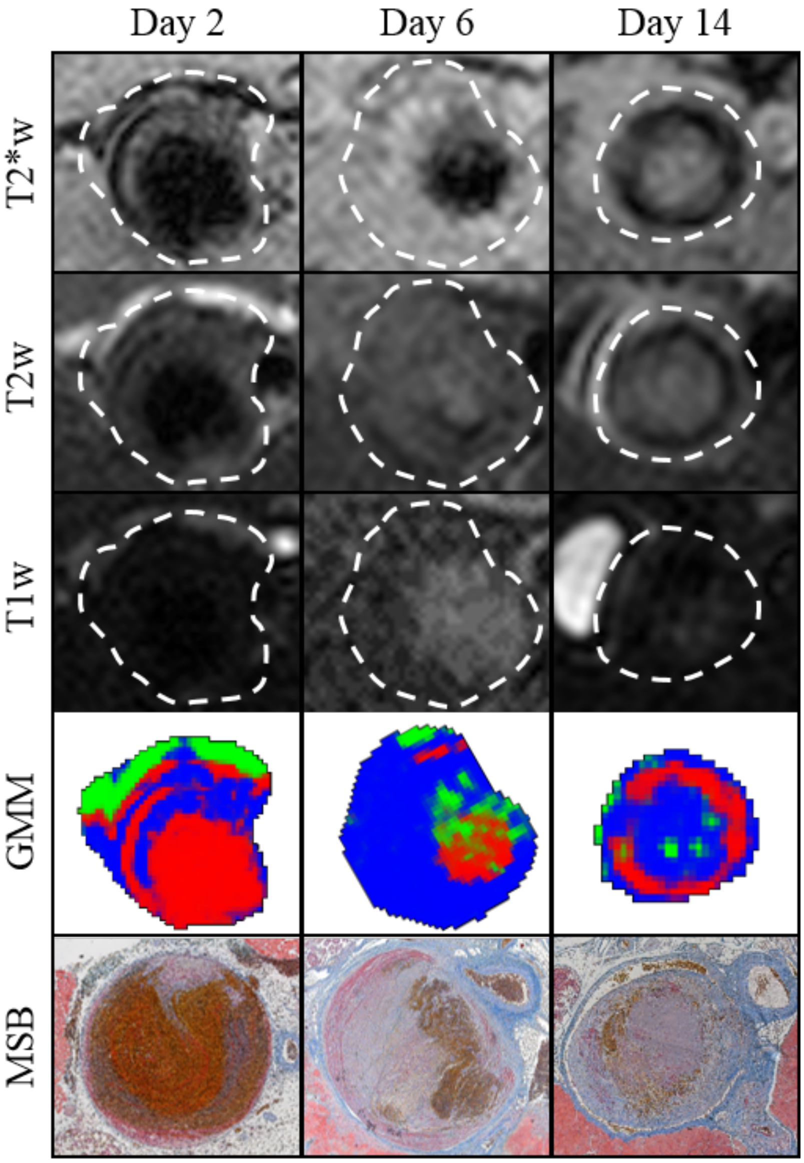

Figure 6.6 Representative MP-MRI and resulting GMM with paired MSB histology for each time point.

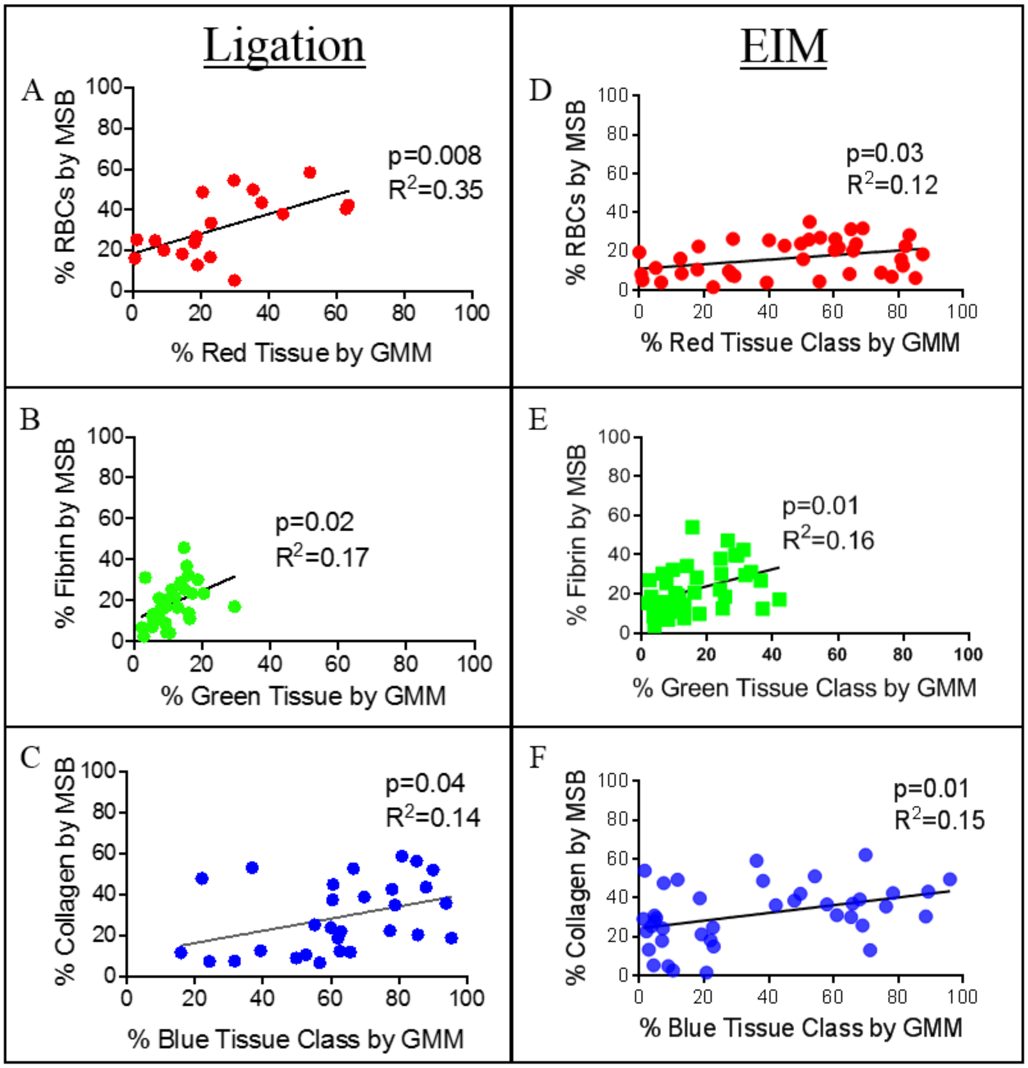

Figure 6.7 Ligation and EIM correlation of GMM with histological staining for RBCs (A, D), fibrin (B, E) and collagen (C, F).

Based on these hypotheses, we assessed the correlation between %GMM tissue class with the corresponding composition as a % positive MSB staining across the thrombus and vein wall across time points. Although this correlation ignores spatial localization, we found a significant correlation in every case. The red tissue class correlated with thrombus rich in RBCs, shown as yellow in MSB histology (Ligation: $R^2=0.35$, $p<0.01$, Figure 6.7A; EIM: $R^2=0.12$, $p<0.03$, Figure 6.7D), while green correlated with fibrin, shown as red in MSB (Ligation: $R^2=0.17$, $p<0.05$, Figure 6.7B; EIM: $R^2=0.16$, $p<0.01$, Figure 6.7E). The blue tissue class, characterized by

MR signals indicating structured material, correlated with collagen content (blue in MSB, Ligation: $R^2=0.14$, $p<0.05$, Figure 6.7C; EIM: $R^2=0.15$, $p<0.01$, Figure 6.7F).

6.5 Conclusions

The MP-MRI framework provides a novel approach to non-invasively determine thrombus composition with readily available imaging techniques. This methodology does not require contrast agents or long scan times. Classification of the data showed thrombus organization and evolution, validated by correlation with histology. This approach provides foundational methodology that could eventually be used clinically to provide patient-specific treatment planning for DVT, which would improve patient quality of life and reduce the risk of adverse events from treatment, including death. An example the application of this methodology to treatment planning is shown in Figure 6.8.

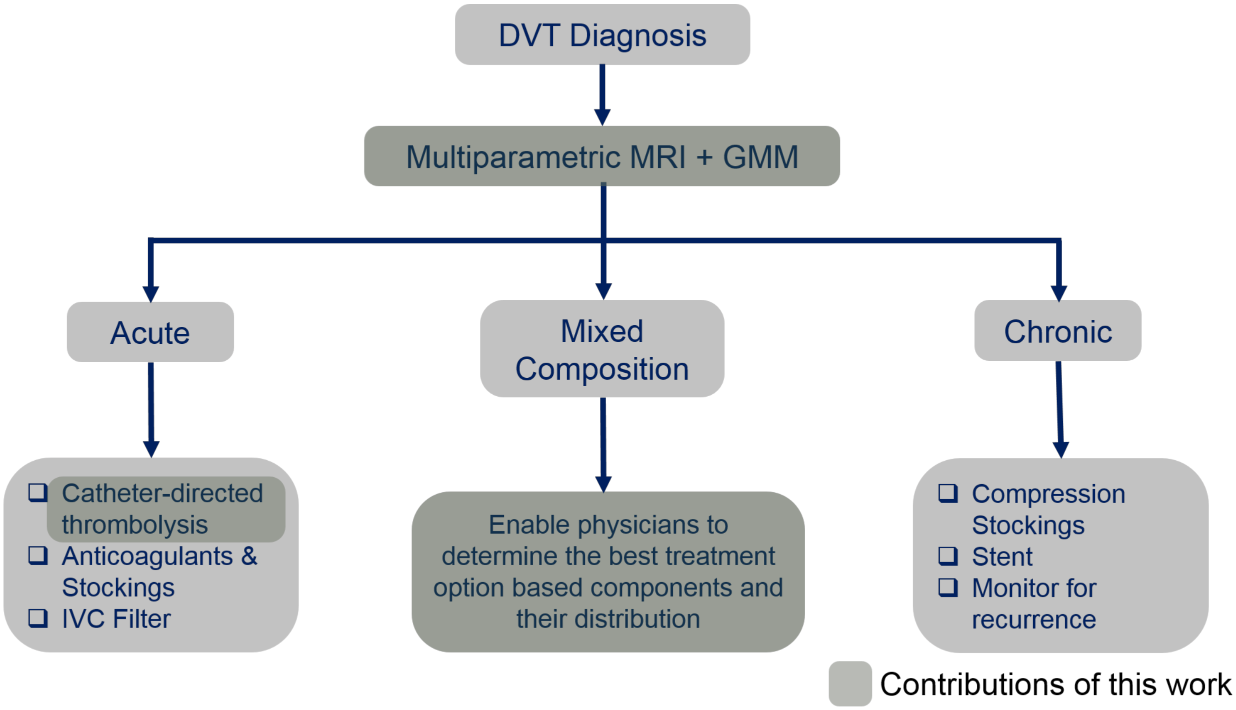

Figure 6.8 Schematic of treatment options. Currently, the thrombus age is inferred from the patient's recollection of symptom onset. Treatment selection based on thrombus composition would reduce the risk to the patient.

Chapter 7

Effects of Spontaneous Exercise on Murine Model of Venous Thrombosis

7.1 Introduction

Exercise has tremendous cardiovascular health benefits that have been indicated to be safe and beneficial in patients with DVT, yet we lack an understanding of *how* exercise affects thrombus formation and resolution. Exercise and ambulation in patients with DVT have been controversial given the historical but never empirically tested narrative that ambulation could cause PE. This narrative has since been discredited [137]–[140]. Several recent studies suggest that early walking does not increase the risk of PE, may reduce the risk of extensions of proximal DVT shortly after diagnosis, and may be associated with less severe post thrombotic syndrome [141]–[144]. Given the significant bleeding risks associated with the standard treatment of anticoagulation and large variation in response to treatment, understanding the impact exercise may play on DVT could open a new avenue of treatment and/or inform treatment practice in the case of an athlete or highly active person with DVT.

In humans, it is well established that the effects of exercise are dependent on duration and intensity. Regular moderate exercise is associated with beneficial health effects, whereas strenuous prolonged exercise such as in endurance athletes can induce negative physiological disturbances. In rodents, studies using forced exercise (treadmill with a motivator such as electric shock) have been shown to cause significant stress that may outweigh the benefits of exercise. These effects were emphasized in studies of the gastrointestinal microbiome, which showed increased inflammatory gene expression, increased morbidity (diarrhea) and increased mortality in mice undergoing forced exercise, while the opposite effect was observed in mice undergoing voluntary running wheel exercise [145], [146]. Inflammation plays a key role in VTE, thus stress induced exercise could exacerbate the inflammatory response and misrepresent the effects of exercise in humans. Therefore, we chose to use spontaneous exercise in the form of in-cage running wheels to investigate whether exercise, alone and in combination with standard treatment, impacts thrombus composition and resolution.

7.2 Methods

All experiments were performed with approval of the University of Michigan's Institutaional Animal Care and Use Committee.

7.2.1 Experimental Groups and Spontaneous Exercise

10-12-week old C57BL6 male mice divided into four groups outlined in (Figure 7.1): true controls (**CC**) were not given access to an in-cage running wheel and received no pharmacological intervention, exercise controls (**EC**) were given access to in-cage running wheels starting 2 weeks prior to and continuously following VT induction but received no pharmacological intervention, the non-running heparin group (**CH**) received 6mg/kg low molecular weight heparin twice daily via subcutaneous injection beginning 4 hours after VT induction but had no access to a running wheel, and the exercising heparin experimental group (**EH**) received the same LMWH treatment with running wheel access beginning 2 weeks prior to and continuously following VT induction. Mice exposed to a running wheel were singly housed to enable individual monitoring of exercise activity. A 2-week acclimation period prior to VT induction was chosen because this time period has been demonstrated to induce vascular conditioning in wheel-running mice [147]. Because we hypothesized that exercise would lead to a reduction in thrombus size (leading to non-occlusive thrombi in humans) and a reduction in circulating inflammatory cytokines, we chose to use the EIM model to enable continuous blood flow access to the thrombus.

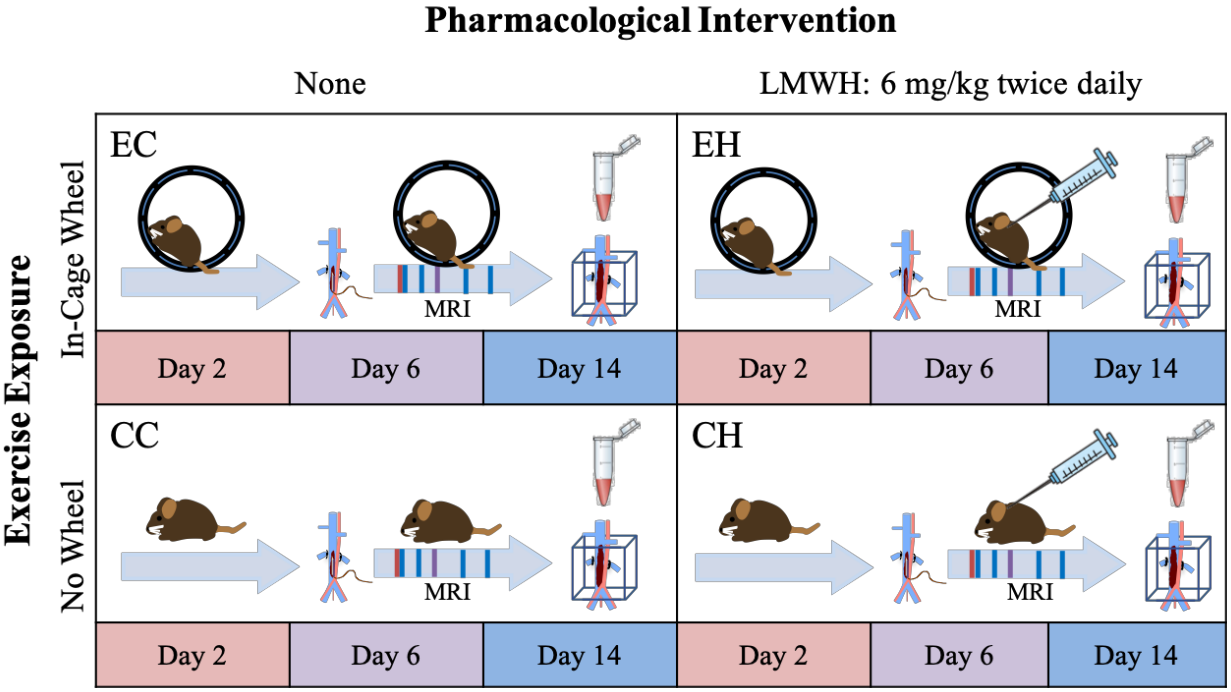

Figure 7.1 Schematic representation of experimental groups. Exercising mice (EC and EH) had continuous access to an in-cage running wheel beginning 2 weeks prior to and continuously following VT induction by EIM. Mice with pharmacological intervention (EH and CH) received subcutaneous injections of low molecular weight heparin (LMWH). Within each experimental group, mice were separated into three time points of interest (day 2, 6, and 14 following VT induction, n=5 each). Day 2 and 6 mice were imaged on days 2 and 6, respectively, prior to harvest. Day 14 mice were imaged at days 2, 4, 6, 11, and 14 prior to harvest. At harvest, blood was collected via exsanguination, and the IVC with surrounding tissue was collected for histology.

7.2.2 Magnetic Resonance Imaging

Within each of the four experimental groups, mice were separated into three time points of interest representing the harvest time point: day 2 (acute), 6 (sub-chronic), or 14 (chronic) following VT induction, n=5 per time point within each group. Day 2 and 6 mice were imaged on days 2 and 6, respectively, prior to harvest. For longitudinal data on thrombus resolution in the same mice over time, day 14 mice were imaged at days 2, 4, 6, 11, and 14, followed by harvest at day 14. 2D contiguous axial TOF images and MP-MRI was acquired as described in Chapter 6.2.2.

7.2.3 Histology and Immunohistochemistry

The IVC containing thrombus was harvested with surrounding tissue to maintain anatomic landmarks for orienting with image data. Samples were formalin fixed overnight, dehydrated in alcohol, paraffin embedded, and cut into 5 μm axial sections at three locations along the thrombus: proximal, middle, and distal. Sections were stained by using hematoxylin and eosin (H&E) for anatomic detail, Masson's Trichrome for collagen content, and Martius Scarlet Blue for RBC and fibrin content. Percent RBC, fibrin, and collagen content was analyzed by thresholding as in a modification of the previously described method [101].

For immunohistochemistry, non-specific sites were blocked with normal serum. Sections were incubated with primary antibodies to Ly6G (1:2000, BD Pharmingen, Catalog # 551458, Franklin Lakes, NJ), FSP-1 (1:2000, Millipore, Catalog # 07-2274, Burlington, MA), CD68 (1:100, Bio-Rad, Catalog # MCA1957, Hercules, CA), or CD41 (1:100, Santa Cruz, Catalog # Sc-6602, Dallas, TX). A species-specific ABC peroxidase kit (Vector Laboratories Inc., Burlingame, CA) was used according to the manufacturer's instructions for the corresponding secondary antibody and subsequent steps. Color development was performed with diaminobenzidine (DAB). Images were captured using light microscopy (Nikon, Tokyo, Japan) under 40x magnification and quantification of percent positive staining was performed as previously described [101].

7.2.4 Circulating Inflammatory Cytokines

At harvest, blood was collected via exsanguination by cardiac puncture and incubated undisturbed at room temperature for at least 20 minutes. Samples were then centrifuged at 4 °C for 10 min at 3000 rpm, and blood serum was extracted and stored at -80 °C. Standard enzyme-linked immunosorbent assays (ELISAs) for IL-6 (from Abcam, Cambridge, MA), IL-1β, TNFα, and CRP (from R&D Systems, San Diego, CA) were used to measure blood serum levels of each circulating inflammatory cytokine according to manufacturer's instructions.

7.3 Results

7.3.1 Exercise Reduces Thrombus Size

Of the 37 mice exposed to an in cage running wheel, 6 did not engage in any spontaneous exercise activity. These mice were assigned to non-exercise groups. Mice that did use the in-cage running wheel averaged just under 1 km of running per day in the 2 weeks before VT induction, and 300 m per day following VT induction (Figure 7.2). We were initially unsure whether mice would run at all following surgery, so although they had reduced activity, these results show promise for the use of spontaneous exercise as a therapeutic following VT induction.

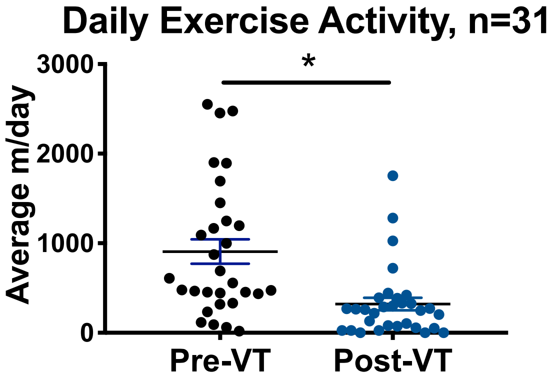

Figure 7.2 Average daily exercise activity in 31 mice before and following VT induction.

Exercise reduced thrombus size at initiation and throughout thrombus resolution (Figure 7.3). As expected, thrombus volume was significantly reduced compared in mice treated with LMWH (CH and EH) compared to those receiving no pharmacological intervention (CC and EC) across time points. Interestingly, there was a trend of decreased thrombus volume across time points with exercise compared to the non-exercising control group. Exercise significantly reduced thrombus volume at day 11 compared to non-running controls (EC vs CC, $p<0.05$).

Further, from day 6 onwards, thrombus volume in EC mice were not significantly different from the CH group, indicating that by chronic time points, exercise approaches the effectiveness of LMWH at reducing thrombus volume. EH mice had a smaller thrombus volume compared to CH mice across time points, although these groups were not significantly different from one another.

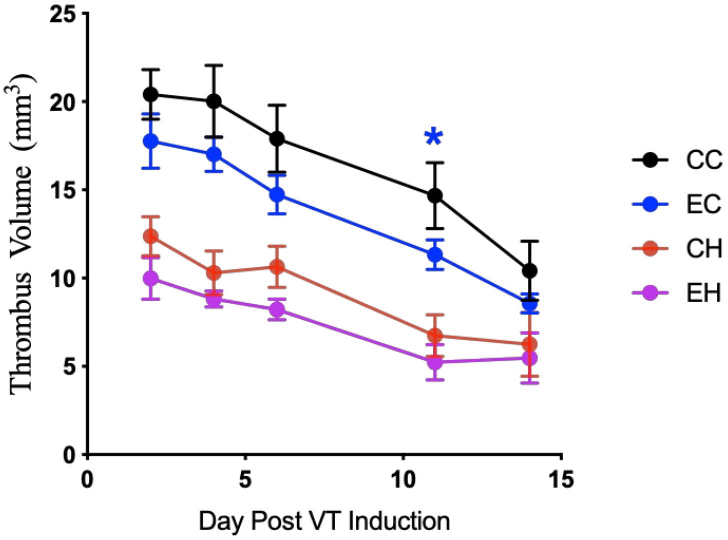

Figure 7.3 Thrombus volume measured by MRI. AT day 11, thrombus volume was significantly reduced with exercise, $p<0.05$. CC – true control; EC – exercise; CH – low molecular weight heparin (LMWH); EH – exercise + LMWH. Day 2, 11, and 14 have n=5 per group; days 2 and 6 have n=10 per group.

7.3.2 Impact of Exercise on Thrombus Composition

Neutrophils are the main leukocytes observed in acute VT, with a transition to monocytes in chronic VT. Neutrophils were observed in all groups at day 2. We found that exercise reduced neutrophil recruitment in acute VT in mice not receiving LMWH (Figure 7.4). Neutrophil content was not different in mice treated with LMWH (with and without exercise) compared to true controls.

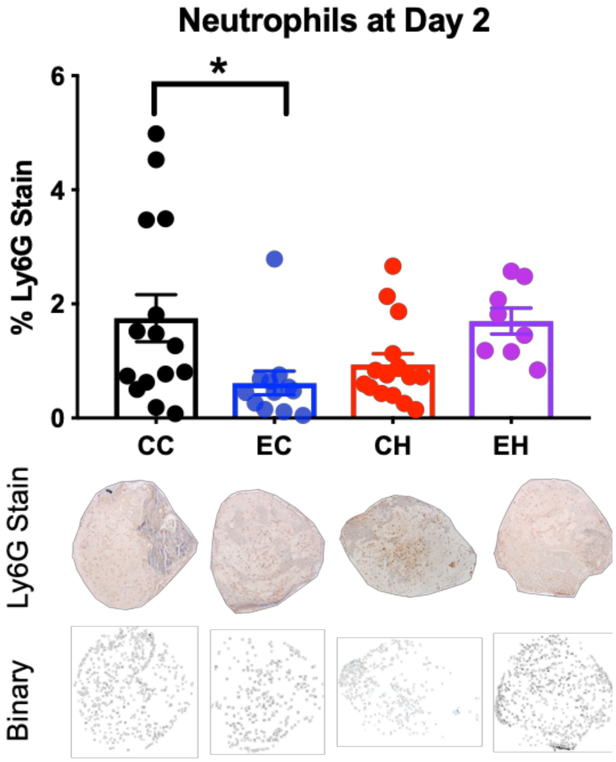

Figure 7.4 Neutrophil content as measured by Ly6g immunohistochemistry (IHC) with representative IHC and binary image of positive staining from each group. Binary images are enhanced for clarity – positive stain regions appear larger than the true amount. CC – true control; EC – exercise; CH – low molecular weight heparin (LMWH); EH – exercise + LMWH. * = $p<0.05$.

At day 2, the thrombus is largely composed of fibrin and entrapped RBCs. Exercise alone, but not coupled with anticoagulants, increased fibrin content in acute VT (Figure 7.5A). RBC content did not differ between groups (Figure 7.5B). At day 6, exercise tended to increase fibrin content in both treated and untreated groups, although this effect was not statistically significant (Figure 7.6A). LMWH alone decreased RBC content compared to CC and EC, but was not reduced in exercising LMWH treated mice (Figure 7.6B).

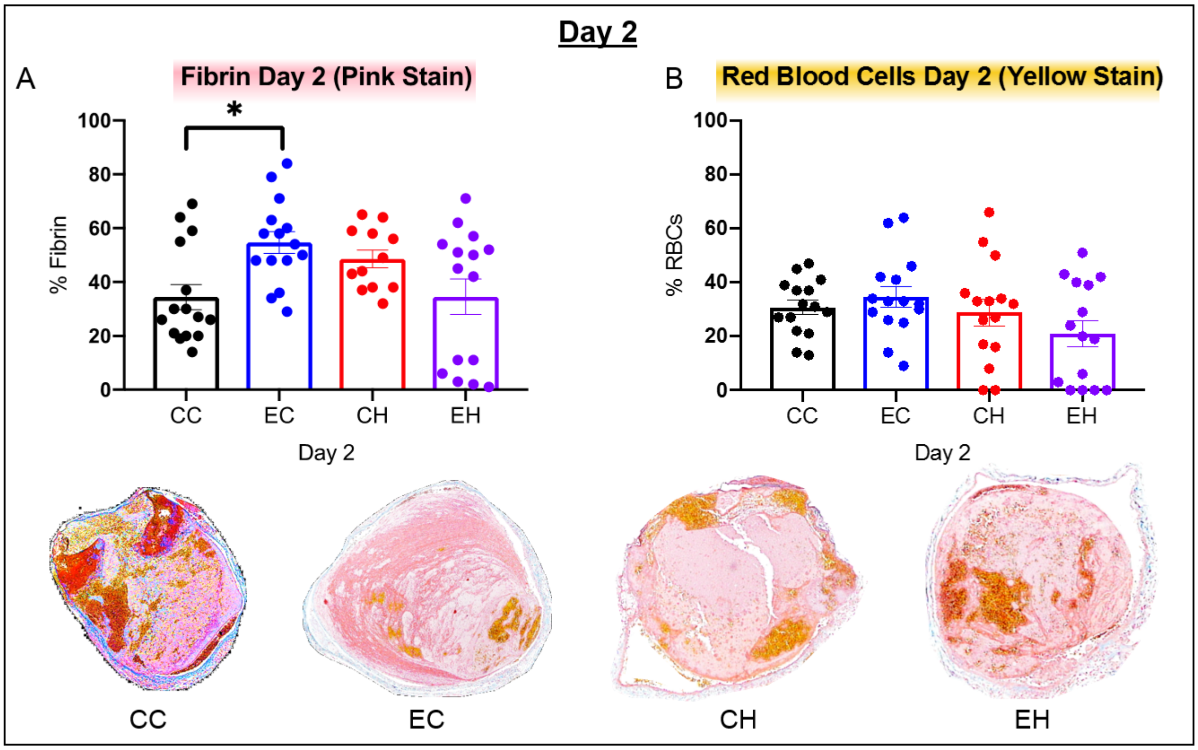

Figure 7.5 Day 2 percent fibrin (A) and red blood cell (B) content as measured from Martius Scarlet Blue stain and representative histology images from each group. Fibrin is stained pink, RBCs yellow, and collagen blue. CC – true control; EC – exercise; CH – low molecular weight heparin (LMWH); EH – exercise + LMWH. * = p<0.05.

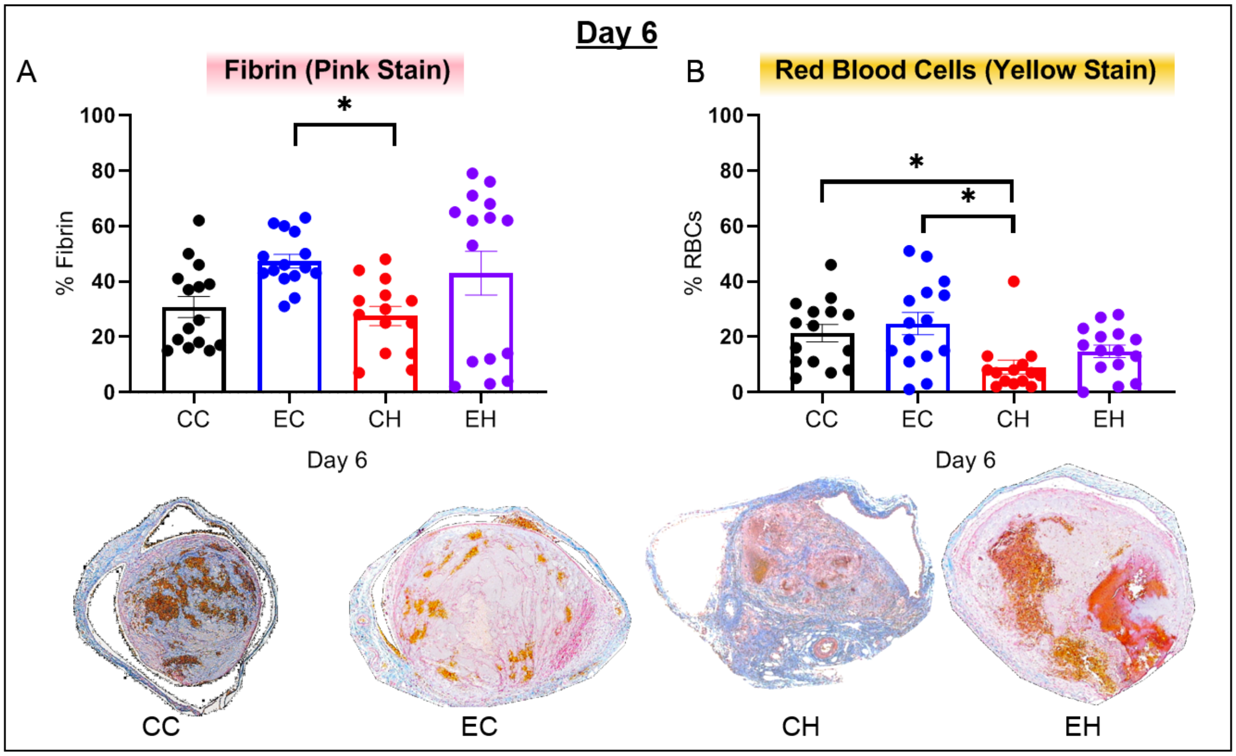

Figure 7.6 Day 6 percent fibrin (A) and red blood cell (B) content as measured from Martius Scarlet Blue stain and representative histology images from each group. Fibrin is stained pink, RBCs yellow, and collagen blue. CC – true control; EC – exercise; CH – low molecular weight heparin (LMWH); EH – exercise + LMWH. * = p<0.05.

In chronic VT, the thrombus organizes into a collagen rich thrombus that becomes incorporated into the vein wall. At day 6, collagen content in the vein wall and thrombus was greatest in non-exercising mice treated with LMWH (CH mice, Figure 7.7A-C). However, the opposite trend was observed in the thrombus at day 14 (Figure 7.7F), suggesting that LMWH hastens thrombus organization causing sub-chronic thrombi to resemble chronic thrombi. However, exercising mice receiving LMWH did not differ from true controls in collagen content at either time point. The groups did not differ in vein wall thickness, taken as the average of five measurements of the vein wall (data not shown).

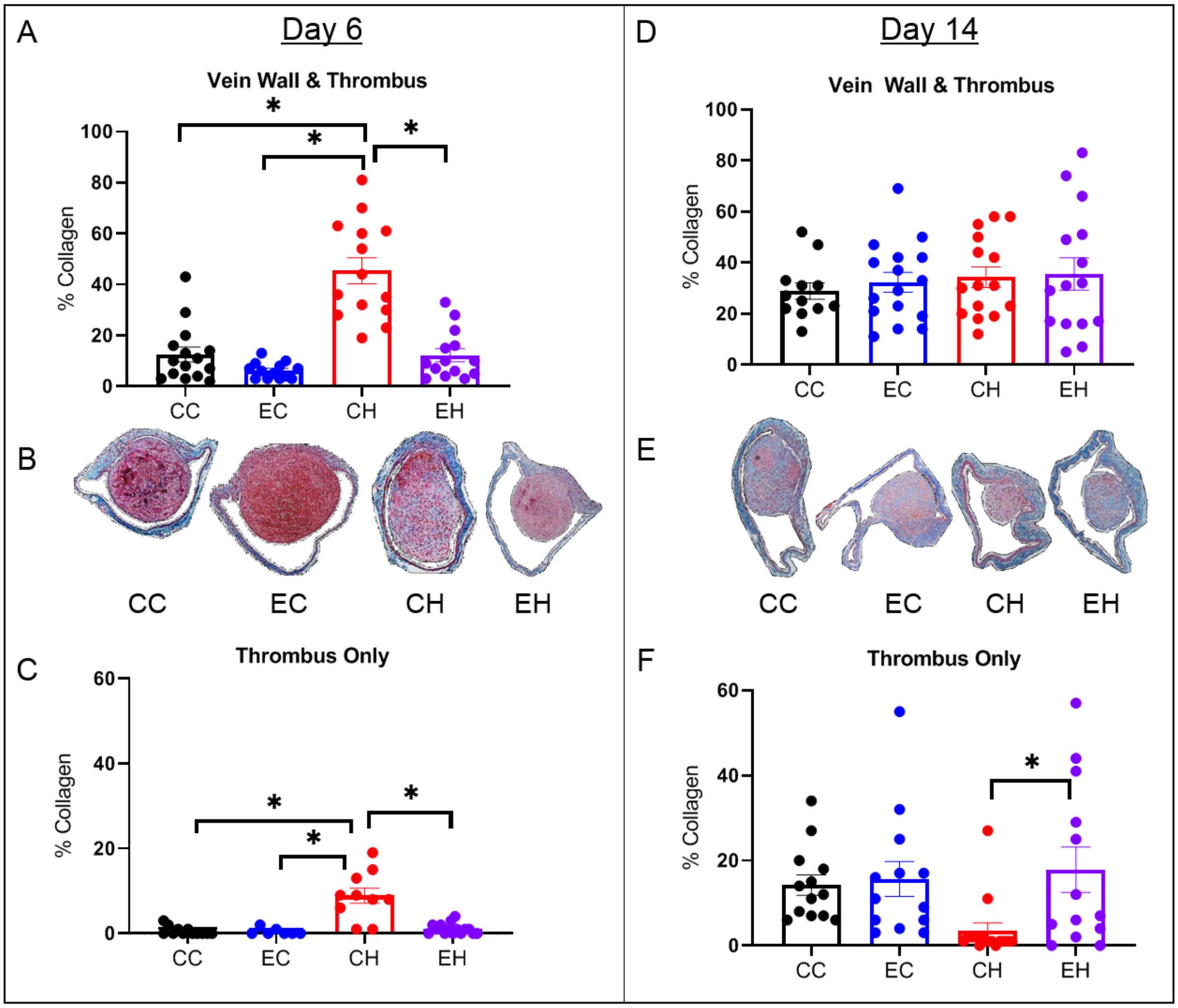

Figure 7.7 Percent collagen content in thrombus and vein wall (A, D) or thrombus only (C, F) with representative histology images from each group (B, E) at days 6 and 14 as measured from Masson's Trichrome stain (collagen = blue). CC – true control; EC – exercise; CH – low molecular weight heparin (LMWH); EH – exercise + LMWH. * = $p<0.05$, *** = $p<0.001$.

Fibroblasts are the precursor to collagen. We measured fibroblast content by fibroblast-specific protein-1 (FSP-1) IHC. At day 6, FSP-1 expression tended to decrease with exercise compared to the control group under the same treatment conditions, although this decrease was not significant (Figure 7.8A). At day 14, the opposite trend was observed, although again not significant (Figure 7.8B). LMWH decreased fibroblast expression in both CH and EH groups compared to EC, but not compared to CC mice.

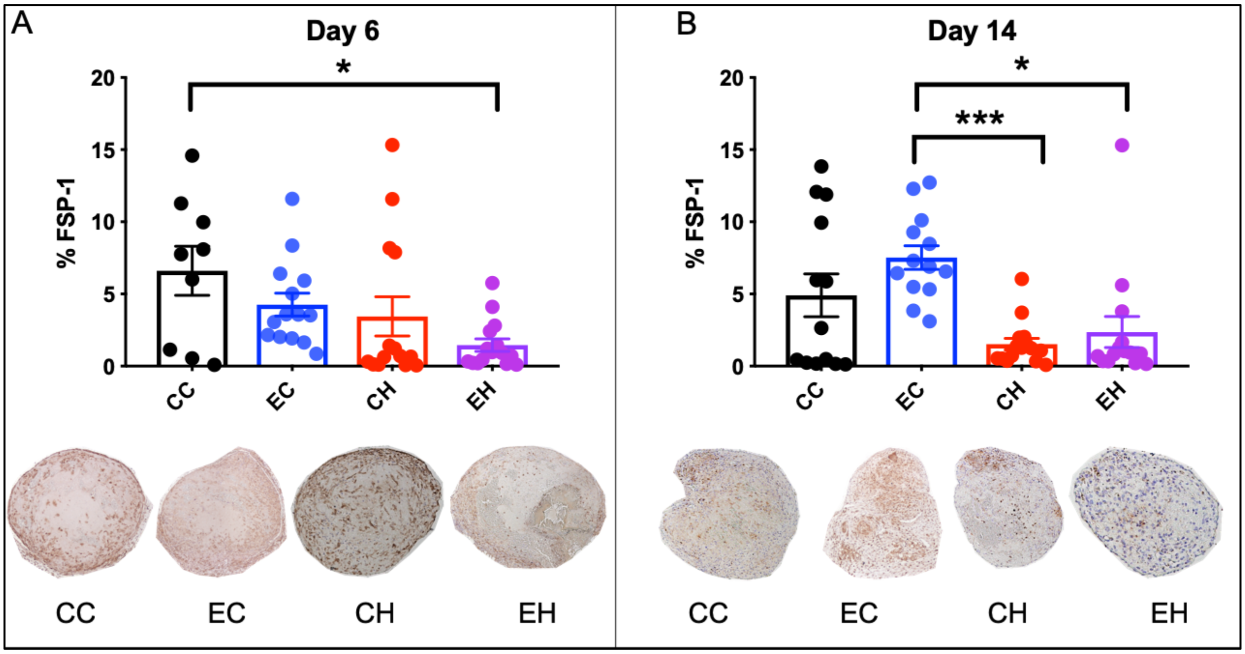

Figure 7.8 Fibroblast content as measured by immunohistochemistry (IHC) for FSP-1 at day 6 (A) and 14 (B) with representative IHC from each group. CC – true control; EC – exercise; CH – low molecular weight heparin (LMWH); EH – exercise + LMWH. * = $p<0.05$, *** = $p<0.001$.

7.3.3 Impact of Exercise on Circulating Inflammatory Cytokines

TNFα, CRP, and IL-6 are inflammatory cytokines known to be elevated in DVT [7], [19], [148], but decreased in healthy patients undergoing an exercise regimen [149]. We hypothesized that exercise would lead to a reduction in circulating inflammatory cytokines. At day 2, TNFα was elevated in EH mice compared to CH ($p<0.05$), but tended to decrease at days 6 and 14 (Figure 7.9A). In the untreated groups, TNFα tended to increase with exercise across time points, although this trend was not significant. LMWH groups had significantly decreased TNFα at day

6 compared to both non-treated groups. No significant trends were observed with CRP (Figure 7.9B). LMWH decreased serum IL-6 expression in CH mice compared to CC and EC mice at day 2 ($p<0.01$), in both LMWH groups compared to CC and EC groups at day 6, and in both LMWH groups compared to EC at day 14 (Figure 7.9C).

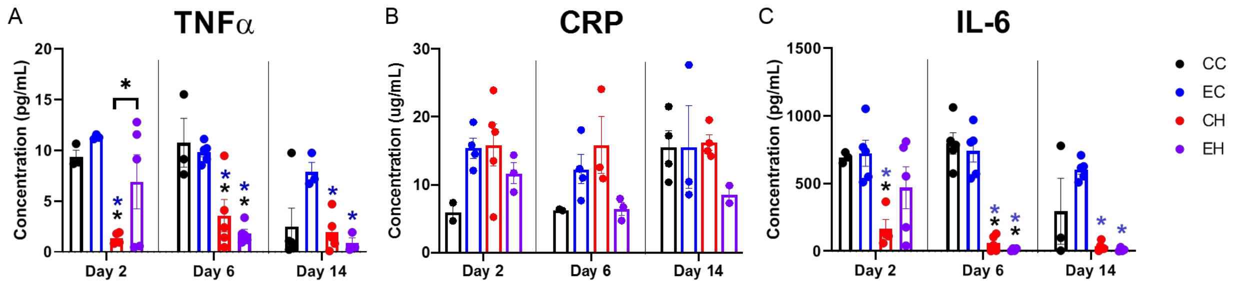

Figure 7.9 A) Circulating tumor necrosis factor alpha (TNFα) was elevated with exercise at day 2, but showed a decreasing trend with exercise at day 6 in both control and LMWH treatment groups and the LMWH group at day 14. B) Circulating C reactive protein (CRP) was not significantly different between groups at any time point. C) Interleukin-6 (IL-6) was significantly reduced with administration of LMWH but was not significantly different with exercise. CC – true control; EC – exercise; CH – low molecular weight heparin (LMWH); EH – exercise + LMWH. * = $p<0.05$. Significance bars only shown comparing exercise group to its treatment control group (i.e. CC vs EC and CH vs EH); all other comparisons denoted with asterisk colored by group of comparison.

7.4 Discussion

We have quantified the impact of spontaneous exercise—alone and coupled with standard anticoagulation treatment—on thrombus resolution and composition in a preclinical blood flow model of VT. Exercising mice showed a trend of reduced thrombus size across time points, with significantly reduced thrombus volume at day 11 in non-treated exercising mice compared to true controls. In chronic time points, thrombus volume in non-treated exercising mice was not significantly different from mice treated with LMWH, indicating that exercise has beneficial effects on thrombus resolution.

Exercise in non-treated mice attenuated local inflammation (neutrophil content), but not circulating inflammatory cytokines. However, due to limitations in the amount of blood collected from cardiac puncture, preliminary results of circulating inflammatory cytokines are limited by small numbers in some cases and will require further studies to determine significance. Exercise alone increased acute fibrin content and reduced sub-chronic collagen content. Together, this indicates the exercising individuals may respond better to thrombolytic therapy when timed appropriately. However, this effect was reversed in chronic thrombi, where the remaining thrombus in LMWH treated mice had significantly less collagen content compared to treated exercising mice. Increased fibroblast content compared to LMWH treated mice at day 14 indicates that untreated mice will become more collagen rich at more chronic time points, although differences with exercise were not observed.

The large variability in exercise activity between mice serves as a major limitation of this work. Exercising mice in our study ran slightly less compared to a previous study in which C57BL/6 males of the same age ran average of 2-3 km per day on the same type of setup [150]. Another study reported significantly more running activity (averaging 8-10 km per day) with an angled running track instead of a running wheel [151]. Future studies may benefit from switching to an angled running track for increased running activity, particularly following exercise. Due to the shape of the running wheel, mice must arch their back, a position which increases tension on their incision site (see Figure 7.10). Therefore, the angled running track (in which the mice maintain a neutral spine) may be more comfortable for post-surgical mice to use.

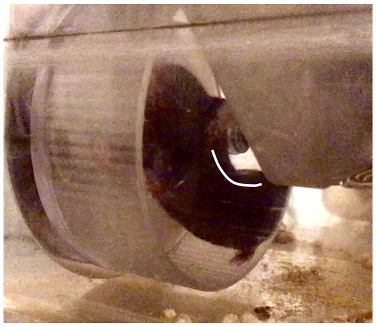

Figure 7.10 Picture of a mouse using the in-cage running wheel. White line shows curvature of the spine required to use the wheel, which increases tension on incision site.

If post-surgical activity increased with this method, it may be possible to parse out differences in prophylactic exercise compared to therapeutic exercise. We were not able to separate the two in this study due to the time needed for mice to acclimate to the running wheel and significantly reduced activity following surgery. To account for the large variation in exercise activity, further studies could separate mice into running performance groups based on pre-surgical exercise to allow comparison between mice from different time point groups. Classifications could consist of high performance (>20 km), medium performance (10-20 km), and low performance (<10 km).

In conclusion, this work represents the first basic science study of exercise on VT. We found that exercise reduces thrombus size and contributes to thrombus resolution. Additionally, exercise increases acute fibrin content, attenuates local but not systemic inflammation, and decreases sub-chronic collagen content in pharmacologically treated mice. Understanding the impact exercise may play on DVT could open a new avenue of treatment and/or inform treatment practice in the case of an athlete or highly active person with DVT. These findings support clinical findings that exercise is beneficial rather than harmful to patients, and provides insights on the compositional changes that result from exercise activity.

Chapter 8

Conclusions

8.1 Scientific Contributions

This work provides five contributions to the field of venous thrombosis research. The first three contributions directly impact preclinical model research, which are critical to advancing our understanding of DVT and the development of new treatment approaches and therapeutics. The third and fourth contributions have translational implications, with the potential to contribute to patient-specific treatment planning in DVT.

8.1.1 First *In Vivo* Characterization of the Murine Venous System

Previous studies of the venous system had focused on ex vivo measurements under supra-physiological conditions. Using MRI, we noninvasively quantified the cross-sectional area, cyclic strain, and circularity of the venous system in young and old, male and female C57BL/6 mice at five locations (PMID: 28865773). This work provided a foundation for drawing age and sex comparisons in disease models, provided physiologically relevant parameters to inform computation models, and represents the first *in vivo* characterization of the murine venous system at rest and during the application of a pharmacological exercise surrogate. These results are important for providing a greater understanding of the biomechanics of the venous system.

8.1.2 First Model Selection Algorithm

Prior to 2019, researchers hoping to use a mouse model of VT had no set of guidelines for selecting or implementing an appropriate model. Variation in surgical technique and major modifications to existing models confounded comparisons between labs and created ambiguity for investigators, manuscript reviewers, and grant reviewers alike. I had the opportunity to work with the American Venous Forum's Animal Model Task Force on developing the first consensus on mouse models of VT (PMID: 30786739). After compiling information on each animal model and gathering statistics and metrics for surgical technique validation, I developed the first model selection algorithm to guide researchers in selecting a model appropriate for their specific research question, which also suggests relevant secondary models to explore the research question in more than one setting. With the help of Dr. Diaz, the proposed algorithm was readily supported by the co-authors, all experts in animal models of VT. This tool will help investigators, manuscript reviewers, and grant reviewers understand the most appropriate primary and secondary model options for basic science investigations of VT.

8.1.3 Improvements to VT Model Surgical Equipment and Characterization

The EIM was originally developed in 2009, using equipment that was subsequently discontinued. Thus, when I began preparing to implement the EIM, I encountered a problem that had prevented several other researchers from moving forward with this valuable model. The only options in the U.S. were to purchase old equipment off eBay (which I and others have tried and found to be unreliable). Therefore, I developed an equipment alternative by constructing a standard voltage to current converter circuit powered by a direct current power supply, which offered the added benefit of significantly reducing costs. This validated method, along with a characterization of the current and time dependency of the EIM and natural history of the fibrinolytic system under flow conditions, offered a much-needed update on the EIM (PMID: 30046728). Since publishing this update, I have helped three other labs implement this equipment, enabling broader use of the EIM.

Characterization is fundamentally important for both consistencies in preclinical models and outlining the translational ability of a given model. MRI enabled two important characterization insights that would not have been possible with *ex vivo* or ultrasound studies. First, I demonstrated that leaving branches uninterrupted causes blood flow reversal, the cause of thrombus size variability in a proposed modification to the IVC ligation model. Second, I used high resolution MOTSA to quantify the endogenous venogenic response to IVC occlusion in two models of VT. This study showed that collateral vein patterns are influenced by pre-existing anatomy, collateralization correlates with the degree of occlusion, and importantly, venous collateral patterns in C57BL/ mice are consistent with those observed in humans.

8.1.4 Foundational Methodology for Determining Thrombus Composition

Successful treatment of DVT depends on the components present in the thrombus at the time of treatment, a composition which changes significantly over time. Currently, thrombus composition is inferred from the duration of symptoms, a metric that is inherently unreliable and is not able to account for heterogeneity within the thrombus or differences between patients. We developed a multiparametric MRI approach using readily translatable sequences that shows correlation with RBC, fibrin, and collagen content – important components for determining susceptibility to thrombolysis. This work provides a foundational methodology that could eventually enable physicians to determine regions amenable to thrombolysis, which would improve patient quality of life and reduce the risk of adverse events from treatment, including death.

8.1.5 First Basic Science Study of Exercise in VT

There is growing interest on the use of exercise as a treatment for cardiovascular disease, punctuated by the recent approval of supervised exercise therapy as a treatment for peripheral artery disease. Small clinical trials have shown exercise to be safe and beneficial to patients with DVT, yet little is known regarding how exercise affects thrombus formation and resolution. We conducted what is to our knowledge the first basic science study of the impact of exercise on VT. Our study looked at exercise alone, and in the clinically relevant scenario of exercise coupled with the standard treatment of LMWH. Using an in-cage running wheel, our results show that spontaneous exercise – both alone and in combination with standard treatment – reduces initial thrombus size and contributes to thrombus resolution. We found that exercise increases acute fibrin content, attenuates local inflammation but not circulating inflammatory cytokines, and decreases sub-chronic collagen content in pharmacologically treated mice. These findings support clinical findings that exercise is beneficial rather than harmful to patients, and provides insights on the compositional changes that result from exercise activity.

8.2 Future Directions

We found that age and sex impact the naïve murine venous system, but did not have the chance to investigate the role of age and sex on thrombus composition and treatment response. Age is a known risk factor for DVT, and studies have shown that thrombus resolution is impaired in aged mice [152]. Additionally, there are known sex differences in risk factors for DVT, yet preclinical studies focus almost exclusively on male mice. One study found that male mice had increased thrombotic potential [61], but this study was crucially flawed. As discussed in Chapter 3.1.5, interrupting the right uterine vein in female mice leads to necrosis of the reproductive organs. To avoid necrosis, the authors of this study interrupted all side branches in male mice but left branches open in female mice. I have shown that leaving branches uninterrupted is the source of thrombus size variability, thus the results of this paper may solely be the result of the sex-based modification of the model rather than true sex differences. Sex-based differences in preclinical models remain uncertain. The limitation of branching vessels in female mice could be overcome by the use of the BALBc strain, in which males and females have more back branches but no side branches in the segment of the IVC between the left renal vein and the iliac bifurcation. Understanding potential sex differences in thrombus composition could have important clinical implications in the treatment of DVT.

The study of aged mice may be especially important for understanding the impact of exercise because the majority of DVT patients are over the age of 50. Mice continually add body weight as they age, thus exercise studies on aged mice would need to switch to an angled running track because the larger old mice cannot readily fit inside a running wheel (see Figure 8.1). Studies have shown young C57BL/6 mice run significantly farther on angled running wheels, and this increased activity without the arched back tension on the incision site may enable studies on exercise as a therapeutic compared to a prophylactic.

Figure 8.1 An aged mouse (over 1 year old) checking out the in-cage running wheel. Aged mice become too large to be able to fit onto an in-cage running wheel.

The exercise studies were conducted using the EIM. Basic science findings are strongest when supported by data from more than one model. Repeating this study using the ligation model may show stronger differences between groups, particular in fibrosis and vein wall thickness as the vein wall is much more involved in the thrombotic process in the ligation model. Additionally, MP-MRI was performed on all mice in the exercise study, thus future studies could use this data to test the GMM framework on detecting composition differences under different treatment conditions.

8.3 Translational Potential

We have designed a method for non-invasive determination of thrombus composition to facilitate ease of clinical translation. The MP-MRI sequences are readily available and thus avoids potential issues of dealing with specially coded sequences on different scanner systems. The MP-MRI is faster than parameter mapping and does not require the use of contrast agents, thus is accessible to all patients able to undergo MRI scanning. Our GMM results have shown a general correlation with known composition, but this correlation does not consider spatial localization of each component. We are working on developing co-localization techniques to ensure the validity of this correlation. If successful, this method could be implemented in human studies.

The impact of exercise on DVT has two potential translational implications. First, basic science evidence can provide information on the mechanisms under which exercise influences thrombus resolution, which helps to counter the historical resistance to ambulation following diagnosis. Second, composition differences in exercising subjects could implicate a modified treatment regimen for athletes or people undergoing regular cardiovascular exercise diagnosed with DVT.

Appendix 1: Detailed Surgical Procedures

1.1 Surgical Preparation and Approach

Mice are anesthetized in a small anesthetic induction chamber using isoflurane at 5% and an oxygen flow rate of 500 mL/mn. Once the animal is at a respiration rate of approximately 1 breath every second, it is removed from the chamber, weighed, and the animal's abdomen hair is shaved and/or removed using a hair removal lotion (I prefer to use both methods). Then the animal is transferred to a nose cone atop a heating pad, in a dorsal recumbent position, and the oxygen flow is reduced to 200 mL/mn at 2%. The animal's shaved abdomen is wiped (cranially to caudally) with appropriate cleaning solutions (such as chlorhexidine or betadine in combination with alcohol wipes). A midline laparotomy is performed using iris scissors—not a blade—to ensure that only the skin is incised. The muscle layer is opened along the linea-alba to reduce pain/bleeding, and a Fine Science Tools (FST) retractor system or small internal abdominal retractor/eyelid retractor is placed to keep the abdominal cavity opened. To allow for easy visualization of the IVC, the intestines are exteriorized and placed on a sterile saline moistened 2x2 inch gauze pad to the animal's left, with an additional moistened gauze pad placed over the bowel. The surgery should then proceed as follows depending on the model.

1.2 Ligation Model

The fascia tissue on either side of the IVC is dissected using straight jeweler's forceps. Dissection is performed carefully, as grabbing the IVC alone may result in puncture. Small, controlled movements should be utilized when dissecting. Once visualized, all lateral branches are ligated with nonreactive 7-0 Prolene suture, slightly away from the IVC (approximately 1-2 mm), taking caution to avoid damaging the nerves that run parallel to the IVC on either side. Using a cotton swab to roll the IVC if accessing from animal's right side (usually more accessible), or straight forceps if accessing from animal's left side, posterior venous branches are cauterized using a Bovie low temperature fine tip cautery pen (MFI Medical Equipment, Inc; San Diego, CA). Slight compression with the cotton swab should be applied to collapse the posterior branches prior to cauterization to prevent bleeding. Gentle maneuvers when handling the IVC are strongly recommended.

Dissection between the IVC and aorta is then performed immediately below the left renal vein, usually within a window of 1-3 mm below where the left renal vein enters the IVC. The gap between the IVC and aorta is used to create a path underneath the IVC, and a 7-0 Prolene suture is passed through and tied down onto the IVC as close as possible to the left renal vein. Silk or nonreactive nylon/polyprolene sutures sized 4.0-7.0 may also be used. Dilation of the IVC is immediately observed. After the retractors are removed, the intestines are moistened and placed back into abdominal cavity. The abdomen is then closed with a continuous stitch using 3-0 Vicryl for the muscle layer, and the skin is closed with tissue glue.

1.3 EIM

1.3a Supplies Needed

If using the voltage to current converter described in Chapter 4, the following provides a list of equipment needed for the surgery and for construction of the voltage to current converter. Sample vendors and product numbers are provided as one option, however, other vendors or products could also work.

General surgery equipment

- Microscope & micro-surgical instruments

- Heating pad
- 7-0 Polyprolene for ligating side branches
- 5-0 Vicryl for closing the muscle (and skin if not using Vetbond)
- Vetbond for closing the skin
- Eye ointment to protect mouse's eyes during surgery
- Sterile saline
- Magnetic fixator retractor system – Fine Science Tools, Catalog No. 18200-20

Supplies for making EIM needle

- 30-gauge insulated copper wire – DigiKey, Part No. K617-ND
- 25-gauge needles – Fisher, Catalog No. 14-826AA
- Alice Clamp
- #11 blade

VIC-specific equipment

- Triple output DC power supply – Bell Electronics, E3630A
- Multimeter that can read µA – Lowe's Item # 447115 (cheaper option) or Digikey part No. 614-1042-ND
    - Alligator clips to connect multimeter to circuit (ensure compatibility with your mulitimeter leads) – Amazon Part No. a15042900ux0086 or AliExpress Model No. sh-255
- Operational amplifiers – need one of each (total of 2 op amps) but can order larger quantities for replacements. I've found the circuit to last 2 years.
    - AD620 - DigiKey, Part No. AD620BN-ND
    - UA741CP (DigiKey Part No. 296-11107-5-ND) *or* AD705

- Breadboard - Digikey Part No 1286-1062-ND
- Banana plug probe cables (4 cables total, so buy n=2 sets) - Grainger Item No. 4XKX1
- Resistors – as most resistors can only be bought in bulk (1000 or more), we recommend buying a kit – Amazon Model No. Top-cofrLD008
  - 40 kΩ resistor (somewhere close to this range will suffice)
  - 100 Ω resistor (somewhere close to this range will suffice)

1.3b Surgical Preparation

Prior to surgery, equipment should be prepared as follows. The EIM needle is prepared by cutting a 25-gauge needle to a length of 0.5 cm using a #11 blade and scoring the needle completely around until it is broken cleanly (no sharp edges and without decreasing the lumen of the needle). A 30-gauge silver-coated copper wire is measured to a length of approximately 20 cm, and the coating is stripped off on each end (0.3 cm off one end, approximately 2 cm of the other end). The 0.3 cm stripped wire end is inserted into the blunt end of the 0.5 cm 25-gauge needle, which is held in place using alligator forceps. A needle holder is used to clamp the needle onto the wire to secure it. The 2-cm end of the stripped wire is attached to a positive anode of a constant current machine. The needle is bent, bevel facing up, at 60-70° from the wire (less than 90° to avoid slipping out of the IVC, so that upon insertion the needle will be angled upwards along the anterior vein wall). A second piece of copper wire of the same length is prepared with the shorter stripped end bent into a small hook to be inserted into subcutaneous tissue. This second wire is connected to the negative terminal of the constant current source.

1.3c Surgical Procedure

Mice are prepared and surgery is initiated as described above. If lateral branches draining into the IVC are present, the immediately surrounding fascia tissue should be carefully dissected and a nonreactive 7-0 Prolene suture used to ligate the lateral branches. Care should be taken to avoid damaging the nerves that run parallel to the IVC on either side. To better visualize the iliac bifurcation, a moistened cotton tip broken off a cotton swab (without any rough edges) may be used as a laparotomy pad for bladder and seminal vesicles, held in place with FST retraction to keep these tissues from touching the IVC during the procedure. The copper wire is bent into an upside down "U" shape and taped such that the needle lies directly on top of the distal IVC, with care taken to avoid poking the IVC with the needle. The hook end of the second wire is inserted into subcutaneous tissue near the proximal end of the abdominal incision.

Next, the EIM needle connected to the anode is inserted into the IVC at the level of the lymph node just proximal to the iliac vein bifurcation. To accomplish this, a cotton swab is used to press on the IVC just below the left renal vein prior to needle insertion in order to dilate the IVC to prevent sticking the needle through the back of the IVC. A needle driver or forceps is used to hold the wire by the base of the needle to insert into the IVC, keeping the needle parallel to the vessel, taking care not to insert the needle all the way to where the needle meets the wire (insert approximately 90%) as this can increase the risk of bleeding. The inserted needle is elevated in order to contact the ventral surface of the IVC. This elevation can be accomplished by taping to a fixed structure such as the microscope, or through construction of a stable hook.

A direct current of 250 μA is applied over 15 minutes, which will produce a large thrombus from the iliac bifurcation extending to approximately the left renal vein by day 2. If modifying current or time to achieve a different thrombus size, these modifications should *decrease* one or both of these parameters, as higher current or longer application may result in paralysis.

The direct current generates free radicals in the copper wire, which results in endothelial cell activation. Saline is intermittently dripped into the abdomen while the current is being applied, and the brightness of the microscope is reduced to diminish tissue desiccation. Dark spots should become visible surrounding the needle during current application, indicating successful thrombus formation. Following electrolysis, the negative wire is removed first, and sterile saline is applied to the IVC around the anode needle to ease the removal process. While gripping the wire with a needle driver, small up and down motions should be used to release the needle from the anterior IVC wall before removal. Light or minimum pressure is applied to the insertion site without compressing the IVC following removal of the EIM needle. A laminar thrombus (visible during current application) forms immediately with maintenance of a flow channel and a solid thrombus can be harvested beginning at 2 hours following induction, depending on the mouse strain. The cotton tip is removed from the bladder area, and the intestines are moistened and placed back into the abdominal cavity. The muscle layer is closed with a continuous stitch using 3-0 Vicryl, and the skin is closed with tissue glue.

Appendix 2: Harvest Procedures

2.1 Harvest for Histology

The surrounding tissue, including the back musculature and aorta, serve as valuable anatomical landmarks in histology. As such, when harvesting for histology, it is most useful to harvest a block of tissue rather than only the infrarenal segment of the IVC. With the mouse under deep anesthesia, use scissors to cut a line parallel to either side of the IVC into the back musculature, approximately 3 mm on either side of the IVC. It is best to cut the sides first so that you can see where you are cutting before the cavity fills with blood. Next cut horizontally across the iliac veins, approximately 2 mm below the bifurcation (or where you guess the bifurcation to be), and hold onto that bottom part of the IVC with forceps (so you don't lose it in the pool of blood) while you make a horizontal cut near the left renal vein. If harvesting a thrombus from the ligation model, the top cut is straightforward – above the ligature site. If harvesting a thrombus from the EIM, be sure that you capture the top of the thrombus, which may extend a bit farther proximal from the left renal vein, in which case I like to angle the scissors to snip both the left renal vein and the segment of the IVC with thrombus at once.

While still holding the distal end of the thrombus/back muscle in your forceps, carefully cut underneath the thrombus to release the back musculature, keeping the scissors as close to the spine as you can. Once the block of tissue is entirely cut loose from the mouse, place it in formaldehyde (Formalin) overnight, followed by ethanol.

2.2 Harvest for Thrombus Weight

When harvesting for thrombus weight, the IVC must be carefully separated from the aorta and surrounding tissues. Separating the IVC from the aorta can be very difficult, especially at chronic time points. It is easiest to start by separating the IVC from the back musculature by passing forceps underneath both the IVC and aorta and opening the forceps slowly, moving proximal/distal to separate the entire infrarenal segment of the IVC from back musculature. The lumbar veins may need to be snipped if this process does not separate them by itself. If the lumbar veins are enlarged, wait to snip until after separating the aorta so that you can see what you're doing. Next, separate the lymph nodes that sit on the IVC near the iliac bifurcation. The lymph nodes may be separated following IVC removal, but it is often easier to do while still in the body.

Next, clasp the aorta with forceps, and using separate forceps, poke and open another pair of forceps on the fascia between the two vessels. Once a window is created between the aorta and IVC, pass closed forceps through and let them open, moving proximal/distal to widen the window. Once separated, cut the IVC with thrombus out by making a horizontal cut just distal to the iliac bifurcation, and another at the proximal end of the thrombus (above ligature for ligation model, at left renal vein or just above where thrombus ends if it extends farther proximal in the EIM). If harvesting a thrombus from the ligation model, the ligature may be used as a grabbing point to hold onto the IVC for separation procedures (although use caution because sometimes it comes off). If the aorta breaks in half during separation (common), carefully peel it away from the vessel however possible (before or after cutting the IVC) out.

Once removed, weigh the IVC (with thrombus) on a microscale capable of reading ~3-60 μg. This weight is referred to as the thrombus weight. The thrombus may be subsequently separated from the IVC for separate weighing or for q-RT PCR analysis. To separate at acute time points, clasp one end of the IVC with one forceps, and use another closed bent forceps to squeeze the thrombus out of the IVC. At chronic time points, the IVC may need to be carefully cut open under a microscope for scraping removal of the thrombus (very difficult).

Appendix 3: Note on Leg Edema in Murine Models

Leg edema is a primary indicator of DVT in humans, yet the presence or potential importance of leg edema in quadruped models had not previously been considered. Nonhuman primates are the only semi-upright model available for studying VT, but there are significant disadvantages of nonhuman primates including ethical considerations, cost, and the need for highly trained personnel. Lower limb edema is used as a clinical indicator of deep vein thrombosis, yet edema had not been a focus in animal models. We examined lower limb edema over time in the ligation model to address whether quadrupeds exhibit leg edema as a clinical feature.

Multiple axial slices were acquired through the lower limbs using a fast spin-echo sequence (TR: 2700 ms, TE_{eff}: 20 ms, FOV: (40 mm)2, matrix 256^2 zero-filled to 512^2 for an in-plane resolution of $(78\ \mu m)^2$, NEX: 3, slice thickness: 1 mm). Three consecutive axial slices of the calf located 4 mm below the knee were used to quantify calf volume using a threshold value of half the signal intensity in muscle (MRVision, MA). Over the same segment of leg, changes in the MRI signal itself were quantified using identical sequence parameters but with a 180° inversion preparation RF pulse (TI: 300 ms) to eliminate the signal from fat and highlight fluid accumulation in the musculature of the lower limbs. In this case, images were quantified using a threshold value of three standard deviations above mean muscle signal intensity (Figure A.1).

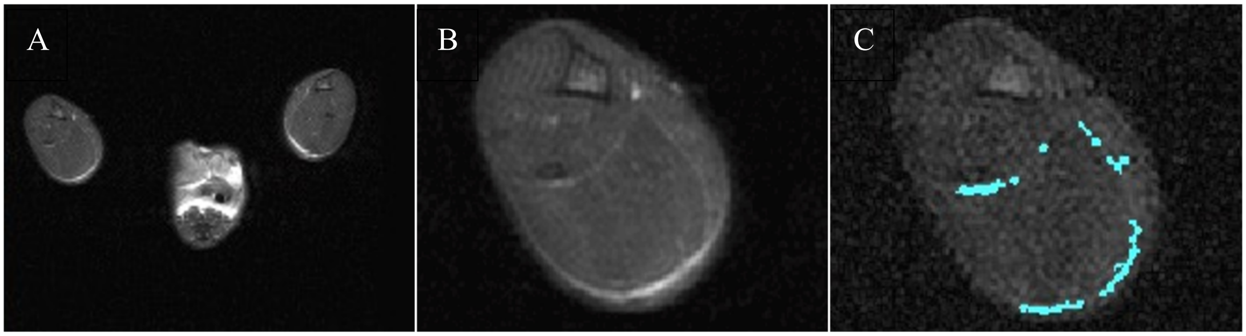

Figure A.1 Multiple 1 mm contiguous axial slices were acquired to encompass the calf region (A and B) using a fast spin-echo sequence. A 180° inversion preparation RF pulse was used to highlight fluid accumulation, measured using a threshold of three standard deviations above mean muscle signal intensity (C, blue).

The calf volume decreased at days 2 and 4 post-surgery (Figure A.2, line; pre-surgical volume 154.3 ± 13.5 mm3; day 2 134.7 ± 15.8 mm3, $p<0.05$; day 4 135.8 ± 13.7 mm3, $p<0.05$) and returned to pre-surgical volume by day 7. VT-associated lower leg edema was observed in 3 of the 5 mice, displaying the most edema between days 1 and 4 (Figure A.2, bar). By day 14, the MRI signal associated with edema was consistently smaller than pre-surgical values, but this difference did not reach statistical significance. Reduction in leg volume may be attributable to a loss of muscle mass associated with weight loss and decreased activity following surgery. Mice that did not demonstrate leg edema may have a larger network of collateral vessels develop early on. Interrupting the largest abdominal vein (IVC) resulted in leg edema in 3 of 5 mice. This confirms for the first time that quadruped models can display clinical features of venous thrombosis, but that lower limb edema is not consistent in this population size as is observed in humans.

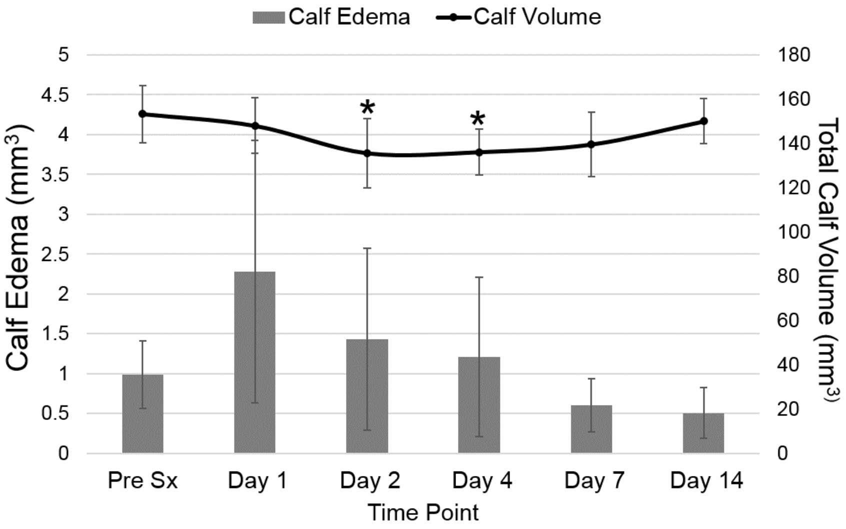

Figure A.2 Murine calf edema (bar) and total calf volume (line) as measured by MRI before surgery, and days 1, 2, 4, 7, and 14 following induction of VT using the IVC ligation model (n=5; mean, standard deviation; * denotes differences from pre-surgical volume of $p<0.05$).

Bibliography

[1] J. A. Heit, M. D. Silverstein, D. N. Mohr, T. M. Petterson, W. M. O'Fallon, and L. J. Melton, "Predictors of survival after deep vein thrombosis and pulmonary embolism: a population-based, cohort study.," *Arch. Intern. Med.*, vol. 159, no. 5, pp. 445–53, Mar. 1999.

[2] S. R. Kahn, C. E. M'Lan, D. L. Lamping, X. Kurz, A. Bérard, and L. Abenhaim, "The influence of venous thromboembolism on quality of life and severity of chronic venous disease.," *J. Thromb. Haemost.*, vol. 2, no. 12, pp. 2146–51, Dec. 2004.

[3] S. R. Kahn, "Prospective Evaluation of Health-Related Quality of Life in Patients With Deep Venous Thrombosis," *Arch. Intern. Med.*, vol. 165, no. 10, p. 1173, May 2005.

[4] J. Heit, A. Cohen, and F. Anderson, "Estimated annual number of incident and recurrent, non-fatal and fatal venous thromboembolism (VTE) events in the US.," *Blood*, vol. 106, no. 11, p. 910, 2005.

[5] N. Labropoulos, J. Jen, H. Jen, A. P. Gasparis, and A. K. Tassiopoulos, "Recurrent deep vein thrombosis: long-term incidence and natural history.," *Ann. Surg.*, vol. 251, no. 4, pp. 749–53, Apr. 2010.

[6] J. A. Diaz *et al.*, "P-selectin inhibition therapeutically promotes thrombus resolution and prevents vein wall fibrosis better than enoxaparin and an inhibitor to von Willebrand factor.," *Arterioscler. Thromb. Vasc. Biol.*, vol. 35, no. 4, pp. 829–37, Apr. 2015.

[7] B. M. Wojcik, S. K. Wrobleski, A. E. Hawley, T. W. Wakefield, D. D. Myers, and J. A. Diaz, "Interleukin-6: a potential target for post-thrombotic syndrome.," *Ann. Vasc. Surg.*,

vol. 25, no. 2, pp. 229–39, Mar. 2011.

[8] R. J. Glynn *et al.*, “A randomized trial of rosuvastatin in the prevention of venous thromboembolism.,” *N. Engl. J. Med.*, vol. 360, no. 18, pp. 1851–61, Apr. 2009.

[9] B. O. Patterson, R. Hinchliffe, I. M. Loftus, M. M. Thompson, and P. J. E. Holt, “Indications for catheter-directed thrombolysis in the management of acute proximal deep venous thrombosis.,” *Arterioscler. Thromb. Vasc. Biol.*, vol. 30, no. 4, pp. 669–74, Apr. 2010.

[10] J.-P. Galanaud, J.-P. Laroche, and M. Righini, “The history and historical treatments of deep vein thrombosis.,” *J. Thromb. Haemost.*, vol. 11, no. 3, pp. 402–11, Mar. 2013.

[11] K. P. LINK, “The Discovery of Dicumarol and Its Sequels,” *Circulation*, vol. 19, no. 1, pp. 97–107, Jan. 1959.

[12] L.-A. Linkins, P. T. Choi, and J. D. Douketis, “Clinical impact of bleeding in patients taking oral anticoagulant therapy for venous thromboembolism: a meta-analysis.,” *Ann. Intern. Med.*, vol. 139, no. 11, pp. 893–900, Dec. 2003.

[13] S. Sherry, “The origin of thrombolytic therapy,” *J. Am. Coll. Cardiol.*, vol. 14, no. 4, pp. 1085–1092, Oct. 1989.

[14] L. Watson, C. Broderick, and M. P. Armon, “Thrombolysis for acute deep vein thrombosis,” in *Cochrane Database of Systematic Reviews*, no. 1, L. Watson, Ed. Chichester, UK: John Wiley & Sons, Ltd, 2014.

[15] S. Vedantham *et al.*, “Pharmacomechanical Catheter-Directed Thrombolysis for Deep-Vein Thrombosis,” *N. Engl. J. Med.*, vol. 377, no. 23, pp. 2240–2252, Dec. 2017.

[16] P. Saha *et al.*, “Leukocytes and the natural history of deep vein thrombosis: current concepts and future directions.,” *Arterioscler. Thromb. Vasc. Biol.*, vol. 31, no. 3, pp.

506–12, Mar. 2011.

[17] Y. Zheng, J. Chen, and J. A. López, “Flow-driven assembly of VWF fibres and webs in in vitro microvessels.,” *Nat. Commun.*, vol. 6, p. 7858, Jul. 2015.

[18] M. W. J. Smeets, M. J. Mourik, H. W. M. Niessen, and P. L. Hordijk, “Stasis Promotes Erythrocyte Adhesion to von Willebrand Factor,” *Arterioscler. Thromb. Vasc. Biol.*, vol. 37, no. 9, pp. 1618–1627, Sep. 2017.

[19] J. A. Diaz *et al.*, “Plasma DNA is Elevated in Patients with Deep Vein Thrombosis.,” *J. Vasc. surgery. Venous Lymphat. Disord.*, vol. 1, no. 4, Oct. 2013.

[20] Y.-U. Lee, A. Y. Lee, J. D. Humphrey, and M. K. Rausch, “Histological and biomechanical changes in a mouse model of venous thrombus remodeling.,” *Biorheology*, vol. 52, no. 3, pp. 235–45, 2015.

[21] N. Bækgaard, P. Foegh, C. Wittens, and C. Arnoldussen, “Thrombus age is ideally measured by history or MRV prior to thrombus removal,” *Phlebol. J. Venous Dis.*, vol. 30, no. 1_suppl, pp. 20–26, Mar. 2015.

[22] J. W. Choi *et al.*, “CT venography for deep venous thrombosis: can it predict catheter-directed thrombolysis prognosis in patients with iliac vein compression syndrome?,” *Int. J. Cardiovasc. Imaging*, vol. 31, no. 2, pp. 417–26, Feb. 2015.

[23] M. Perrin, “Reconstructive surgery for deep vein reflux,” *Phlebologie*, vol. 43, no. 01, pp. 23–31, Jan. 2014.

[24] C. M. Lindquist, F. Karlicki, P. Lawrence, J. Strzelczyk, N. Pawlyshyn, and I. D. C. Kirkpatrick, “Utility of balanced steady-state free precession MR venography in the diagnosis of lower extremity deep venous thrombosis.,” *AJR. Am. J. Roentgenol.*, vol. 194, no. 5, pp. 1357–64, May 2010.

[25] J. M. Rubin *et al.*, “Sonographic elasticity imaging of acute and chronic deep venous thrombosis in humans.,” *J. Ultrasound Med.*, vol. 25, no. 9, pp. 1179–86, Sep. 2006.

[26] B. Dharmarajah, V. Sounderajah, S. P. Rowland, E. L. S. Leen, and A. H. Davies, “Aging techniques for deep vein thrombosis: a systematic review.,” *Phlebology*, vol. 30, no. 2, pp. 77–84, Mar. 2015.

[27] C. P. Cantwell, A. Cradock, J. Bruzzi, P. Fitzpatrick, S. Eustace, and J. G. Murray, “MR Venography with True Fast Imaging with Steady-state Precession for Suspected Lower-limb Deep Vein Thrombosis.”

[28] R. E. Westerbeek *et al.*, “Magnetic resonance direct thrombus imaging of the evolution of acute deep vein thrombosis of the leg.,” *J. Thromb. Haemost.*, vol. 6, no. 7, pp. 1087–92, Jul. 2008.

[29] M. Tan *et al.*, “Magnetic resonance direct thrombus imaging differentiates acute recurrent ipsilateral deep vein thrombosis from residual thrombosis.,” *Blood*, vol. 124, no. 4, pp. 623–7, Jul. 2014.

[30] D. G. W. Fraser, A. R. Moody, P. S. Morgan, A. L. Martel, and I. Davidson, “Diagnosis of lower-limb deep venous thrombosis: a prospective blinded study of magnetic resonance direct thrombus imaging.,” *Ann. Intern. Med.*, vol. 136, no. 2, pp. 89–98, Jan. 2002.

[31] V. Mani *et al.*, “A Multicenter MRI Protocol for the Evaluation and Quantification of Deep Vein Thrombosis.,” *J. Vis. Exp.*, no. 100, p. e52761, Jan. 2015.

[32] I. A. Mendichovszky *et al.*, “Combined MR direct thrombus imaging and non-contrast magnetic resonance venography reveal the evolution of deep vein thrombosis: a feasibility study,” *Eur. Radiol.*, vol. 27, no. 6, pp. 2326–2332, Jun. 2017.

[33] M. B. Streiff, P. J. Brady, A. M. Grant, S. D. Grosse, B. Wong, and T. Popovic, “CDC

Grand Rounds: Preventing Hospital-Associated Venous Thromboembolism," *Morb. Mortal. Wkly. Rep.*, vol. 63, no. 9, pp. 190–193, 2014.

[34] S. R. Kahn *et al.*, "The postthrombotic syndrome: Evidence-based prevention, diagnosis, and treatment strategies: A scientific statement from the American heart association," *Circulation*, vol. 130, no. 18, pp. 1636–1661, 2014.

[35] P. Prandoni *et al.*, "Residual venous thrombosis as a predictive factor of recurrent venous thromboembolism.," *Ann. Intern. Med.*, vol. 137, no. 12, pp. 955–60, Dec. 2002.

[36] M. K. Puurunen, P. N. Gona, M. G. Larson, J. M. Murabito, J. W. Magnani, and C. J. O'Donnell, "Epidemiology of venous thromboembolism in the Framingham Heart Study," *Thromb. Res.*, vol. 145, pp. 27–33, Sep. 2016.

[37] C. J. Goergen *et al.*, "In vivo quantification of murine aortic cyclic strain, motion, and curvature: implications for abdominal aortic aneurysm growth.," *J. Magn. Reson. Imaging*, vol. 32, no. 4, pp. 847–58, Oct. 2010.

[38] J. M. Greve *et al.*, "Allometric scaling of wall shear stress from mice to humans: quantification using cine phase-contrast MRI and computational fluid dynamics.," *Am. J. Physiol. Heart Circ. Physiol.*, vol. 291, no. 4, pp. H1700-8, Oct. 2006.

[39] C. L. Chen, P. A. Tunick, and I. Kronzon, "Pulmonary Vein Compression by Tumor: An Unusual Doppler Flow Pattern," *Echocardiography*, vol. 22, no. 9, pp. 746–747, Oct. 2005.

[40] C. Liu, D. Li, J. Guo, Q. Cui, L. Zhang, and Y. Zeng, "Four case reports on pelvic tumors with deep venous thromboses as main symptoms and literature review," *J Can Res Ther*, vol. [Epub ahea, no. [cited 2017 Jun 29], 2017.

[41] E. J. Zucker, S. Ganguli, B. B. Ghoshhajra, R. Gupta, and A. M. Prabhakar, "Imaging of

venous compression syndromes," *Cardiovasc. Diagn. Ther.*, vol. 6, no. 6, pp. 519–532, Dec. 2016.

[42] M. H. Meissner *et al.*, "The hemodynamics and diagnosis of venous disease," *J. Vasc. Surg.*, vol. 46, no. 6, pp. S4–S24, Dec. 2007.

[43] Y. U. Lee, Y. Naito, H. Kurobe, C. K. Breuer, and J. D. Humphrey, "Biaxial mechanical properties of the inferior vena cava in C57BL/6 and CB-17 SCID/bg mice.," *J. Biomech.*, vol. 46, no. 13, pp. 2277–82, Sep. 2013.

[44] K. C. McGilvray, R. Sarkar, K. Nguyen, and C. M. Puttlitz, "A biomechanical analysis of venous tissue in its normal and post-phlebitic conditions.," *J. Biomech.*, vol. 43, no. 15, pp. 2941–7, Nov. 2010.

[45] D. P. Sokolis, "Passive mechanical properties and constitutive modeling of blood vessels in relation to microstructure," *Med. Biol. Eng. Comput.*, vol. 46, no. 12, pp. 1187–1199, Dec. 2008.

[46] NIH, "NOT-OD-15-102: Consideration of Sex as a Biological Variable in NIH-funded Research," *National Institutes of Health*, 2015. [Online]. Available: https://grants.nih.gov/grants/guide/notice-files/NOT-OD-15-102.html. [Accessed: 29-Jun-2017].

[47] M. H. Criqui *et al.*, "Chronic venous disease in an ethnically diverse population: the San Diego Population Study.," *Am. J. Epidemiol.*, vol. 158, no. 5, pp. 448–56, Sep. 2003.

[48] P. Prandoni, S. Barbar, M. Milan, V. Vedovetto, and R. Pesavento, "The risk of recurrent thromboembolic disorders in patients with unprovoked venous thromboembolism: New scenarios and opportunities," *Eur. J. Intern. Med.*, vol. 25, no. 1, pp. 25–30, Jan. 2014.

[49] E. Nagel *et al.*, "Noninvasive Diagnosis of Ischemia-Induced Wall Motion Abnormalities

With the Use of High-Dose Dobutamine Stress MRI," *Circulation*, vol. 99, no. 6, 1999.

[50] S.-S. Yao and F. A. Chaudhry, "Assessment of Myocardial Viability with Dobutamine Stress Echocardiography in Patients with Ischemic Left Ventricular Dysfunction," *Echocardiography*, vol. 22, no. 1, pp. 71–83, Jan. 2005.

[51] S. D. Calligaris, M. Ricca, and P. Conget, "Cardiac Stress Test Induced By Dobutamine And Monitored By Cardiac Catheterization In Mice," *J. Vis. Exp.*, no. 72, Feb. 2013.

[52] F. Wiesmann *et al.*, "Dobutamine-stress magnetic resonance microimaging in mice : acute changes of cardiac geometry and function in normal and failing murine hearts.," *Circ. Res.*, vol. 88, no. 6, pp. 563–9, Mar. 2001.

[53] S. P. Williams *et al.*, "Dobutamine stress cine-MRI of cardiac function in the hearts of adult cardiomyocyte-specific VEGF knockout mice.," *J. Magn. Reson. Imaging*, vol. 14, no. 4, pp. 374–82, Oct. 2001.

[54] K. Flurkey, J. Currer, and D. Harrison, "Mouse Models in Aging Research," in *The Mouse in Biomedical Research*, 2nd ed., J. Fox, S. Barthold, M. Davisson, C. Newcomer, and F. Quimby, Eds. Elsevier, 2007, pp. 637–672.

[55] X. Zhou *et al.*, "Mutation responsible for the mouse pygmy phenotype in the developmentally regulated factor HMGI-C.," *Nature*, vol. 376, no. 6543, pp. 771–4, Aug. 1995.

[56] A. Fronek, M. H. Criqui, J. Denenberg, and R. D. Langer, "Common femoral vein dimensions and hemodynamics including Valsalva response as a function of sex, age, and ethnicity in a population study," *J. Vasc. Surg.*, vol. 33, no. 5, pp. 1050–1056, 2001.

[57] F. Demontis, R. Piccirillo, A. L. Goldberg, and N. Perrimon, "Mechanisms of skeletal muscle aging: insights from Drosophila and mammalian models," *Dis. Model. Mech.*, vol.

6, no. 6, pp. 1339–1352, Nov. 2013.

[58] M. Sandri *et al.*, “Signalling pathways regulating muscle mass in ageing skeletal muscle. The role of the IGF1-Akt-mTOR-FoxO pathway,” *Biogerontology*, vol. 14, no. 3, pp. 303–323, Jun. 2013.

[59] K. N. Frayn, P. Arner, and H. Yki-Järvinen, “Fatty acid metabolism in adipose tissue, muscle and liver in health and disease,” *Essays Biochem.*, vol. 42, 2006.

[60] D. Valecchi *et al.*, “Internal jugular vein valves: an assessment of prevalence, morphology and competence by color Doppler echography in 240 healthy subjects.,” *Ital. J. Anat. Embryol.*, vol. 115, no. 3, pp. 185–9, 2010.

[61] C. M. Alvarado, J. A. Diaz, A. E. Hawley, S. K. Wrobleski, R. E. Sigler, and D. D. Myers, “Male mice have increased thrombotic potential: sex differences in a mouse model of venous thrombosis.,” *Thromb. Res.*, vol. 127, no. 5, pp. 478–86, May 2011.

[62] C. J. Goergen, B. L. Johnson, J. M. Greve, C. A. Taylor, and C. K. Zarins, “Increased Anterior Abdominal Aortic Wall Motion: Possible Role in Aneurysm Pathogenesis and Design of Endovascular Devices,” *J. Endovasc. Ther.*, vol. 14, no. 4, pp. 574–584, Aug. 2007.

[63] J. L. Cox, D. A. Chiasson, A. I. Gotlieb, and et al., “Stranger in a strange land: the pathogenesis of saphenous vein graft stenosis with emphasis on structural and functional differences between veins and arteries.,” *Prog. Cardiovasc. Dis.*, vol. 34, no. 1, pp. 45–68, 1989.

[64] A. Phinikaridou, M. E. Andia, P. Saha, B. Modarai, A. Smith, and R. M. Botnar, “In vivo magnetization transfer and diffusion-weighted magnetic resonance imaging detects thrombus composition in a mouse model of deep vein thrombosis.,” *Circ. Cardiovasc.*

Imaging, vol. 6, no. 3, pp. 433–40, May 2013.

[65] S. Magder, “Volume and its relationship to cardiac output and venous return.,” *Crit. Care*, vol. 20, no. 1, p. 271, Sep. 2016.

[66] S. Gelman, “Venous Function and Central Venous Pressure,” *Anesthesiology*, vol. 108, no. 4, pp. 735–748, Apr. 2008.

[67] J. A. Diaz, D. M. Farris, S. K. Wrobleski, D. D. Myers, and T. W. Wakefield, “Inferior vena cava branch variations in C57BL/6 mice have an impact on thrombus size in an IVC ligation (stasis) model.,” *J. Thromb. Haemost.*, vol. 13, no. 4, pp. 660–4, Apr. 2015.

[68] N. A. Dewyer *et al.*, “Divergent effects of Tlr9 deletion in experimental late venous thrombosis resolution and vein wall injury.,” *Thromb. Haemost.*, vol. 114, no. 5, pp. 1028–37, Nov. 2015.

[69] A. Brill *et al.*, “von Willebrand factor-mediated platelet adhesion is critical for deep vein thrombosis in mouse models.,” *Blood*, vol. 117, no. 4, pp. 1400–7, Jan. 2011.

[70] M.-L. von Brühl *et al.*, “Monocytes, neutrophils, and platelets cooperate to initiate and propagate venous thrombosis in mice in vivo.,” *J. Exp. Med.*, vol. 209, no. 4, pp. 819–35, Apr. 2012.

[71] Y. Hisada, C. Ay, A. C. Auriemma, B. C. Cooley, and N. Mackman, “Human pancreatic tumors grown in mice release tissue factor-positive microvesicles that increase venous clot size,” *J. Thromb. Haemost.*, vol. 15, no. 11, pp. 2208–2217, Nov. 2017.

[72] K. A. Patterson *et al.*, “Rosuvastatin reduced deep vein thrombosis in ApoE gene deleted mice with hyperlipidemia through non-lipid lowering effects.,” *Thromb. Res.*, vol. 131, no. 3, pp. 268–76, Mar. 2013.

[73] P. K. Henke *et al.*, “Toll-like receptor 9 signaling is critical for early experimental deep

vein thrombosis resolution.," *Arterioscler. Thromb. Vasc. Biol.*, vol. 31, no. 1, pp. 43–9, Jan. 2011.

[74] K. B. Deatrick *et al.*, "The effect of matrix metalloproteinase 2 and matrix metalloproteinase 2/9 deletion in experimental post-thrombotic vein wall remodeling," *J. Vasc. Surg.*, vol. 58, no. 5, p. 1375–1384.e2, Nov. 2013.

[75] I. Singh *et al.*, "Antithrombotic effects of controlled inhibition of factor VIII with a partially inhibitory human monoclonal antibody in a murine vena cava thrombosis model," *Blood*, vol. 99, no. 9, 2002.

[76] A. Brill *et al.*, "Extrahepatic High-Density Lipoprotein Receptor SR-BI and ApoA-I Protect Against Deep Vein Thrombosis in Mice," *Arterioscler. Thromb. Vasc. Biol.*, vol. 32, no. 8, pp. 1841–1847, Aug. 2012.

[77] T. Ponomaryov, H. Payne, L. Fabritz, D. D. Wagner, and A. Brill, "Mast Cells Granular Contents Are Crucial for Deep Vein Thrombosis in Mice," *Circ. Res.*, p. CIRCRESAHA.117.311185, Jul. 2017.

[78] H. Payne, T. Ponomaryov, S. P. Watson, and A. Brill, "Mice with a deficiency in CLEC-2 are protected against deep vein thrombosis," *Blood*, vol. 129, no. 14, pp. 2013–2020, Apr. 2017.

[79] M. M. Aleman *et al.*, "Factor XIII activity mediates red blood cell retention in venous thrombi.," *J. Clin. Invest.*, vol. 124, no. 8, pp. 3590–600, Aug. 2014.

[80] M. Brandt *et al.*, "Deep vein thrombus formation induced by flow reduction in mice is determined by venous side branches," *Clin. Hemorheol. Microcirc.*, vol. 56, no. 2, pp. 145–152, Jan. 2014.

[81] G. M. Thomas *et al.*, "Tissue factor expressed by circulating cancer cell-derived

microparticles drastically increases the incidence of deep vein thrombosis in mice.," *J. Thromb. Haemost.*, vol. 13, no. 7, pp. 1310–9, Jul. 2015.

[82] X. Wang, P. L. Smith, M.-Y. Hsu, M. L. Ogletree, and W. A. Schumacher, "Murine model of ferric chloride-induced vena cava thrombosis: evidence for effect of potato carboxypeptidase inhibitor.," *J. Thromb. Haemost.*, vol. 4, no. 2, pp. 403–10, Feb. 2006.

[83] C. M. Ripplinger *et al.*, "Inflammation Modulates Murine Venous Thrombosis Resolution In Vivo: Assessment by Multimodal Fluorescence Molecular Imaging," *Arterioscler. Thromb. Vasc. Biol.*, vol. 32, no. 11, pp. 2616–2624, Nov. 2012.

[84] B. C. Cooley and G. Schmeling, "Murine model of large-vein electrolytic injury induction of thrombosis with slow resolution.," *Thromb. Res.*, vol. 140, pp. 149–152, Apr. 2016.

[85] B. C. Cooley, "In vivo fluorescence imaging of large-vessel thrombosis in mice.," *Arterioscler. Thromb. Vasc. Biol.*, vol. 31, no. 6, pp. 1351–6, Jun. 2011.

[86] J. A. Diaz *et al.*, "Thrombogenesis with continuous blood flow in the inferior vena cava. A novel mouse model.," *Thromb. Haemost.*, vol. 104, no. 2, pp. 366–75, Aug. 2010.

[87] J. A. Diaz, S. K. Wrobleski, A. E. Hawley, B. R. Lucchesi, T. W. Wakefield, and D. D. Myers, "Electrolytic inferior vena cava model (EIM) of venous thrombosis.," *J. Vis. Exp.*, no. 53, p. e2737, Jul. 2011.

[88] J. A. Diaz *et al.*, "The electrolytic inferior vena cava model (EIM) to study thrombogenesis and thrombus resolution with continuous blood flow in the mouse.," *Thromb. Haemost.*, vol. 109, no. 6, pp. 1158–69, Jun. 2013.

[89] O. R. Palmer, C. B. Chiu, A. Cao, U. M. Scheven, J. A. Diaz, and J. M. Greve, "In vivo characterization of the murine venous system before and during dobutamine stimulation: implications for preclinical models of venous disease," *Ann. Anat. - Anat. Anzeiger*, vol.

214, pp. 43–52, Nov. 2017.

[90] F. Banno *et al.*, “Exacerbated venous thromboembolism in mice carrying a protein S K196E mutation.,” *Blood*, vol. 126, no. 19, pp. 2247–53, Nov. 2015.

[91] J. A. Diaz, “Animal models of VT: to change or not to change?,” *Blood*, vol. 126, no. 19, pp. 2177–2178, Nov. 2015.

[92] O. R. Palmer, M. E. Shaydakov, J. P. Rainey, D. A. Lawrence, J. M. Greve, and J. A. Diaz, “Update on the electrolytic IVC model for pre-clinical studies of venous thrombosis,” *Res. Pract. Thromb. Haemost.*, vol. 2, pp. 266–273, Jan. 2018.

[93] E. Andraska *et al.*, “Pre-Clinical Model to Study Recurrent Venous Thrombosis in the Inferior Vena Cava,” *Thromb. Haemost.*, vol. 118, no. 06, pp. 1048–1057, Jun. 2018.

[94] G. Lorenzatti Hiles *et al.*, “Abstract 20227: Impact of Solid Tumors on Venous Thrombosis: A Novel Unified Model to Understand Cancer-Associated Thrombosis,” *Circulation*, vol. 134, no. Suppl 1, 2016.

[95] S. P. Grover, C. E. Evans, A. S. Patel, B. Modarai, P. Saha, and A. Smith, “Assessment of Venous Thrombosis in Animal ModelsSignificance,” *Arterioscler. Thromb. Vasc. Biol.*, vol. 36, no. 2, pp. 245–252, Feb. 2016.

[96] J. Charan and N. D. Kantharia, “How to calculate sample size in animal studies?,” *J. Pharmacol. Pharmacother.*, vol. 4, no. 4, pp. 303–6, Oct. 2013.

[97] J. Geddings, M. M. Aleman, A. Wolberg, M. L. von Br??hl, S. Massberg, and N. Mackman, “Strengths and weaknesses of a new mouse model of thrombosis induced by inferior vena cava stenosis: Communication from the SSC of the ISTH,” *J. Thromb. Haemost.*, vol. 12, no. 4, pp. 571–573, 2014.

[98] K. Sugimoto *et al.*, “The safety, efficacy, and pharmacoeconomics of low-dose alteplase

compared with urokinase for catheter-directed thrombolysis of arterial and venous occlusions," *J. Vasc. Surg.*, vol. 37, no. 3, pp. 512–517, Mar. 2003.

[99] M. Lin, J. C. F. Hsieh, M. Hanif, A. McDaniel, and D. K. Chew, "Evaluation of thrombolysis using tissue plasminogen activator in lower extremity deep venous thrombosis with concomitant femoral-popliteal venous segment involvement," *J. Vasc. Surg. Venous Lymphat. Disord.*, vol. 5, no. 5, pp. 613–620, Sep. 2017.

[100] J. C. Garber *et al.*, *Guide for the Care and Use of Laboratory Animals*, 8th ed. National Academies Press (US), 2011.

[101] S. Lynch *et al.*, "Semiautomatic Computational Method for the Quantification of Histologic Elements of Experimental Venous Thrombi," *J. Vasc. Surg. Venous Lymphat. Disord.*, vol. 5, no. 1, pp. 146–147, Jan. 2017.

[102] J. A. Diaz *et al.*, "Impaired fibrinolytic system in ApoE gene-deleted mice with hyperlipidemia augments deep vein thrombosis.," *J. Vasc. Surg.*, vol. 55, no. 3, pp. 815–22, Mar. 2012.

[103] J. L. Romson, D. W. Haack, and B. R. Lucchesi, "Electrical induction of coronary artery thrombosis in the ambulatory canine: a model for in vivo evaluation of anti-thrombotic agents.," *Thromb. Res.*, vol. 17, no. 6, pp. 841–53, Mar. 1980.

[104] S. Vedantham *et al.*, "Rationale and design of the ATTRACT Study: A multicenter randomized trial to evaluate pharmacomechanical catheter-directed thrombolysis for the prevention of postthrombotic syndrome in patients with proximal deep vein thrombosis," *Am. Heart J.*, vol. 165, no. 4, p. 523–530.e3, Apr. 2013.

[105] S. Vedantham, "Catheter-directed thrombolysis to avoid late consequences of acute deep vein thrombosis," *Thromb. Res.*, Aug. 2017.

[106] M. H. Meissner, B. K. Zierler, R. O. Bergelin, W. L. Chandler, and D. E. Strandness, "Coagulation, fibrinolysis, and recanalization after acute deep venous thrombosis.," *J. Vasc. Surg.*, vol. 35, no. 2, pp. 278–85, Feb. 2002.

[107] Bondke Persson *et al.*, "Therapeutic arteriogenesis in peripheral arterial disease: combining intervention and passive training," *Vasa*, vol. 40, no. 3, pp. 177–187, May 2011.

[108] Y. Nishijima, Y. Akamatsu, P. R. Weinstein, and J. Liu, "Collaterals: Implications in cerebral ischemic diseases and therapeutic interventions," *Brain Res.*, vol. 1623, pp. 18–29, Oct. 2015.

[109] F. Lurie, "Invited commentary," *J. Vasc. Surg. Venous Lymphat. Disord.*, vol. 5, no. 1, p. 95, Jan. 2017.

[110] T. M. van Vuuren, S. Doganci, I. M. Toonder, R. De Graaf, and C. H. Wittens, "Venous stent patency may be affected by collateral vein lumen size," *Phlebology*, vol. 34, no. 1, pp. 32–39, Mar. 2018.

[111] R. L. M. Kurstjens, T. M. A. J. van Vuuren, M. A. F. de Wolf, R. de Graaf, C. W. K. P. Arnoldussen, and C. H. A. Wittens, "Abdominal and pubic collateral veins as indicators of deep venous obstruction," *J. Vasc. Surg. Venous Lymphat. Disord.*, vol. 4, no. 4, pp. 426–433, Oct. 2016.

[112] W.-S. Lou *et al.*, "Endovascular Treatment for Iliac Vein Compression Syndrome: a Comparison between the Presence and Absence of Secondary Thrombosis," *Korean J. Radiol.*, vol. 10, no. 2, p. 135, Apr. 2009.

[113] S. Kapur, E. Paik, A. Rezaei, and D. N. Vu, "Where There Is Blood, There Is a Way: Unusual Collateral Vessels in Superior and Inferior Vena Cava Obstruction,"

RadioGraphics, vol. 30, no. 1, pp. 67–78, Jan. 2010.

[114] L. M. Orella, J. M. Mellado, N. Y. Barea, S. S. Alava, R. L. López, and J. M. Cuartero, "ECR 2010 / C-3062 / Collateral pathways of the abdominal wall: anatomical review and pathologic findings at 64-slice multidetector CT angiography," in *European Society of Radiology*, 2010, p. C-3062.

[115] E. Kalchev, R. D. Popova, G. Valchev, Balev B., and B. G. Varna, "Congenital absence of inferior vena cava," in *EPOS - ECR*, 2015.

[116] D. L. M. Oterdoom, B. M. de Jong, P. V. J. M. Hoogland, and R. J. M. Groen, "Transient cauda equina compression syndrome and headache caused by internal vertebral venous plexus engorgement in a teenage female with vena cava inferior agenesis and iliac vein thrombosis.," *J. Neurol. Neurosurg. Psychiatry*, vol. 78, no. 11, pp. 1283–4, Nov. 2007.

[117] S. Specchi, M.-A. d'Anjou, E. N. Carmel, and G. Bertolini, "COMPUTED TOMOGRAPHIC CHARACTERISTICS OF COLLATERAL VENOUS PATHWAYS IN DOGS WITH CAUDAL VENA CAVA OBSTRUCTION," *Vet. Radiol. Ultrasound*, vol. 55, no. 5, pp. 531–538, Sep. 2014.

[118] W.-Y. Shi, S. Wu, L.-Y. Hu, C.-J. Liu, and J.-P. Gu, "Swine Model of Thrombotic Caval Occlusion Created by Autologous Thrombus Injection with Assistance of Intra-caval Net Knitting.," *Sci. Rep.*, vol. 5, p. 18546, Dec. 2015.

[119] J. R. Hetthéssy *et al.*, "High pressure-low flow remodeling of the rat saphenous vein wall.," *Phlebology*, vol. 33, no. 2, pp. 128–137, Mar. 2018.

[120] P. A. Araoz, G. P. Reddy, H. Tarnoff, C. L. Roge, and C. B. Higgins, "MR findings of collateral circulation are more accurate measures of hemodynamic significance than arm-leg blood pressure gradient after repair of coarctation of the aorta.," *J. Magn. Reson.*

Imaging, vol. 17, no. 2, pp. 177–83, Feb. 2003.

[121] S. Pujadas, G. P. Reddy, O. Weber, C. Tan, P. Moore, and C. B. Higgins, “Phase contrast MR imaging to measure changes in collateral blood flow after stenting of recurrent aortic coarctation: Initial experience,” *J. Magn. Reson. Imaging*, vol. 24, no. 1, pp. 72–76, Jul. 2006.

[122] J. M. Greve *et al.*, “Magnetic resonance angiography reveals therapeutic enlargement of collateral vessels induced by VEGF in a murine model of peripheral arterial disease.,” *J. Magn. Reson. Imaging*, vol. 24, no. 5, pp. 1124–32, Nov. 2006.

[123] V. M. Runge, “Safety of the Gadolinium-Based Contrast Agents for Magnetic Resonance Imaging, Focusing in Part on Their Accumulation in the Brain and Especially the Dentate Nucleus.,” *Invest. Radiol.*, vol. 51, no. 5, pp. 273–9, May 2016.

[124] R. J. McDonald *et al.*, “Gadolinium Retention: A Research Roadmap from the 2018 NIH/ACR/RSNA Workshop on Gadolinium Chelates,” *Radiology*, vol. 289, no. 2, pp. 517–534, Nov. 2018.

[125] M. R. Prince, H. L. Zhang, G. H. Roditi, T. Leiner, and W. Kucharczyk, “Risk factors for NSF: A literature review,” *J. Magn. Reson. Imaging*, vol. 30, no. 6, pp. 1298–1308, Dec. 2009.

[126] D. L. Parker, C. Yuan, and D. D. Blatter, “MR angiography by multiple thin slab 3D acquisition,” *Magn. Reson. Med.*, vol. 17, no. 2, pp. 434–451, Feb. 1991.

[127] R. O. Robison, D. D. Blatter, D. L. Parker, W. W. Barney, D. M. Perry, and K. C. Goodrich, “Reduction of slab boundary artifact with multiple overlapping thin slab acquisition in MR angiography of the cervical carotid artery,” *J. Magn. Reson. Imaging*, vol. 4, no. 4, pp. 529–535, Jul. 1994.

[128] C. Jacoby *et al.*, “Dynamic changes in murine vessel geometry assessed by high-resolution magnetic resonance angiography: a 9.4T study.,” *J. Magn. Reson. Imaging*, vol. 28, no. 3, pp. 637–45, Sep. 2008.

[129] C. Arnoldussen, R. Strijkers, D. Lambregts, M. Lahaye, R. de Graaf, and C. Wittens, “Feasibility of identifying deep vein thrombosis characteristics with contrast enhanced MR-Venography,” *Phlebol. J. Venous Dis.*, vol. 29, no. 1_suppl, pp. 119–124, May 2014.

[130] J. Vidmar, A. Blinc, and I. Sersa, “A comparison of the ADC and T2 mapping in an assessment of blood-clot lysability.,” *NMR Biomed.*, vol. 23, no. 1, pp. 34–40, Jan. 2010.

[131] P. Saha *et al.*, “Magnetic resonance T1 relaxation time of venous thrombus is determined by iron processing and predicts susceptibility to lysis.,” *Circulation*, vol. 128, no. 7, pp. 729–36, Aug. 2013.

[132] O. Wu, R. M. Dijkhuizen, and A. G. Sorensen, “Multiparametric magnetic resonance imaging of brain disorders.,” *Top. Magn. Reson. Imaging*, vol. 21, no. 2, pp. 129–38, Apr. 2010.

[133] S. E. Ungersma *et al.*, “Vessel imaging with viable tumor analysis for quantification of tumor angiogenesis.,” *Magn. Reson. Med.*, vol. 63, no. 6, pp. 1637–47, Jun. 2010.

[134] J. Viereck *et al.*, “MRI of atherothrombosis associated with plaque rupture,” *Arterioscler. Thromb. Vasc. Biol.*, vol. 25, no. 1, pp. 240–245, Jan. 2005.

[135] J. Vidmar, I. Sersa, E. Kralj, G. Tratar, and A. Blinc, “Discrimination between red blood cell and platelet components of blood clots by MR microscopy.,” *Eur. Biophys. J.*, vol. 37, no. 7, pp. 1235–40, Sep. 2008.

[136] G. Tratar *et al.*, “Characterization of pulmonary emboli ex vivo by magnetic resonance imaging and ultrasound.,” *Thromb. Res.*, vol. 120, no. 5, pp. 763–71, Jan. 2007.

[137] W. Blättler and H. Partsch, “Leg compression and ambulation is better than bed rest for the treatment of acute deep venous thrombosis.,” *Int. Angiol.*, vol. 22, no. 4, pp. 393–400, Dec. 2003.

[138] R. Beasley, N. Raymond, S. Hill, M. Nowitz, and R. Hughes, “eThrombosis: the 21st century variant of venous thromboembolism associated with immobility.,” *Eur. Respir. J.*, vol. 21, no. 2, pp. 374–6, Feb. 2003.

[139] M. Aschwanden *et al.*, “Acute deep vein thrombosis: early mobilization does not increase the frequency of pulmonary embolism.,” *Thromb. Haemost.*, vol. 85, no. 1, pp. 42–6, Jan. 2001.

[140] S. M. Schellong, T. Schwarz, J. Kropp, Y. Prescher, B. Beuthien-Baumann, and W. G. Daniel, “Bed rest in deep vein thrombosis and the incidence of scintigraphic pulmonary embolism.,” *Thromb. Haemost.*, vol. 82 Suppl 1, pp. 127–9, Sep. 1999.

[141] S. R. Kahn, I. Shrier, and C. Kearon, “Physical activity in patients with deep venous thrombosis: a systematic review.,” *Thromb. Res.*, vol. 122, no. 6, pp. 763–73, Jan. 2008.

[142] V. Gay, R. Hamilton, S. Heiskell, and A. M. Sparks, “Influence of bedrest or ambulation in the clinical treatment of acute deep vein thrombosis on patient outcomes: a review and synthesis of the literature.,” *Medsurg Nurs.*, vol. 18, no. 5, pp. 293–9, Jan. 2009.

[143] H. Partsch, M. Kaulich, and W. Mayer, “Immediate mobilisation in acute vein thrombosis reduces post-thrombotic syndrome.,” *Int. Angiol.*, vol. 23, no. 3, pp. 206–12, Sep. 2004.

[144] M. Jünger *et al.*, “Mobilization versus immobilization in the treatment of acute proximal deep venous thrombosis: a prospective, randomized, open, multicentre trial.,” *Curr. Med. Res. Opin.*, vol. 22, no. 3, pp. 593–602, Mar. 2006.

[145] M. D. Cook *et al.*, “Forced treadmill exercise training exacerbates inflammation and

causes mortality while voluntary wheel training is protective in a mouse model of colitis.," *Brain. Behav. Immun.*, vol. 33, pp. 46–56, Oct. 2013.

[146] J. M. Allen *et al.*, "Voluntary and forced exercise differentially alters the gut microbiome in C57BL/6J mice.," *J. Appl. Physiol.*, vol. 118, no. 8, pp. 1059–66, Apr. 2015.

[147] C. Werner *et al.*, "Physical exercise prevents cellular senescence in circulating leukocytes and in the vessel wall.," *Circulation*, vol. 120, no. 24, pp. 2438–47, Dec. 2009.

[148] E. A. Fox and S. R. Kahn, "The relationship between inflammation and venous thrombosis. A systematic review of clinical studies.," *Thromb. Haemost.*, vol. 94, no. 2, pp. 362–5, Aug. 2005.

[149] J. A. Woods, K. R. Wilund, S. A. Martin, and B. M. Kistler, "Exercise, inflammation and aging.," *Aging Dis.*, vol. 3, no. 1, pp. 130–40, Mar. 2012.

[150] J. P. Konhilas, U. Widegren, D. L. Allen, A. C. Paul, A. Cleary, and L. A. Leinwand, "Loaded wheel running and muscle adaptation in the mouse.," *Am. J. Physiol. Heart Circ. Physiol.*, vol. 289, no. 1, pp. H455-65, Jul. 2005.

[151] J. P. De Bono, D. Adlam, D. J. Paterson, and K. M. Channon, "Novel quantitative phenotypes of exercise training in mouse models.," *Am. J. Physiol. Regul. Integr. Comp. Physiol.*, vol. 290, no. 4, pp. R926-34, Apr. 2006.

[152] A. P. McDonald *et al.*, "Aging is associated with impaired thrombus resolution in a mouse model of stasis induced thrombosis.," *Thromb. Res.*, vol. 125, no. 1, pp. 72–8, Jan. 2010.